PNNL-26493

# Light Water Reactor Sustainability Program

# Physics-Based Modeling of Cable Insulation Conditions for Frequency Domain Reflectometry (FDR)

May 2017

U.S. Department of Energy

Office of Nuclear Energy

PNNL-26493

# Physics-Based Modeling of Cable Insulation Conditions for Frequency Domain Reflectometry (FDR)

**Authors: S.W. Glass[a], A.M. Jones[a], L.S. Fifield[a], T.S. Hartman[a], and N. Bowler[b]**

**a. Pacific Northwest National Laboratory**
**b. Iowa State University**

**May 2017**

**Prepared for the**
**U.S. Department of Energy**
**Office of Nuclear Energy**

**Light Water Reactor Sustainability Program**

# Physics-Based Modeling of Cable Insulation Conditions for Frequency Domain Reflectometry (FDR)

**PNNL-26493**

**May 2017**

**Approved by:**

Steve N. Schlahta
Director, Nuclear Science Project Management Office

May 23, 2016
Date

# SUMMARY

This Pacific Northwest National Laboratory milestone report describes progress to date on cable modeling to support a better understanding of frequency domain reflectometry (FDR) nondestructive tests. The work includes a review of relevant literature as well as experimental verification of model predictions.

As nuclear power plants consider applying for a second, or subsequent, license renewal to extend their operating period from 60 years to 80 years, it is important to understand how the materials installed in plant systems and components will age during that time and develop aging management programs to assure continued safe operation under normal and design-basis events (DBE). Normal component and system tests typically confirm the cables can perform their normal operational function. The focus of the cable test program, however, is directed toward the more demanding challenge of assuring the cable function under accident or DBE. The industry has adopted 50% elongation at break (EAB) relative to the un-aged cable condition as the acceptability standard. All tests are benchmarked against the cable EAB test. EAB, however, is a destructive test so the test programs must apply an array of other nondestructive examination (NDE) methods to assure or infer the overall cable system integrity. Most utilities already have a program associated with their first life extension from 40 to 60 years. Regrettably, there is neither a clear guideline nor a single NDE test that can assure cable function and integrity for all cables. Thankfully, however, implementation of a broad range of tests allows utilities to develop a practical program that assures cable function to a high degree.

One test that is gaining favor within the industry is FDR. This is a low-voltage nondestructive test that can be applied at a cable end. Testing from the cable end is important because local inspection all along the cable length is frequently very difficult because cables are routed within trays, conduits, underground, and through walls. The FDR technique has been shown to locate cable insulation damage due to thermal, radiation, and mechanical damage. However, the degree and extent of damage required for each defect type to produce detectable results is not well quantified and experimental generation of the expansive range of damage scenarios is expensive. Not only must cable segments be artificially aged or damaged, but these aged or damaged segments must be contiguous within relatively long (>15 m) cable lengths to allow meaningful FDR measurements. Thus, a physics-based modeling approach to characterize cable anomalies and their FDR response has been developed. The model has been benchmarked with several cable scenarios for which well-understood damage mechanisms were compared with the model predictions.

This work includes:

a. a review of FDR theory and practice

b. a review of relevant prior modeling publications

c. a description of the finite-element method models used to vary geometry and material properties

d. transfer of those properties to circuit models for characterizing expected FDR responses

e. experimental work to benchmark specific cases

f. parametric adjustment of the model to examine cable degradation cases.

Significant observations and conclusions from this study include:

- Defect length had an important influence on the FDR amplitude response. The maximum amplitude occurred for defect lengths that are on the order of 0.5 wavelength at the highest frequency used in the FDR inspection. This length corresponds to the spatial resolution available from the frequency sweep. This is an explanation for the relatively small responses for mechanical cable damage, since most mechanically damaged segments are only damaged over a short length.

- For longer damage segments consisting of a uniform change in the insulation dielectric constant (and thus local capacitance), the FDR response appeared as two distinct peaks centered on the ends of the damaged segments. This began to occur when the defect section was longer than the system resolution. The amplitudes of the two symmetric peaks were smaller than the amplitude of a similarly damaged segment that was approximately 0.5 to 1 wavelength long at the maximum frequency of the FDR sweep.
- When the damage profile was gradually tapered rather than occurring as a step condition change, the amplitude of the FDR peak was reduced. This effect was due to the tapered impedance transition that reduced the reflection from the tapered portion of the defect segment. If the length of the defect segment was smaller than the spatial resolution, the effect of a tapered damage profile was to simply reduce the amplitude of the single reflection.
- The FDR peaks were not significantly affected by:
  - Termination impedance value (short circuit, open circuit, finite resistance). The single exception was the line resonance analysis response with a matched termination.
  - Number of defects
  - Location of defects
  - Length of low-loss cable
- The FDR peak amplitudes were affected by:
  - Defect length
  - Defect profile
  - Environment around defect (air, water, metals)
  - Cable attenuation/loss
- Cable design affects the FDR response. Coaxial cables generally exhibit lower noise because of better fabrication tolerances and can be more sensitive to subtle changes in insulation characteristics than multi-conductor cable. For multi-conductor cables with a helical twist, inevitable variations in the twist rate (lay length) produce random fluctuations in the distributed inductance and capacitance, which can set a threshold for detection of defects.
- Shielded and unshielded cable configurations respond differently to the local environment. This difference is expected since the surrounding conductor in shielded cables serves to isolate the propagating signal from the external environment.
- For thermally damaged ethylene propylene rubber cable, capacitance changes of 40% to 60% corresponded to an end-of-life EAB of 50%. This was well above the reliably detectable 1% to 5% capacitance change. The threshold for reliable detection is dependent upon the intrinsic cable noise.
- The large reflections at the near end and far end of the cable can prevent inspection of degradations in these regions. Increasing the FDR bandwidth shortens the influence of the cable end reflection by improving the range resolution and can improve sensitivity, but higher bandwidths may not completely inspect longer cables due to signal attenuation. Adding separate cable extensions to artificially lengthen the inspection length can improve the ability to discern defect indications if the extension is impedance-matched to the cable being tested, the connection point does not introduce a significant reflection, and the defect amplitude response is large enough. The practicality of this approach may be limited in field conditions due to these factors.
- The swept-frequency bandwidth is a key parameter for obtaining useful data from FDR cable inspections. Simulated and measured cases for 100 ft. to 1000 ft. cables using bandwidths from 10 MHz to 1300 MHz showed the tradeoff between spatial resolution and signal attenuation. In example measurements, bandwidths of 200 MHz and 50 MHz were successfully used to inspect a shielded triad cable with lengths of 500 ft. and 1000 ft., respectively.

# ACKNOWLEDGMENTS

The authors would like to thank the following individuals who contributed to this report:

- Casey Sexton, Gary Harmon, Craig Harris, and Ryan O'Hagan of Analysis and Measurement Services Corporation for their overall review of the report.
- Paolo Fantoni of Wirescan and Jim Raines of Fauske Inc., a Westinghouse company, for helpful guidance with the use of the line resonance analysis system and overall review.

# CONTENTS

SUMMARY ..... ii

ACKNOWLEDGMENTS ..... iv

ACRONYMS AND ABREVIATIONS ..... xiii

1. OBJECTIVES ..... 1

2. INTRODUCTION AND BACKGROUND ..... 2

3. CABLE DESIGN, CLASSIFICATION, AND LAYOUT ..... 4

4. FREQUENCY DOMAIN REFLECTOMETRY THEORY ..... 7

5. CABLE AND FDR MODELING LITERATURE REVIEW ..... 13

6. FINITE ELEMENT SIMULATION MODEL ..... 15

7. WIRESCAN LIRA SIMULATOR ..... 17

8. VALIDATION OF SIMULATION RESULTS ..... 19

9. TEST AND SIMULATION RESULTS ..... 24
   - 9.1 Degree of Cable Damage ..... 24
   - 9.2 Defect Length ..... 28
   - 9.3 Defect Distribution ..... 34
   - 9.4 Cable Length ..... 39
   - 9.5 Defect Location ..... 41
   - 9.6 Multiple Defects ..... 44
   - 9.7 Use of Cable Extensions ..... 48
   - 9.8 Cable Termination ..... 54
   - 9.9 Cable Environment ..... 56
   - 9.10 Frequency Bandwidth ..... 59

10. CONCLUSIONS ..... 70

11. FUTURE WORK ..... 72

12. REFERENCES ..... 73

# FIGURES


Figure 3.1. Configurations of typical cable designs used in NPPs. 4

Figure 3.2. Typical cable layout allows access at control racks and termination junction boxes but much of the cable is protected within cable trays and conduit thereby limiting access for local inspections. 6

Figure 4.1. Example FDR excitation waveform in which the signal frequency linearly increases as a function of time. 7

Figure 4.2. (a) Electric and magnetic field configurations for generalized sinusoidal TEM wave propagation. (b) Electric and magnetic field configurations for specific cable types. 8

Figure 4.3. Transmission line RLGC circuit model consisting of distributed impedance elements over an infinitesimally short length. 8

Figure 4.4. Block diagram of FDR instrument and cable test arrangement. 9

Figure 4.5. Cross-section view of commonly used twisted-pair cable. 10

Figure 4.6. Example FDR impulse response data. Figure courtesy of AMS Corporation. 11

Figure 4.7. Example FDR step response data. Figure courtesy of AMS Corporation. 12

Figure 4.8. Measured FDR response for shielded triad cable with mechanically damaged defect as described in Section 9 at mid-point in the cable shown as: (*left*) impulse response and (*right*) step response. 12

Figure 6.1. Example ANSYS HFSS simulation models representing segments of (left) three-conductor shielded cable and (right) coaxial cable. 15

Figure 6.2. Example ANSYS Nexxim co-simulation model showing cascaded scattering parameter blocks containing HFSS results for damaged or undamaged cable segments. 15

Figure 7.1. Wirescan LIRA simulator for modeling FDR responses of coaxial and twisted-pair cable configurations. 17

Figure 8.1. VNA FDR instrument (*left*) and LIRA FDR instrument (*right*). 19

Figure 8.2. (*left*) RG-58 coaxial cable with 1.5 in. long mechanical damage; (*right*) corresponding ANSYS HFSS finite element model of damaged section. 19

Figure 8.3. (*left*) 200 MHz VNA measurement and (*right*) 200 MHz ANSYS simulation of 1.5 in. long damaged section at the halfway point of a 100 ft. RG-58 coaxial cable. 20

Figure 8.4. (*left*) 100 MHz VNA measurement and (*right*) 100 MHz ANSYS simulation of 1.5 in. long damaged section at the halfway point of a 100 ft. RG-58 coaxial cable. 20

Figure 8.5 (*left*) 100 MHz LIRA measurement of 1.5 in. long damaged section at halfway point of 100 ft. RG-58 coaxial cable and (*right*) corresponding 100 MHz LIRA simulation using 30% increase in insulation dielectric constant to match defect peak amplitude. 21

Figure 8.6. (*left*) Damaged 3.5 in. section at the halfway point of a 100 ft. three-conductor shielded 600V EPR cable; (*right*) corresponding ANSYS HFSS finite element model of damaged section. 21

Figure 8.7. (*left*) 200 MHz VNA measurement and (*right*) 200 MHz ANSYS simulation of damaged 3.5 in. section in the center of 100 ft. three-conductor shielded EPR cable. 22

Figure 8.8. (*left*) 100 MHz VNA measurement and (*right*) 100 MHz ANSYS simulation of damaged 3.5 in. section in the center of 100 ft. three-conductor shielded EPR cable. ..... 22

Figure 8.9. (*left*) 100 MHz LIRA measurement of 3.5 in. long damaged section at halfway point of 100 ft. three-conductor shielded EPR cable; (*right*) corresponding 100 MHz LIRA simulation using 5% increase in insulation dielectric constant to match defect peak amplitude. ..... 23

Figure 9.1. (a) Cross-section view of Okonite-FMR Okoseal cable; (b) in-house connector head that connects to the sample conductors; (c) connector attached to the sample, with temporary, grounded shield applied to the sample exterior. ..... 24

Figure 9.2. Comparison between EAB and specific capacitance C (*left*), and between EAB and Tan δ (*right*), at 0.1 Hz. The color indicates the color of the wire held at positive potential during the measurement. ..... 25

Figure 9.3. Same as for Figure 9.2 but at 1 kHz. ..... 25

Figure 9.4. (*left*) 100 MHz and (*right*) 200 MHz ANSYS simulations for insulation dielectric constant changes in a 1 ft. segment at the halfway point of 100 ft. coaxial cable. ..... 26

Figure 9.5. (*left*) 100 MHz and (*right*) 200 MHz ANSYS simulations for insulation dielectric constant changes in a 1 ft. segment at the halfway point of 100 ft. shielded triad cable. ..... 27

Figure 9.6. 100 MHz LIRA simulations for (*left*) insulation dielectric constant changes in a 1 ft. segment at the halfway point of 100 ft. coaxial cable and (*right*) capacitance changes in a 1 ft. segment at the halfway point of 100 ft. shielded triad cable. ..... 27

Figure 9.7. 200 MHz ANSYS simulation of 5% increase in insulation dielectric constant for relatively short defect lengths (<1 wavelength at maximum frequency) in three-conductor shielded cable ..... 28

Figure 9.8. 200 MHz ANSYS simulation of 5% increase in insulation dielectric constant for relatively long defect lengths (≥1 wavelength at maximum frequency) in three-conductor shielded cable ..... 29

Figure 9.9. 100 MHz ANSYS simulation of 5% increase in insulation dielectric constant for relatively short defect lengths (<1 wavelength at maximum frequency) in three-conductor shielded cable ..... 29

Figure 9.10. 100 MHz ANSYS simulation ofF 5% increase in insulation dielectric constant for relatively long defect lengths (≥1 wavelength at maximum frequency) in three-conductor shielded cable ..... 30

Figure 9.11. 100 MHz LIRA simulation of (*left*) 3% increase in insulation dielectric constant for defect lengths centered along 100 ft. coaxial cable with 0.3% stochastic noise and (*right*) 3% increase in local capacitance for defect lengths centered along 100 ft. twisted-pair cable with 2.5% stochastic noise. ..... 30

Figure 9.12. Accelerated aging experimental setup for heating 1.5 ft., 7.25 ft., and 10.5 ft. sections of three 100 ft. shielded three-conductor cables. ..... 31

Figure 9.13. Aged cable configurations for (*left*) in-situ LIRA measurements and (*right*) ex-situ VNA measurements. ..... 32

Figure 9.14. 100 MHz LIRA measurements for a uniformly aged (*left*) 1.5 ft. and (*right*) 7.25 ft. segment at the halfway point of 100 ft. shielded triad cable. ..... 32

Figure 9.15. (*left*) 100 MHz and (*right*) 200 MHz VNA measurements for a uniformly aged 7.25 ft. segment at the halfway point of 100 ft. shielded triad cable. ..... 33

Figure 9.16. (*left*) 100 MHz and (*right*) 200 MHz VNA measurements for a uniformly aged 1.5 ft. segment at the halfway point of 100 ft. shielded triad cable. ..... 33

Figure 9.17. (*left*) 100 MHz and (*right*) 200 MHz VNA measurements for a uniformly aged 10.5 ft. segment at the halfway point of 100 ft. shielded triad cable. ..... 34

Figure 9.18. Increase in insulation dielectric constant for uniform and symmetrically tapered cable damage for 10 ft. defect section. ..... 35

Figure 9.19. (*left*) 100 MHz and (*right*) 200 MHz ANSYS simulations for uniform and symmetrically tapered 10 ft. defect sections of 100 ft. three-conductor shielded cable. ..... 35

Figure 9.20. Increase in insulation dielectric constant for uniform and single-sided tapered cable damage cases for 10 ft. defect section. ..... 36

Figure 9.21. (*left*) 100 MHz and (*right*) 200 MHz ANSYS simulations for uniform and single-sided tapered 10 ft. defect sections of 100 ft. three-conductor shielded cable. ..... 36

Figure 9.22. Increase in insulation dielectric constant for uniform and symmetrically tapered cable damage cases for 2.5 ft. defect section. ..... 37

Figure 9.23. (*left*) 100 MHz and (*right*) 200 MHz ANSYS simulations for uniform and symmetrically tapered 2.5 ft. defect sections of 100 ft. three-conductor shielded cable. ..... 37

Figure 9.24. Increase in insulation dielectric constant for uniform and single-sided tapered cable damage cases for 2.5 ft. defect section. ..... 38

Figure 9.25. (*left*) 100 MHz and (*right*) 200 MHz ANSYS simulations for uniform and single-sided tapered 2.5 ft. defect sections of 100 ft. three-conductor shielded cable. ..... 38

Figure 9.26. 100 MHz LIRA simulations for uniform and symmetrically tapered (*left*) 10 ft. and (*right*) 2.5 ft. defect sections of twisted-pair cable. ..... 39

Figure 9.27. 200 MHz ANSYS simulations for 1 ft. defect section at location halfway along (*left*) 100 ft. and (*right*) 500 ft. three-conductor shielded cables. ..... 40

Figure 9.28. 100 MHz ANSYS simulations for 1 ft. defect section at location halfway along (*left*) 100 ft. and (*right*) 500 ft. three-conductor shielded cables. ..... 40

Figure 9.29. 100 MHz LIRA simulations for 1 ft. defect section at location halfway along (*left*) 100 ft. and (*right*) 500 ft. twisted-pair cables. ..... 41

Figure 9.30. (*left*) 100 MHz and (*right*) 200 MHz ANSYS simulations for 3 ft. defect section centered at 10 ft. of 100 ft. three-conductor shielded cable. ..... 42

Figure 9.31. (*left*) 100 MHz and (*right*) 200 MHz ANSYS simulations for 3 ft. defect section centered at 50 ft. of 100 ft. three-conductor shielded cable. ..... 42

Figure 9.32. (*left*) 100 MHz and (*right*) 200 MHz ANSYS simulations for 3 ft. defect section centered at 90 ft. of 100 ft. three-conductor shielded cable. ..... 43

Figure 9.33. 100 MHz LIRA simulations for 3 ft. defect section centered at 10 ft. of 100 ft. twisted-pair cable with (*left*) 0.5% stochastic noise and (*right*) 2.5% stochastic noise settings. ..... 43

Figure 9.34. 100 MHz LIRA simulations for 3 ft. defect section centered at 50 ft. of 100 ft. twisted-pair cable with (*left*) 0.5% stochastic noise and (*right*) 2.5% stochastic noise settings. ..... 44

Figure 9.35. 100 MHz LIRA simulations for 3 ft. defect section centered at 90 ft. of 100 ft. twisted-pair cable with (*left*) 0.5% stochastic noise and (*right*) 2.5% stochastic noise settings. ..... 44

Figure 9.36. (*left*) 100 MHz and (*right*) 200 MHz ANSYS simulations of 3 ft. defect section at 25 ft. along 100 ft. three-conductor shielded cable ..... 45

Figure 9.37. (*left*) 100 MHz and (*right*) 200 MHz ANSYS simulations of 3 ft. defect sections at 25 ft. and 75 ft. along 100 ft. three-conductor shielded cable. ..... 45

Figure 9.38. 100 MHz LIRA simulations for defect models consisting of (*left*) 15% capacitance increase at 25 ft. and 5% capacitance increase at 75 ft. and (*right*) additional 15% capacitance increase at 50 ft. for 100 ft. twisted-pair cable. ..... 46

Figure 9.39. (*left*) 100 MHz and (*right*) 200 MHz ANSYS simulations of 3 ft. defect sections at 25 ft., 50 ft., and 75 ft. along 100 ft. three-conductor shielded cable. ..... 46

Figure 9.40. Mechanical defect consisting of 6 in. section of removed jacket and shield along the three-conductor shielded cable ..... 47

Figure 9.41. 100 MHz VNA measurements for defects consisting of 6 in. section of removed jacket and shield (*left*) at 75 ft. and (*right*) at 25 ft., 50 ft., and 75 ft. for 95 ft. three-conductor shielded cable ..... 47

Figure 9.42. 200 MHz VNA measurements for defects consisting of 6 in. section of removed jacket and shield (*left*) at 75 ft. and (*right*) at 25 ft., 50 ft., and 75 ft. for 95 ft. three-conductor shielded cable ..... 48

Figure 9.43. 100 MHz LIRA measurements for defects consisting of 6 in. section of removed jacket and shield (*left*) at 75 ft. and (*right*) at 25 ft., 50 ft., and 75 ft. for 95 ft. three-conductor shielded cable ..... 48

Figure 9.44. 200 MHz ANSYS simulation of 3 ft. defect section at 5 ft. along 100 ft. three-conductor shielded cable ..... 49

Figure 9.45. 200 MHz ANSYS simulation of 3 ft. defect section at 5 ft. along 100 ft. three-conductor shielded cable with 10 ft. impedance-matched extension cable. ..... 50

Figure 9.46. 200 MHz ANSYS simulation of 3 ft. defect section at 5 ft. along 100 ft. three-conductor shielded cable with 10 ft. 50-Ohm extension cable. ..... 51

Figure 9.47. Mechanical defect consisting of 12 in. section of removed jacket and shield along the three-conductor shielded cable ..... 51

Figure 9.48. (left) 100 MHz and (right) 200 MHz VNA measurements of mechanical defect at 5 ft. along 100 ft. three-conductor shielded cable ..... 52

Figure 9.49. 100 MHz LIRA measurement of mechanical defect at 5 ft. along 100 ft. three-conductor shielded cable ..... 52

Figure 9.50. Twisted wire connections made between 10 ft. extension cable and the 100 ft. three-conductor shielded cable under test. ..... 53

Figure 9.51. (*left*) 100 MHz and (*right*) 200 MHz VNA measurements of mechanical defect at 5 ft. along 100 ft. three-conductor shielded cable with 10 ft. identical extension cable. ..... 53

Figure 9.52. 100 MHz LIRA measurement of mechanical defect at 5 ft. along 100 ft. three-conductor shielded cable with 10 ft. identical extension cable. ..... 54

Figure 9.53. ANSYS simulation model consisting of cascaded S-parameter blocks to simulate damaged and undamaged cable segments with different end termination conditions. ..... 55

Figure 9.54. 100 MHz (*left*) ANSYS and (*right*) LIRA simulations of cable terminations for a 100 ft. cable with a 3 ft. defect section at 50 ft. ..... 55

Figure 9.55. 100 MHz LIRA measurements for 100 ft. unshielded three-conductor cable with different types of environmental conditions at the 50 ft. mechanically damaged location. ..... 56

Figure 9.56. ANSYS simulated electric field magnitude at 100 MHz for unshielded cable cross-section (left) in free space and (right) on 0.25in. thick aluminum plate. ..... 57

Figure 9.57. 200 MHz ANSYS simulation of 100 ft. unshielded three-conductor cable supported by (*left*) 6 in. long and (*right*) 12 in. long 0.25 in. thick aluminum plate at 50 ft. ..... 57

Figure 9.58. 200 MHz ANSYS simulation of 100 ft. unshielded three-conductor cable supported by (*left*) 6 in. long and (*right*) 12 in. long 0.25 in. thick carbon steel plate at 50 ft. ..... 58

Figure 9.59. ANSYS simulated electric field magnitude at 100 MHz for unshielded cable cross section (*left*) in free space and (*right*) with fresh water as jacket material. ..... 58

Figure 9.60. 200 MHz ANSYS simulation of 100 ft. unshielded three-conductor cable with jacket modeled as fresh water along (*left*) 6 in. and (*right*) 12 in. sections at 50 ft. ..... 59

Figure 9.61. LIRA simulations of 100 ft. twisted-pair cable with loss tangent of 0.01 and 3 ft. defect section at 50 ft. for (*upper left*) 100 MHz, (*upper right*) 200 MHz, (*lower left*) 400 MHz, and (*lower right*) 1300 MHz. ..... 60

Figure 9.62. LIRA simulations of 100 ft. twisted-pair cable with loss tangent of 0.0001 and 3 ft. defect section at 50 ft. for (*upper left*) 100 MHz, (*upper right*) 200 MHz, (*lower left*) 400 MHz, and (*lower right*) 1300 MHz. ..... 61

Figure 9.63. LIRA simulations of 1000 ft. twisted-pair cable with loss tangent of 0.01 and 3 ft. defect section at 800 ft. for (*upper left*) 10 MHz, (*upper right*) 25 MHz, (*lower left*) 50 MHz, and (*lower right*) 100 MHz. ..... 62

Figure 9.64. LIRA simulations of 1000 ft. twisted-pair cable with loss tangent of 0.02 and 3 ft. defect section at 800 ft. for (*upper left*) 10 MHz, (*upper right*) 25 MHz, (*lower left*) 50 MHz, and (*lower right*) 100 MHz. ..... 63

Figure 9.65. LIRA simulations of 1000 ft. twisted-pair cable with 3 ft. defect section at 800 ft. and dielectric loss tangent of (*left*) 0.0001, (*center*) 0.01, and (*right*) 0.02. ..... 64

Figure 9.66. Test layout of 1000 ft. three-conductor shielded cable used in bandwidth study. ..... 64

Figure 9.67. LIRA measurements of 1000 ft. three-conductor shielded cable using bandwidth of (*upper left*) 10 MHz, (*upper right*) 25 MHz, (*lower left*) 50 MHz, and *(lower right*) 100 MHz. ..... 65

Figure 9.68. LIRA measurements of 1000 ft. three-conductor shielded cable with 1 ft. mechanical defect at 905 ft. using bandwidth of (*upper left*) 10 MHz, (*upper right*) 25 MHz, (*lower left*) 50 MHz, and (*lower right*) 100 MHz. ..... 66

Figure 9.69. LIRA measurements of 1000 ft. three-conductor shielded cable with mechanical defects at 905 ft. using bandwidth of (*left*) 25 MHz and (*right*) 50 MHz. ..... 67

Figure 9.70. VNA measurements of 500 ft. three-conductor shielded cable using bandwidth of (*upper left*) 50 MHz, (*upper right*) 100 MHz, (*lower left*) 150 MHz, and (*lower right*) 200 MHz. ..... 68

Figure 9.71. VNA measurements of 500 ft. three-conductor shielded cable with 1 ft. mechanical defect at 405 ft. using bandwidth of (*upper left*) 50 MHz, (*upper right*) 100 MHz, (*lower left*) 150 MHz, and (*lower right*) 200 MHz. ..... 69

## TABLES

Table 2.1. Advantages and Disadvantages of FDR Testing ..... 3

Table 3.1. Insulation Material for U.S. NPPs (from EPRI 1994) ..... 4

Table 3.2. Categories of Cable Grouping ..... 5

Table 6.1. Cable parameters considered in ANSYS FDR simulation models ..... 16

Table 7.1. Cable parameters considered in Wirescan LIRA FDR simulation models ..... 18

Table 9.1. Influence of cable insulation dielectric constant changes on characteristic impedance of shielded three-conductor cable segment. ..... 26

# ACRONYMS AND ABREVIATIONS

| | |
|---|---|
| AMP | Aging Management Program |
| AMS | Analysis and Measurement Services |
| c | speed of light or 299792458 m/s |
| CPE | chlorinated polyethylene |
| CSPE | chlorosulphonated polyethylene (Hypalon) |
| DBE | design-basis event |
| Dk | dielectric constant |
| Df | dissipation factor |
| EAB | elongation at break |
| EPR | ethylene propylene rubber |
| EPRI | Electric Power Research Institute |
| FDR | frequency domain reflectometry |
| LIRA | line resonance analysis |
| LOCA | loss-of-coolant accident |
| LWRS | Light Water Reactor Sustainability Program |
| NDE | nondestructive evaluation |
| NPP | nuclear power plant |
| NRC | U.S. Nuclear Regulatory Commission |
| PNNL | Pacific Northwest National Laboratory |
| PVC | polyvinyl chloride |
| S/m | Siemens/meter |
| SLR | subsequent license renewal |
| TDR | time domain reflectometry |
| TEM | transverse electromagnetic |
| VNA | vector network analyzer |
| XLPE | cross-linked polyethylene |

# 1. OBJECTIVES

This Pacific Northwest National Laboratory (PNNL) milestone report describes progress to date on the investigation of nondestructive test methods focusing particularly on a physics-based modeling approach to qualitatively and quantitatively characterize cable anomalies and their frequency domain reflectometry (FDR) response. The work includes:

a. a review of FDR theory and relevant prior modeling publications

b. a description of the finite element method (FEM) models used to characterize normal and damaged cable system geometry and material model properties

c. transfer of those properties to distributed circuit models for characterizing expected FDR responses

d. experimental work to benchmark specific model cases

e. parametric adjustment of the model to examine potentially interesting cable degradation cases.

This report is submitted in fulfillment of deliverable M3LW-17OR040402 – Physics-Based Model of Cable Insulation Condition for Frequency Domain Reflectometry (FDR).

This work is part of an overall project to develop the technical basis for assessing the level and impact of cable insulation aging and degradation in nuclear power plants (NPPs). PNNL has developed capabilities for thermal radiation, and combine thermal and radiation aging of cables as well as significant capability to test and evaluate cable condition (Fifield et al. 2015; Glass et al. 2015). In July 2012, a workshop was held to lay the groundwork for a research and development roadmap to address aging cable management in NPPs particularly focused on nondestructive examination (Simmons et al. 2012). A phased approach was decided to address three particular topics:

1. Determination of key **indicators** of cable aging. This has largely been addressed in earlier reports (Simmons et al. 2014; Ramuhalli et al. 2015).
2. Characterize and advance current nondestructive evaluation (NDE) methods and develop new NDE methods by using insights from determination of key indicators. Although work on this topic continues, activity to date has been generally addressed by Glass et al. (2015) describing the overall state of the art for both bulk and distributed electrical tests and local tests. Separate reports focusing on local tests (Glass et al. 2016a) and electrical tests (Glass et al. 2016b) were also prepared.
3. Develop models that use the advances in key indicators and NDE methods to assist in predicting remaining useful life of cables. This work is also ongoing but this report constitutes one specific modeling activity under this topic.

# 2. INTRODUCTION AND BACKGROUND

Most NPPs have already extended their operating licenses from their initial license period of 40 years to 60 years. Associated with this license extension, some form of cable aging management program (AMP) has been adopted. As NPPs consider applying for second, or subsequent, license renewals (SLR) to extend their operating period from 60 years to 80 years, it is important to understand how the materials installed in plant systems and components will age during that time and develop more consistent AMPs to assure continued safe operation under normal and design-basis events (DBE).

Degradation of the cable jacket, electrical insulation, and other cable components of installed cables within NPPs is known to occur as a function of age, temperature, radiation, and other environmental factors. Although system tests verify cable function under normal loads, concern remains over cable performance under exceptional loads associated with DBEs. The cable's ability to perform safely over the initial 40-year planned and licensed life has generally been demonstrated and there have been very few age-related cable failures (EPRI 2015; Mantey 2015). With greater than 1000 km of power, control, instrumentation, and other cables typically found in an NPP, replacing all the cables would be a severe cost burden. License renewal to 60 years and SLR to 80 years, therefore, requires a cable AMP in accordance with regulatory guidance (NRC 2012) to justify cable performance under normal operation as well as accident conditions.

Acceptance criteria that define the threshold for degradation below which cables may continue to be used are a challenge, because it is impractical to subject each cable system to loss-of-coolant accident (LOCA) or seismic simulation events following 40+ years of service. The report *Initial Acceptance Criteria Concepts and Data for Assessing Longevity of Low-Voltage Cable Insulations and Jackets* (EPRI 2005) develops a basis for acceptance criteria and evaluates the aging profiles for many commonly used cable jackets and polymers. The report describes 50% elongation at break (EAB) as a conservative practical end-of-life threshold for cables that may be stressed during maintenance or subjected to LOCA exposure. The report also discusses the basis for cautious continued use of cables beyond the 50% EAB threshold. EAB inherently compromises the in-service cable use as it is a destructive ex-situ test, so the challenge is to develop NDE methods that can reasonably be correlated with EAB. Reliable NDE in-situ approaches are needed to objectively determine the suitability of installed cables for continued service. A variety of tests are available to assess various aspects of electrical and mechanical cable performance, but none of the available tests are suitable for all cable configurations nor does any single test assess all features of interest. Nevertheless, the complete collection of test possibilities offers a powerful range of tools to assure the integrity of critical cables.

One test that has attracted significant attention in recent years is frequency domain reflectometry. This is a low-voltage nondestructive test that can be applied at a cable end. Testing from the cable end is important because local inspection all along the cable length is frequently very difficult, because cables are routed within trays, conduits, underground, and through walls thereby limiting physical access. FDR has been shown to locate cable insulation damage due to thermal, radiation, and mechanical damage. PNNL has evaluated several types of FDR test equipment to produce the general observations shown in Table 2.1 (Glass et al. 2016b):

Understanding exactly what kind of damage will produce detectable results is not well quantified and experimental generation of the very wide range of damage scenarios is expensive. Not only must cable segments be artificially aged or damaged, but these aged or damaged segments must be contiguous within relatively long (>15 m) cable lengths to allow meaningful FDR measurements. Thus a physics-based model approach to characterize cable anomalies and their FDR responses has been developed to help address this knowledge gap. This model has been benchmarked with several experimental verification cables in which well-understood damage mechanisms were compared with the model predictions.

Table 2.1. Advantages and Disadvantages of FDR Testing

| | |
|---|---|
| Advantages | • Inspection of entire cable length from single-ended access<br>• Low voltage safe, nondestructive test<br>• Rapid inspection times (several minutes)<br>• Systems commercially available<br>• Sensitive detection and location of localized degradations<br>• In most cases, there is no need to de-terminate cable ends |
| Disadvantages | • Global aging indicators still in development for correlation to established methods<br>• Baseline data sets helpful to assess cable condition<br>• Specialized training required for system operation and data analysis<br>• Cannot currently be used on energized cables |

# 3. CABLE DESIGN, CLASSIFICATION, AND LAYOUT

NPP cable designs typically include a conductor to carry power, instrumentation or control signals, and an insulating cover layer to isolate the conductor (Figure 3.1). They may include more than one insulated conductor within a bundle. Other components typically associated with the overall cable design include a semiconductor screen, a shield over each conductor and/or over all conductors, binder tape, and a jacket. While the insulation provides electrical isolation, in jacketed cable configurations the jacket mainly serves to provide mechanical protection during installation and sometimes fire or moisture resistance depending on the cable construction.

The materials for cable components are chosen based on the use environment, such as wet, dry, radiation, or sunlit conditions, and the application such as for power or instrumentation. Conductors, made from copper, aluminum, or tin, are relatively insensitive to age and related damage. Cross-linked polyethylene (XLPE) and ethylene propylene rubber (EPR) compose the vast majority of insulation materials in the nuclear industry, with silicone rubber also being of interest. The most significant jacket materials are chlorosulphonated polyethylene (CSPE – also known as Hypalon® [registered trademark of DuPont]), polychloroprene, and polyvinyl chloride (PVC). While installed cables with intact insulation may well be able to continue to provide safe operation with degraded jacket material, the tendency of jacketing materials to degrade more readily than insulation materials enables their use as lead indicators for local stress prior to insulation degradation and failure.

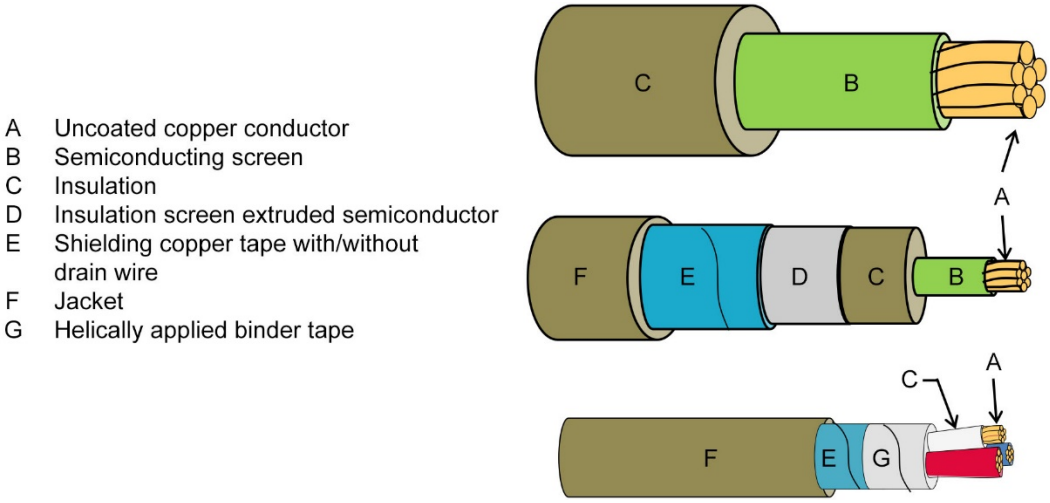


Figure 3.1. Configurations of typical cable designs used in NPPs.

A survey performed by EPRI in the mid-1990s established a representative distribution of insulation materials within the U.S. nuclear fleet (EPRI 1994) (see Table 3.1). Note that over 70% of the materials are XLPE or EPR.

Table 3.1. Insulation Material for U.S. NPPs (from EPRI 1994)

| Insulation Material | Database Entries | Percent of Total (%) | Insulation Material | Database Entries | Percent of Total (%) |
|---|---|---|---|---|---|
| XLPE | 439 | 36 | ETFE | 39 | 3 |
| EPR | 434 | 36 | Flame retardant | 36 | 3 |
| Silicone Rubber | 63 | 5 | CSPE | 28 | 2 |
| Kerite | 61 | 5 | Butyl rubber | 20 | 2 |
| Polyethylene | 52 | 5 | All others | | Each ≤ 1% |

Numerous standards have been developed over the years to group and categorize cables based on application, voltage, environment, and basic design type (Table 3.2). Exactly what grouping is used depends on the application but for cable aging management, generally the nuclear industry has focused on medium- and low-voltage cables. Low-voltage cables constitute the majority of NPP cables, but many safety-critical cables exposed to moisture are medium-voltage cables. Most plants have a rigorous program to test and verify performance of safety-critical medium-voltage cables. Cable condition monitoring programs are encouraged through the U.S. Nuclear Regulatory Commission's (NRC) Draft. Regulatory Guide 1240 (NRC 2010) with particular emphasis on medium-voltage cables citing examples of cable failures particularly for wet environment cables. Although this is not currently a required program, it is encouraged by the NRC "*to promote discussion between staff and licensees when a facility's operating experience indicates cable failure or degraded cable performance as a causal factor. The NRC staff will use this guidance to evaluate compliance with the Maintenance Rule*."

Table 3.2. Categories of Cable Grouping

| Application | Voltage | Environment | Design |
|---|---|---|---|
| Power | Low (≤2 KV) | Normal operating temperature | Single/multi-conductor |
| Control | Medium (≤2–46 KV) | High temperature | Triplex |
| Instrument | High (>46 KV) | Fire/flame retardant | Thermocouple alloys |
| Thermocouple | | High radiation | Coaxial |
| Communication | | Submerged – water | Shielded/unshielded (and shield type – tape, braid, …) |
| Specialty Configuration | | Aggressive solvents | Special jacket |
| Safety Related | | | Conductor/shield material (copper, tinned copper, aluminum, …) |
| Non-Safety Related | | | Insulation/jacket material (XLPE, EPR, PVC, …) |

Cable termination and splice kits also represent sensitive sites for cable system failure. Designs include screw-clamp or crimp-clamp connections between the conductor and the solid metal part of the splice or terminations usually coupled with an insulating shrink-wrap or tape to seal and electrically isolate the metal parts. With respect to wet or dry aging, splices and terminations are expected to have very long lives if they are made in accordance with manufacturers' recommended procedures. This means that crimps and bolted connections have been made properly and that the tapes have been properly applied to the correct thickness and with the appropriate tension, or that heat-shrink materials have been properly applied and completely shrunk in place. Given that no voids exist, the splice and termination insulation is thicker than that of the cable and generally has ratings equal to or greater than the cable insulation. Generally when splices or terminations fail, it is because of an installation error. Such errors include inadequate removal of semiconducting layers, cuts to the insulation under the splice, voids from inadequate taping or heat-shrink practices, and/or the presence of dirt in the splice layers. If mechanical metal-metal connections are not made properly, the connections can loosen over time thereby increasing the connection resistance due to vibration and/or corrosion-based contact-force loss. Many of these workmanship-related failures do not occur on initial energization and may take years to manifest themselves in a cable failure.

This aspect of the cable design has been studied and these junctions have been subjected to aging and LOCA performance tests (Lofaro and Villaran 2002) similar to the full tests. In fact, some form of termination must be included in the full cable tests. In addition, these cable terminations are subject to workmanship-based performance issues and are carefully considered as potential failure points during periodic condition monitoring activity. As a practical matter, whenever cables need to be de-terminated for testing, new termination kits are frequently applied. Because of the bulk of larger diameter cables and practical reel size limitations, splices may be necessary for long cable runs. The main concern for power

connections is that a high-resistance connection does not occur. Infrared-camera thermographic-aided visual inspections are frequently employed to determine if problems (hot spots) exist. Such overheating can cause the insulation and connection tape or heat-shrink to degrade or the connection to burn open over time.

Cable layout in typical plants is not designed to facilitate access and inspection of much of the cable lengths. Cable trays and conduits are designed to protect the cables from environmental stresses as well as accidental damage from workers and equipment that may be moving either inside containment, auxiliary buildings, or control buildings. While cable ends are generally accessible at termination boxes and control panels, many cables are grouped together with other cables in trays that do not necessarily follow personnel access pathways, pass-through penetration pipes and conduits that may be buried in concrete, underground, or even passing through areas that may be flooded (Figure 3.2).

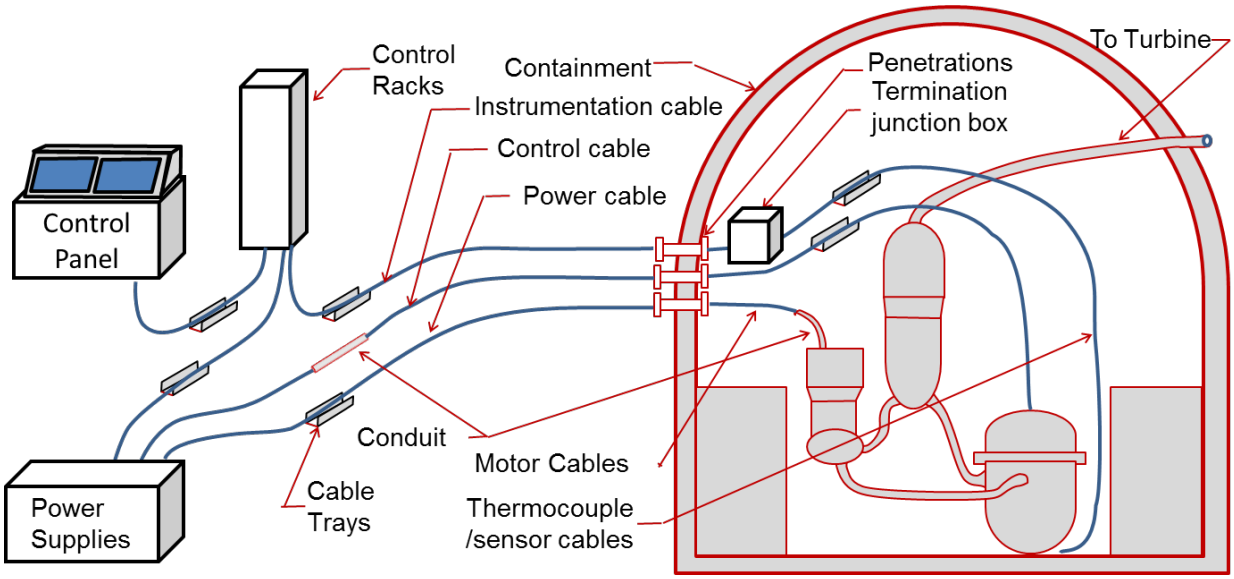


Figure 3.2. Typical cable layout allows access at control racks and termination junction boxes but much of the cable is protected within cable trays and conduit thereby limiting access for local inspections.

# 4. FREQUENCY DOMAIN REFLECTOMETRY THEORY

Frequency-domain reflectometry is a nondestructive electrical inspection technique used to detect, localize, and characterize subtle impedance changes in power and communication system conductors along the length of a cable from a single connection point. FDR is based on the interaction of electromagnetic waves with conductors and dielectric materials as they propagate along the cable. The technique uses the principles of transmission line theory to locate and quantify impedance changes in the cable circuit. These impedance changes can result from connections, faults in the conductors, or degradation in the cable polymer material (Furse et al. 2003; Agilent 2012). FDR theory is addressed generally in this section and then the implementation of this theory is addressed specifically for typical instruments used to measure the FDR response.

For the measurement, two conductors in the cable system are treated as a transmission line through which a low-voltage swept-frequency waveform is propagated. As the excitation signal is swept over the frequency range and the associated electromagnetic wave travels down the cable, the impedance response is recorded at each frequency to characterize the wave interaction with the conductors and surrounding dielectric materials. The remote end of the cable can be terminated in arbitrary impedance different from the cable characteristic impedance, but is often grounded or open-circuited during the testing. Because the applied signal is low-voltage, the test is completely nondestructive and poses no special safety concerns to operators assuming that routine electrical safety procedures are followed. Note that in most cases, it is only necessary to de-energize the cables and de-termination is not required, but typically one end of the cabling is de-terminated to connect the FDR system. Only de-terminating one cable end can be an advantage over many other techniques by shortening the required testing time and minimizing the risk of improper re-termination. Frequently, however, both ends of the cable systems are de-terminated anyway to minimize the risk of residual charge shock.

Figure 4.1 shows a linearly increasing “chirp” sinusoidal waveform that is representative of the type of excitation signal used in the FDR technique. The excitation signal can be generated for transmission into the cable using an analog circuit such as a voltage-controlled oscillator or using a digital circuit such as a direct digital synthesizer.

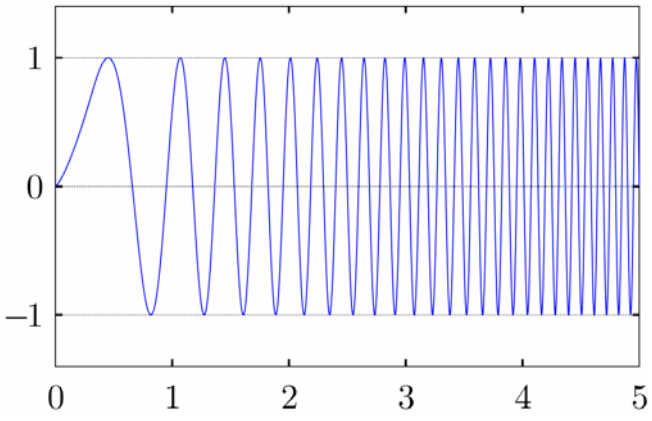


Figure 4.1. Example FDR excitation waveform in which the signal frequency linearly increases as a function of time.

Figure 4.2(a) shows a representation of the electric and magnetic vector field components for a propagating sinusoidal transverse electromagnetic (TEM) wave. For TEM waves traveling on a transmission line, the electric and magnetic fields are orthogonal to each other as well as the direction of propagation. Figure 4.2(b) shows cross-sectional views of the electric and magnetic field configurations for TEM waves traveling on coaxial and two-wire transmission lines. The electric fields start and end on current-carrying conductors and are influenced by dielectric materials and other metals. The magnetic fields form closed loops around current-carrying conductors and are influenced by magnetic materials.

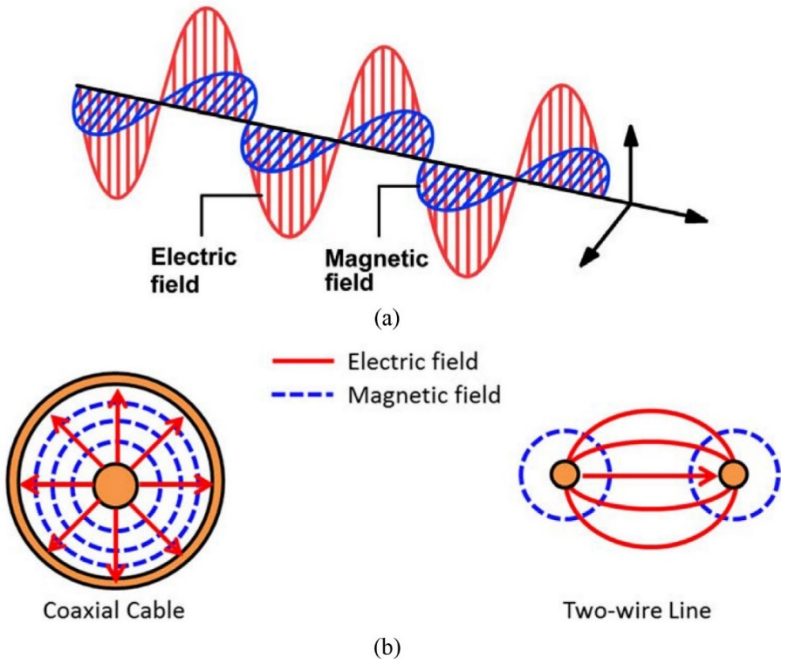


Figure 4.2. (a) Electric and magnetic field configurations for generalized sinusoidal TEM wave propagation. (b) Electric and magnetic field configurations for specific cable types.

Where TEM wave propagation analysis may be complicated by unknown and changing electromagnetic properties of the waveguide, for most practical applications a simplified form of analysis referred to as transmission line theory is sufficient. In transmission line theory, the electric fields relate to distributed (per unit length) capacitance and the magnetic fields relate to distributed inductance. The resistance of the metallic conductors and dielectric loss in the insulation attenuate the signal as it propagates along the cable. A schematic representation of the standard transmission line model is shown in Figure 4.3, where the distributed circuit elements representing an infinitesimally short length may be cascaded with similar elements to model the overall behavior of the line. In the FDR method, an inverse Fourier transform coupled with the cable velocity factor is used to obtain the range domain data, which contains information on the wave interactions with the cable's resistive, inductive, and capacitive material and which identifies the physical location of signal reflections (Minet et al. 2010).

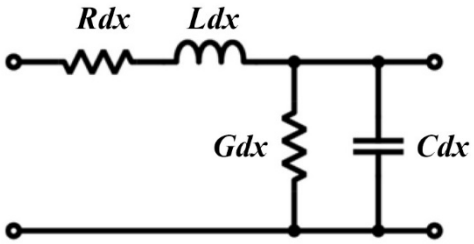


Figure 4.3. Transmission line RLGC circuit model consisting of distributed impedance elements over an infinitesimally short length.

The FDR technique can potentially yield better sensitivity to cable degradations than traditional time domain reflectometry (TDR), which is traditionally suited for identifying open and short circuit conditions in the conductors (Murty 2013). For example, FDR is less susceptible to electrical noise and interference due to the availability of filtering and noise-lowering algorithms in the frequency domain (IEC 2002). This can lead to increased sensitivity and accuracy. The FDR method can have a high dynamic range. Additionally, FDR is suited for identifying and characterizing a series of multiple

degradations for long cables because TDR pulses may have difficulty continuing in the forward direction after several significant reflections or multiple reflections may complicate the correlation between the impedance change and the corresponding location on the reflectometry waveform.

The spatial resolution is an important parameter for detection and localization of cable defects. The range resolution is a function of the swept-frequency bandwidth (BW), the speed of light (c), and the velocity factor (VF) of the cable (Mohr and Associates 2010):

$$\text{Resolution (m)} = (c \times VF) / (2 \times BW) = 1.5E8 \times (VF/BW) \quad (4.1)$$

where c = 3E8 m/s. The cable's VF is a value less than unity and is inversely related to the square root of the dielectric constant of the insulation material. As an example, using a 200 MHz FDR bandwidth to inspect a coaxial cable with a velocity factor of 66% results in a 0.5 m resolution as shown below:

$$\text{Resolution} = 3E8m * 0.66/ (2*2E8) = 0.5m = 1.6 \quad (4.2)$$

The maximum unambiguous (alias-free) range is also a factor for interpreting FDR results, and is a function of the resolution and the number of frequencies (NF) used to cover the bandwidth (Mohr and Associates 2010):

$$\text{Range (m)} = \text{Resolution} \times NF \quad (4.3)$$

An important parameter in the implementation of the FDR method is the bandwidth of the swept-frequency signal that propagates along the cable. A higher bandwidth waveform allows for increased detection sensitivity, a shorter termination shadow, and improved localization of degradations due to better spatial resolution. However, higher bandwidth signals are more susceptible to signal attenuation along the cable, which can limit the inspection length. If the maximum frequency is too low, the cable length will not be sufficient to be treated as a transmission line and the measurement may not produce meaningful results. Typically, the electrical length of the cable should be at least one wavelength of the signal propagating along the cable in order to apply radio-frequency transmission line theory. Thus, higher frequencies are required to characterize shorter cables in order to satisfy the cable length requirement, and lower frequencies are required to characterize longer cables in order to prevent the insertion loss from overcoming the measurement signal.

Figure 4.4 shows a simplified diagram and example data processing flow for an FDR system, which collects and processes the cable data for aging/damage evaluation.

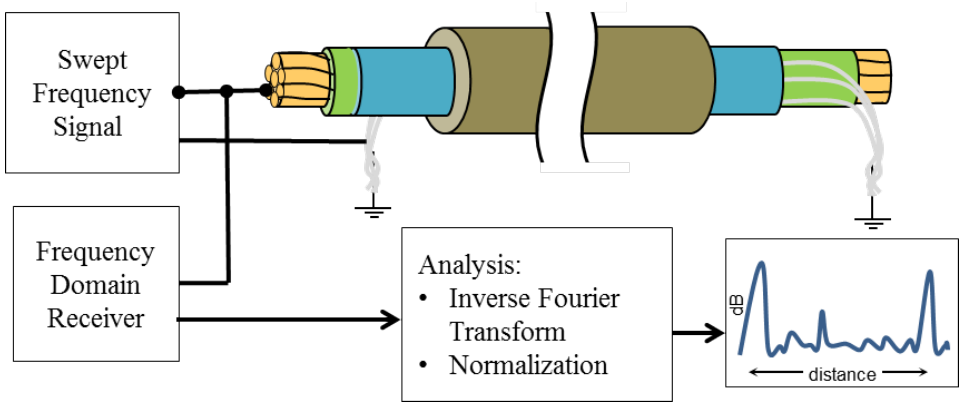


Figure 4.4. Block diagram of FDR instrument and cable test arrangement.

The signal reflections measured by the FDR system are caused by changes in the characteristic impedance (Z0) along the length of cable that can be attributable to physical changes such as cuts, gouges, and excessive bending or aging-related degradation of the cable insulation material caused by thermal and radiation aging. As an example, the characteristic impedance of the twisted-pair cable shown in Figure 4.5 can be calculated using the following equation (EEWeb 2015):

$$Z_0 = \frac{120}{\sqrt{\varepsilon_r}} \times \ln\left(\frac{2S}{D}\right) \tag{4.4}$$

where S is the distance between the two conductors, D is the conductor diameter, and $\varepsilon_r$ is the relative permittivity of the insulation material.

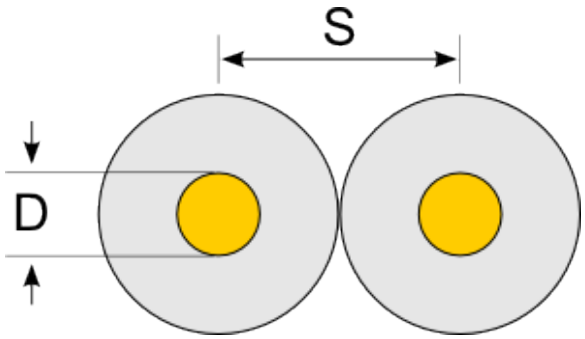


Figure 4.5. Cross-section view of commonly used twisted-pair cable.

Based on this equation, the parameters that could create a change in characteristic impedance are the physical dimensions and the relative permittivity of the insulation material. Physical damage to the jacket material or excessive bending would cause changes in the spacing of the cable conductors. Because there is no significant change in the spacing or diameter of the conductors during the aging process, the relative permittivity is the only remaining variable that could change the impedance and cause reflections in FDR data. The relative permittivity is directly related to the capacitance of the cable using the insulation material as the dielectric media:

$$C\left(pF/inch\right) = \left(\frac{0.7065}{\ln\frac{2S}{d}}\right) \times \varepsilon_r \tag{4.5}$$

The capacitance changes from insulation aging can be trended over time using the FDR measurement. The reflections of the FDR signal are converted from the frequency to the time domain using an inverse fast Fourier Transform. In the time domain, the impulse response data is further enhanced by integrating over time to obtain the step response. The result of the integral is expressed in terms of the reflection coefficient ($\rho$) as:

$$\rho = \frac{\mathrm{V}_{\mathrm{reflected}}}{\mathrm{V}_{\mathrm{incident}}}. \tag{4.6}$$

The distance to fault is calculated using the velocity factor for the cable, which is a percentage of the speed of light in a vacuum and is determined by the relative permittivity of the cable's insulating material. Distance to fault can be determined by multiplying the signal propagation velocity of the cable ($V_P$) by half the time it takes for the incident wave to travel to the impedance change and be reflected back to the signal generator:

$$\text{Distance} = \frac{V_P T}{2}. \tag{4.7}$$

In general, FDR data can be viewed in two forms—referred to as the impulse response and the step response depending on the desired analysis to be performed. The impulse response, $h(t)$, is given per the equation below by the inverse Fourier transform of the transfer function where $H(f)$ is the FDR return loss as a function of frequency.

$$h(t) = \int_{-\infty}^{\infty} H(f) e^{j2\pi ft} df \tag{4.8}$$

The step response, $f_{step}(t)$, is given by integration of the impulse response, shown below.

$$f_{step}(t) = \int_{-\infty}^{\infty} h(t) dt \tag{4.9}$$

Figure 4.6 through Figure 4.8 provide example impulse response and step response FDR presentations. Figure 4.6 and Figure 4.7 are sample data provided over two different frequency bandwidths for the same measured cable response. Figure 4.8 shows the impulse and step response for the mechanically damaged cable discussed in Section 9. In general, results in this study use the impulse response representation.

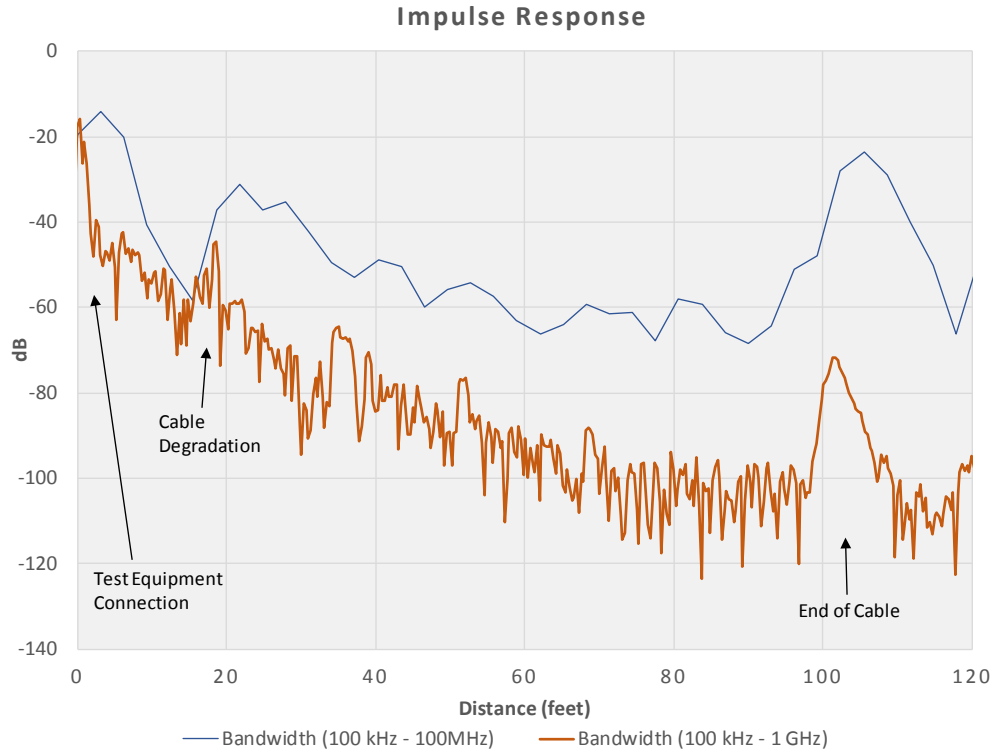


Figure 4.6. Example FDR impulse response data. Figure courtesy of AMS Corporation.

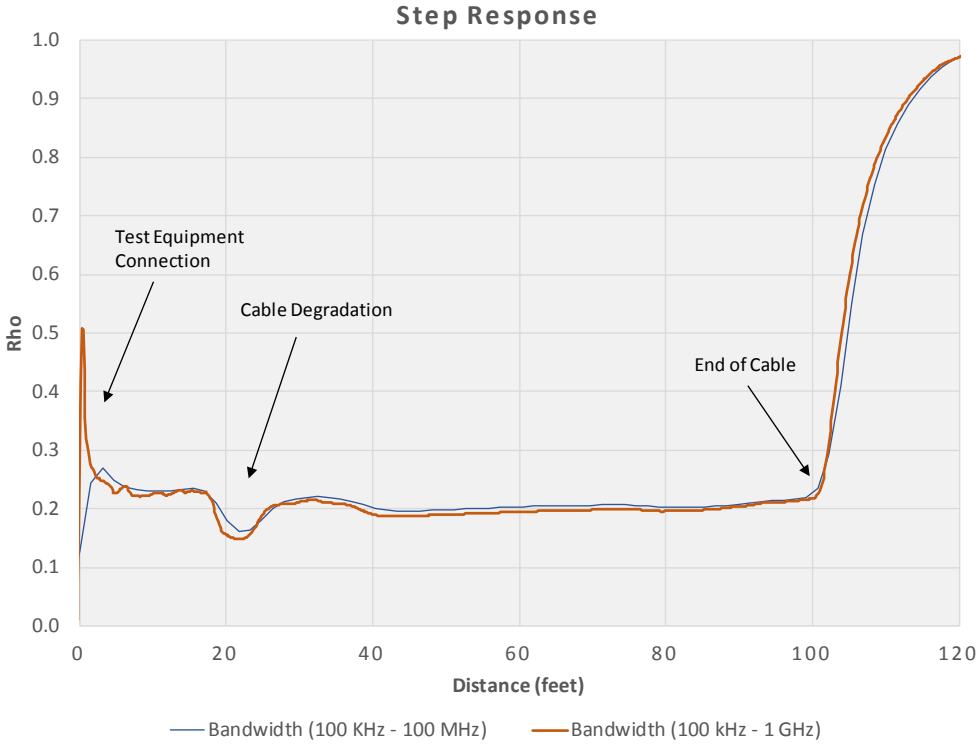


Figure 4.7. Example FDR step response data. Figure courtesy of AMS Corporation.

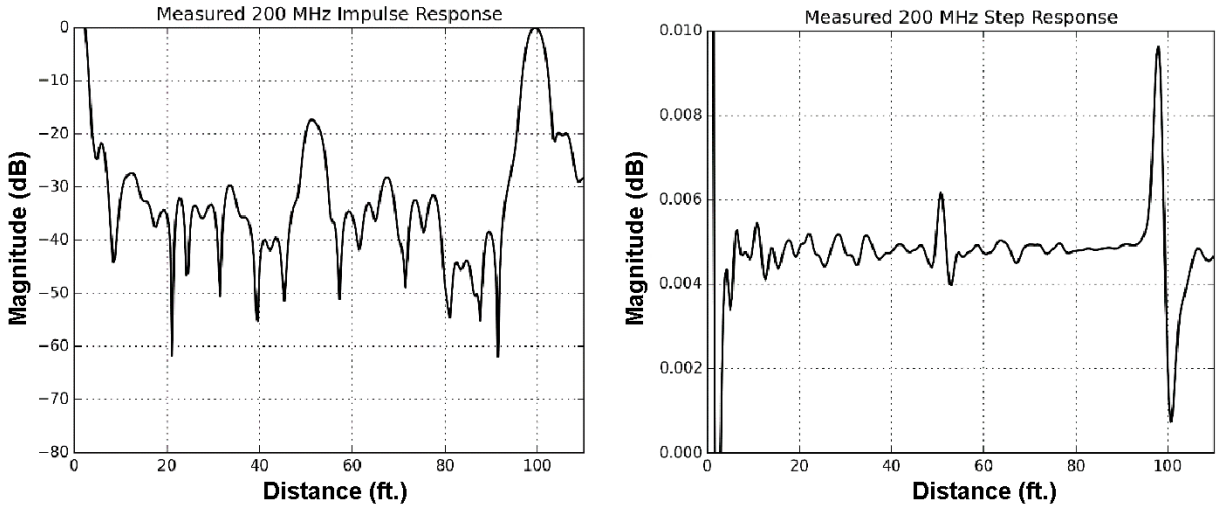


Figure 4.8. Measured FDR response for shielded triad cable with mechanically damaged defect as described in Section 9 at mid-point in the cable shown as: (*left*) impulse response and (*right*) step response.

# 5. CABLE AND FDR MODELING LITERATURE REVIEW

Cable modeling has been extensively used for cable system design. Several commercial FEM simulation tools include dedicated electromagnetic modules that are tailored for cable modeling and analysis (ANSYS 2014; Strikwerda 2016). These software packages offer both two- and three-dimensional modeling capability. Design inputs include conductor material and geometry, insulation permittivity and geometry, and signal frequency. This allows for calculation of multiple parameters relative to cable design including electric and magnetic field strengths for the given input and the effective cable capacitance per unit length. Many researchers have used these modeling tools to predict cable characteristics and performance and to characterize defects in cables. The following summary does not provide a comprehensive review of pertinent literature, but is intended to provide examples of prior work relevant to the current simulation study.

As early as 1984, FEM tools were used at Fermi National Accelerator Laboratory to calculate transmission line impedances and capacitance for two conductor systems (Johnson 1984). Cases considered included coaxial, off-centered coaxial, and two paired conductor systems.

The researchers in Chen et al. (2014) applied FEM tools to characterize a water-tree damaged section of cable insulation and to image the altered electric field in the region of the water tree. The model was parametrically varied to characterize capacitance of the water-tree affected area versus the percent growth of the water-tree across the insulation.

Collaborators from Sebha University and Glasgow Caledonian University used COMSOL software to characterize the electric field for an 11 kV armored XLPE cable insulation containing air-filled void defects (Alsharif et al. 2012). The 2D electrostatic simulation showed a map of the electric field strength within the XLPE cable insulation. The void defect strongly affected the electrostatic field strength and geometric distribution.

Researchers at Sandia National Laboratory have studied submerged medium-voltage cable systems. As part of this effort they have presented a circuit model for a coaxial cable (Brown et al. 2015). This work includes a review of several references where circuit models are developed (Eriksson et al. 2006; Kuan et al. 2011).

Researchers at Iowa State University have recently developed COMSOL models of single- and three-core cable for the purpose of determining the sensitivity of capacitive sensing techniques to changes in cable insulation permittivity as the material ages. For the purpose of designing an interdigital capacitive sensor with optimal sensitivity to insulation permittivity changes, when measured from the jacket exterior, a three-layer COMSOL model was configured with metal core (the conductor), polymer insulation, and polymer jacket layers.[(a)] The voltage distribution applied to a three-core cable was also modeled in COMSOL in order to determine how best to concentrate electrical energy in the insulation, for the purpose of optimizing sensitivity to insulation permittivity changes as the material ages (Imperatore 2017).[(b)]

(a) Shao ZH and N Bowler. 2017. "Capacitive Nondestructive Evaluation of Aged Cross-Linked Polyethylene (XLPE) Cable Insulation Material." To be presented at *18th International Conference on Environmental Degradation of Materials in Nuclear Power Systems – Water Reactors*. August 13–17, 2017, Portland, Oregon. The Minerals, Metals & Materials Society.

(b) Imperatore MV, LS Fifield, D Fabiani and N Bowler. 2017. "Dielectric Spectroscopy on Intact PVC/EPR Multipolar Cables." To be presented at *2017 IEEE Conference on Electrical Insulation and Dielectric Phenomena (CEIDP)*. October 22–25, 2017, Forth Worth, Texas. IEEE.

PF Fantoni has published extensively on the line impedance resonance analysis (LIRA) FDR method including measurement examples, and modeling associated with NDE. One significant report (Fantoni and Nordlund 2006) includes a discussion of the LIRA simulator in which cables are modeled using cascaded equivalent circuit-model segments. Most of the segments are similar and represent undamaged cable. The circuit model values are calculated based on inputs that can include segment length, conductor material and diameter, insulation dielectric properties, distributed capacitance, and distributed inductance. The characteristics of a damaged segment are different primarily due to the change in cable capacitance within the damaged segment. The LIRA simulator applies the same kind of input to this circuit model as is used in the actual measurement instrument to simulate the theoretical cable measurement response. The commercial version of this LIRA simulator is one of the methods used to predict cable responses in this report.

# 6. FINITE ELEMENT SIMULATION MODEL

A co-simulation approach based on ANSYS High Frequency Structure Simulator (HFSS) as the electromagnetic FEM simulator and ANSYS Nexxim as the circuit simulator was used to model scenarios representative of NPP cable systems. ANSYS HFSS was first used to rigorously solve Maxwell's equations for 3D models representing damaged or undamaged cable sections. Examples of these HFSS models are shown in Figure 6.1 where the cable jacket is rendered partially transparent so the insulation and wires are visible.

Figure 6.1. Example ANSYS HFSS simulation models representing segments of (left) three-conductor shielded cable and (right) coaxial cable.

The frequency-domain scattering parameters were then extracted from each HFSS model to provide physics-based building blocks, which can be combined to investigate a variety of defect scenarios. Scattering parameter matrices are a well-established method based on incident and reflected waves, which accurately characterize the properties of an electrical network. Finally, the simulated FDR response for a specific scenario was obtained from an ANSYS Nexxim circuit model of cascaded scattering parameter datasets corresponding to damaged or undamaged cable sections. This cascaded network model allows analysis of an arbitrary number of independently characterized structures.

An example circuit schematic is shown in Figure 6.2 where the FDR input port is located on the upper left. and the defect cable segments are represented by the four scattering parameter blocks in the center. The groups of scattering parameter blocks on the left. and right halves of the schematic represent the much longer undamaged sections of the cable. In this example, the data in each block represents a section consisting of one lay length (360-degree revolution) of a multi-conductor cable.

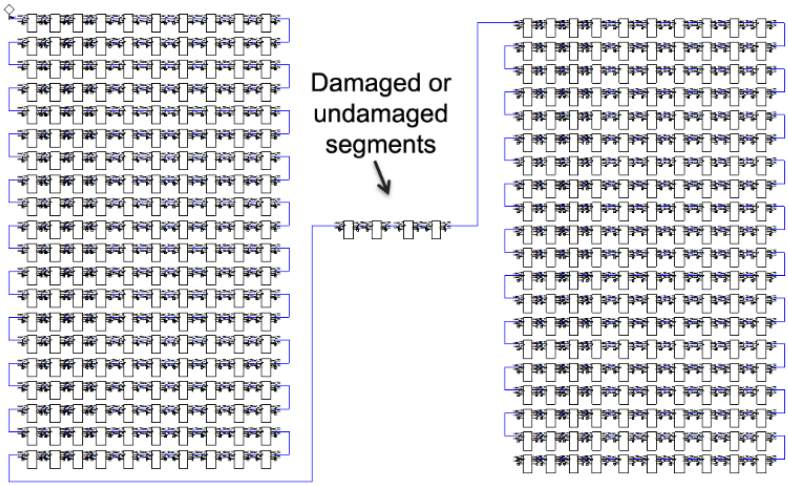


Figure 6.2. Example ANSYS Nexxim co-simulation model showing cascaded scattering parameter blocks containing HFSS results for damaged or undamaged cable segments.

In all simulation cases, the cable orientation is assumed to be straight along the entire length of the cable layout. The frequency domain circuit simulation response from Nexxim was converted to the range domain using an inverse Fourier transform to create the cable signature. This modeling approach provided a computationally efficient method to study FDR responses of highly detailed 3D models representing short sections of cable runs that can be many electrical wavelengths long in the overall cascaded model. For the purposes of this study, a total cable length of 100 ft. was generally used, which is representative of the cables provided for the FDR measurement study in PNNL0-25634 (Glass et al. 2016b).

Two different cable types were modeled in this study—1) an RG-58 coaxial cable and 2) a General Cable FR-EPR/chlorinated polyethylene (CPE) three-conductor shielded cable. The relevant design parameters shown in Table 6.1 were used to model the 3D cable geometries in ANSYS HFSS.

Table 6.1. Cable parameters considered in ANSYS FDR simulation models

| Parameter | 600 V Shielded Triad Cable | RG-58 Coaxial Cable |
|---|---|---|
| Conductor | Copper, 16 AWG, 1.52 mm diameter, 76 mm lay length (twist rate) | Copper, 0.91 mm diameter |
| Insulation | EPR, Dk = 3, 0.64 mm thick | PE, Dk = 1.98, 1.02 mm thick |
| Shield | Copper | Copper |
| Jacket | CPE, Dk = 2.25, 1.14 mm thick | PVC, Dk = 2.7, 0.75 mm thick |
| Outer Diameter | 8.31 mm | 4.95 mm |
| Loss | Insulation Df = 0.025 | 0.161 dB/m at 100 MHz |
| Dk=dielectric constant; Df=dissipation factor; EPR= ethylene-propylene rubber; PE=polyethelene | | |

The cable models can also include a component of stochastic noise to simulate a representative noise floor that would be encountered in an actual measurement. This noise contribution is not the electrical noise associated with the measurement, but rather the normal variation in reflected signals associated with impedance changes along the cable from material and geometrical variations in the conductors and insulation. The cable fabrication tolerance produces random fluctuations in electrical parameters along the cable length. These small differences in cable construction (twist rate, conductor or insulation dimensions, dielectric properties, etc.) can set a threshold for the FDR defect detection.

Selection of an appropriate stochastic noise level depends highly upon the specific cable that is being evaluated. In this case, cable measurements provided an indication of a noise floor that could be utilized for modeling purposes. A similar noise level assignment is available in both the ANSYS and the LIRA simulator. In many simulation cases, no stochastic noise was used in the ANSYS simulation so that small reflections due to the defect phenomena under study would be visible and clearly interpreted.

# 7. WIRESCAN LIRA SIMULATOR

In addition to the electromagnetic/circuit co-simulations described in the previous section, a commercial FDR simulator was used to examine predicted responses for cable defect scenarios. The Wirescan LIRA instrument includes a simulator module that is based on the analysis of cascaded transmission line segments. Figure 7.1 shows the user interface of the LIRA Simulator module.

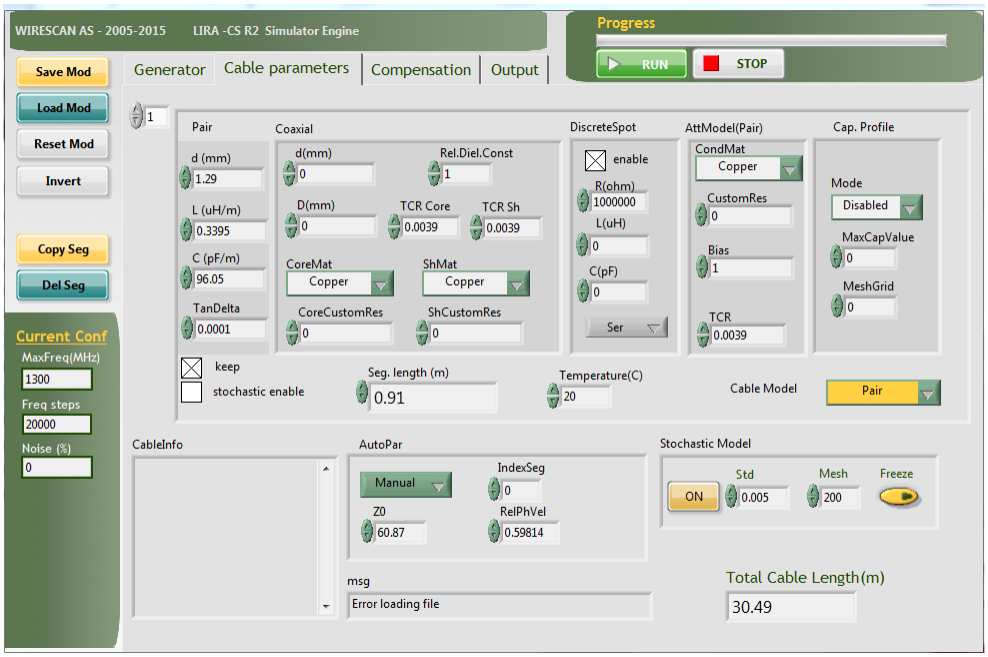


Figure 7.1. Wirescan LIRA simulator for modeling FDR responses of coaxial and twisted-pair cable configurations.

Available cable types in the LIRA simulator are limited to coaxial or twisted-pair configurations. The analysis is based on analytical formulas describing electrical characteristics as a function of parameters such as conductor size, insulation type, and other dimensions. For coaxial cable, a damaged segment can be represented by changing the insulation dielectric constant value. For twisted-pair cable, a damaged segment can be represented by a change in the distributed capacitance value. The simulator uses these inputs to calculate an FDR response for the overall cable model. The results of the LIRA Simulator module are subsequently processed by the LIRA Analysis module as if the dataset was obtained from an actual measurement.

The RG-58 coaxial cable was modeled in the LIRA simulator by entering the physical properties, which include the inner conductor diameter, outer shield diameter, insulation dielectric constant, and conductor metal types. The General Cable three-conductor shielded cable was approximated as a twisted pair using the distributed circuit parameters from the cable datasheet as well as LIRA measurements. The twisted pair was modeled using the conductor diameter, distributed inductance, distributed capacitance, insulation loss tangent, and conductor metal type. In all simulation cases, the cable orientation is assumed to be straight along the entire length of the cable and the temperature was specified as 20°C. Table 7.1 lists the cable parameters used in the the LIRA simulator models for the simulation study.

Table 7.1. Cable parameters considered in Wirescan LIRA FDR simulation models.

| Parameter | Twisted-Pair Cable | RG-58 Coaxial Cable |
|---|---|---|
| Conductor | Copper, 1.29 mm diameter | Copper, 0.91 mm diameter |
| Insulation | N/A | PE, Dk = 1.98, 1.02 mm thick |
| Shield | Copper | Copper |
| Jacket | N/A | N/A |
| Outer Diameter | N/A | 2.95 mm insulation diameter |
| Loss | Insulation Df = 0.0001–0.02 | N/A |
| Inductance | 0.3396 µH/m | N/A |
| Capacitance | 91.50 pF/m | N/A |

The LIRA simulator module can include the effects of stochastic and random noise on the simulated FDR response. A stochastic noise function can be enabled for each segment in the model to simulate the effects of cable construction tolerances. Fabrication tolerances produce small, repeatable fluctuations in the electrical parameters along a given cable. The stochastic noise level is entered as a standard deviation value with a default setting of 0.5%, and is strongly dependent on the anticipated characteristics of the cable. This stochastic noise setting was enabled in a “locked” state on the undamaged segments and disabled for the defect segment. Locking the stochastic noise models allows a direct comparison to be made for a given cable with and without a defect segment. A random white noise level is also available to simulate the noise produced by the electronics hardware and is entered as a percentage, with a default value of 0.5%. For all simulation cases, this noise source was disabled over the entire cable length to prevent undesired variations between simulation models.

# 8. VALIDATION OF SIMULATION RESULTS

The cable simulation tools were validated using measurements of damaged and undamaged cables obtained with a vector network analyzer (VNA) and a Wirescan LIRA system. These instruments have been evaluated under a previous report within this program and shown to provide similar results for bandwidths of 100 MHz (Glass et al. 2016b). Figure 8.1 shows the LIRA Acquire system and an example VNA, which has been used to measure cable FDR responses. The LIRA Acquire system has an upper frequency limit of 100 MHz while the VNA can be used to collect data over larger frequency ranges. The ANSYS simulation results were compared against the measured responses and the LIRA simulator for bandwidths of 100 MHz and 200 MHz.

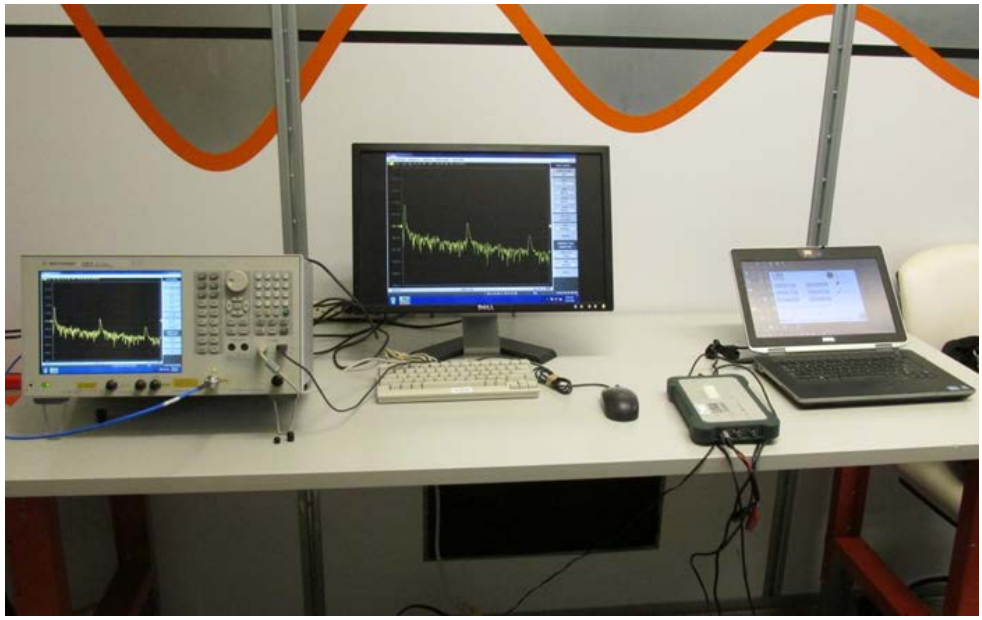

Figure 8.1. VNA FDR instrument (*left*) and LIRA FDR instrument (*right*).

A comparison between simulation and measurement was performed using a 100 ft. section of RG-58 coaxial cable with a 1.5 in. long gouge located at 50 ft. This defect consisted of removing the upper half of the PVC jacket, the outer shield, and the polyethylene insulation as shown in Figure 8.2. In the Nexxim circuit simulation, a randomized impedance tolerance with a standard deviation of 0.25% was applied to the undamaged segments to generate a noise floor representative of the cable fabrication tolerances. As shown in Figure 8.3 and Figure 8.4, the ANSYS simulation results and VNA measurements agree well for bandwidths of 200 MHz and 100 MHz, respectively.

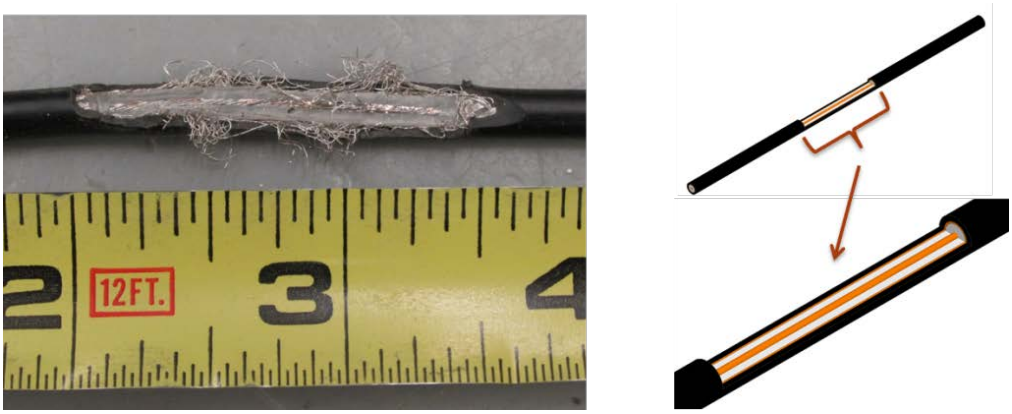


Figure 8.2. (*left*) RG-58 coaxial cable with 1.5 in. long mechanical damage; (*right*) corresponding ANSYS HFSS finite element model of damaged section.

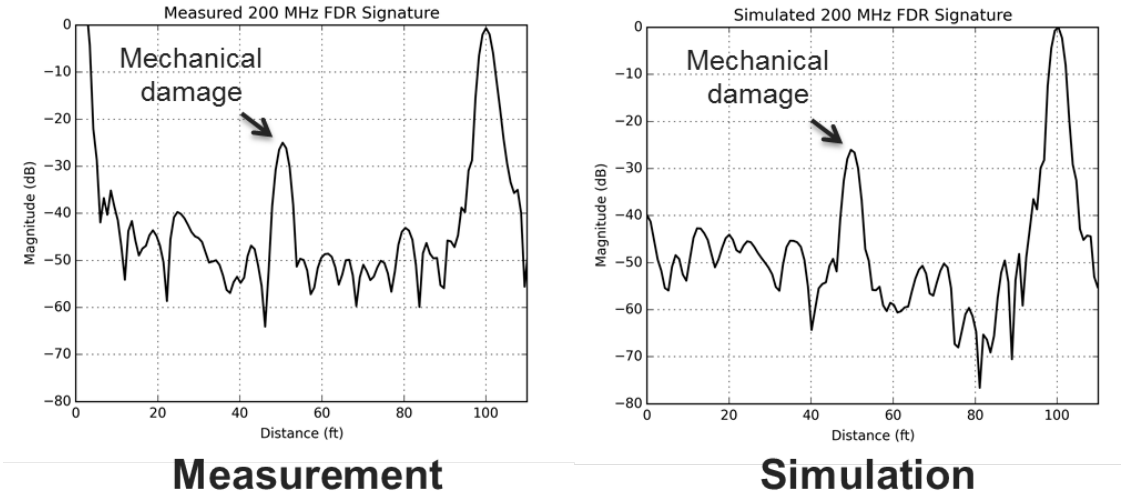


Figure 8.3. (*left*) 200 MHz VNA measurement and (*right*) 200 MHz ANSYS simulation of 1.5 in. long damaged section at the halfway point of a 100 ft. RG-58 coaxial cable.

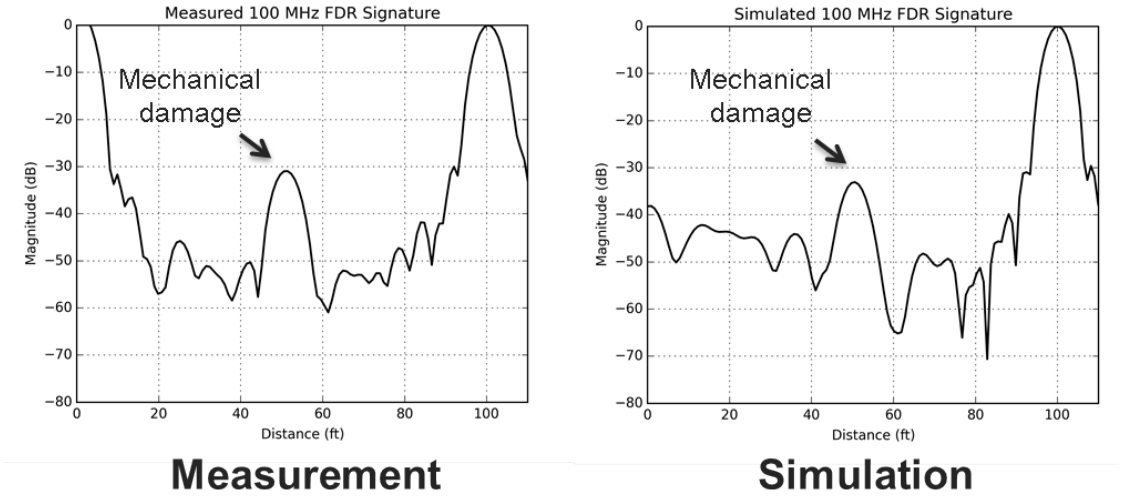


Figure 8.4. (*left*) 100 MHz VNA measurement and (*right*) 100 MHz ANSYS simulation of 1.5 in. long damaged section at the halfway point of a 100 ft. RG-58 coaxial cable.

Results from the LIRA simulator module were compared with the LIRA measurement of the RG-58 coaxial cable. The measured noise floor level was approximately represented in the LIRA model using a stochastic noise setting of 0.3%. Since the physical gouge cannot be directly modeled using this simulator, a defect peak having a similar amplitude was obtained by increasing the insulation dielectric constant by 30%. Figure 8-5 shows the results of the LIRA measurement and simulation. The large change required in the cable insulation dielectric constant for the simulation signal to be visible and approximately equal to the measured value is due to the short defect length of 0.125 ft. (3.8 cm) when compared to the resolution of the 100 MHz measurement, which is approximately 3.3ft (100 cm).

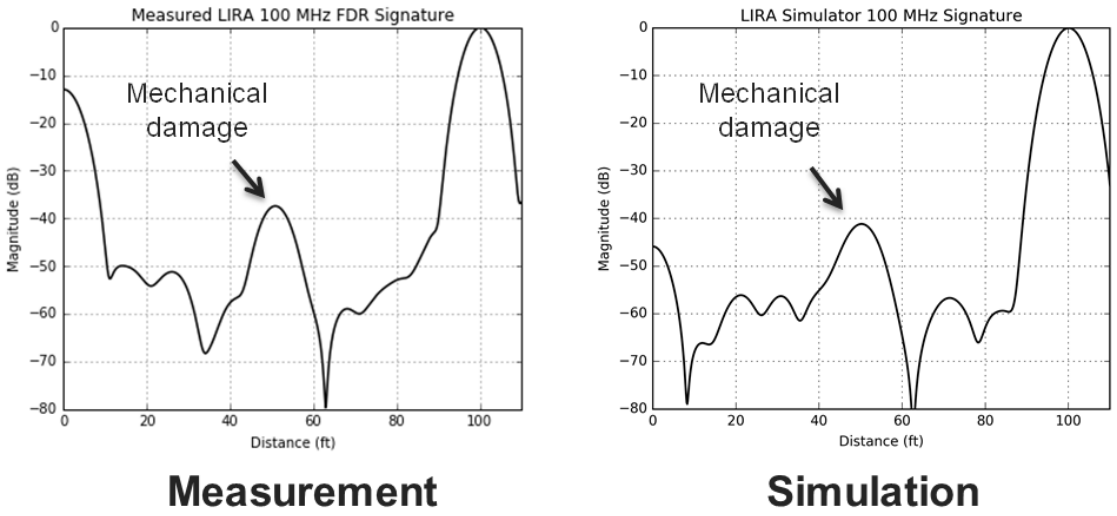


Figure 8.5 (*left*) 100 MHz LIRA measurement of 1.5 in. (3.8cm) long damaged section at halfway point of 100 ft. RG-58 coaxial cable and (*right*) corresponding 100 MHz LIRA simulation using 30% increase in insulation dielectric constant to match defect peak amplitude.

A similar comparison was performed using a 100 ft. section of General Cable FR-EPR/CPE shielded 600V three-conductor cable (General Cable 2016). In this case, a 3.5 in. long segment of the cable jacket and shield was removed at the 50 ft. location as shown in Figure 8.6. In the Nexxim circuit simulation, a randomized impedance tolerance with a standard deviation of 2% was applied to the undamaged segments to generate a noise floor representative of the cable fabrication tolerances. The ANSYS simulation results and VNA measurements for 200 MHz and 100 MHz are in good agreement as shown in Figure 8.7 and Figure 8.8, respectively.

Figure 8.6. (*left*) Damaged 3.5 in. section at the halfway point of a 100 ft. three-conductor shielded 600V EPR cable; (*right*) corresponding ANSYS HFSS finite element model of damaged section.

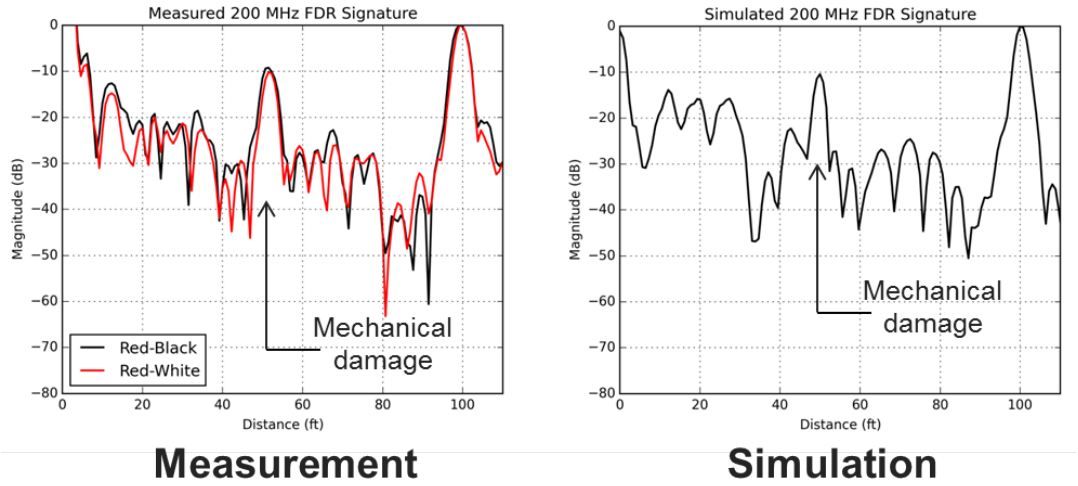


Figure 8.7. (*left*) 200 MHz VNA measurement and (*right*) 200 MHz ANSYS simulation of damaged 3.5 in. section in the center of 100 ft. three-conductor shielded EPR cable.

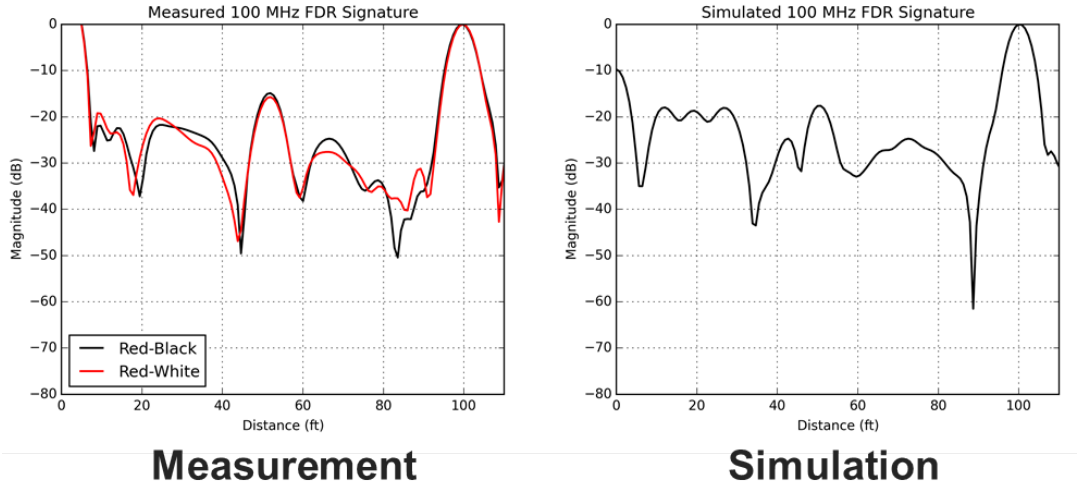


Figure 8.8. (*left*) 100 MHz VNA measurement and (*right*) 100 MHz ANSYS simulation of damaged 3.5 in. section in the center of 100 ft. three-conductor shielded EPR cable.

The three-conductor cable with the 3.5 in. long mechanical defect was simulated and measured with the LIRA Acquire system and LIRA simulator module. The cable capacitance of the damaged segment was increased by 5% and the stochastic cable noise level of 2.5% was specified to closely approximate the measured results. Figure 8.9 shows the results of the LIRA simulation and LIRA measurement. Although the peak corresponding to the defect location at 50 ft. is not as clear as in the ANSYS simulation, the highest peak is in the correct location and significantly above the baseline level.

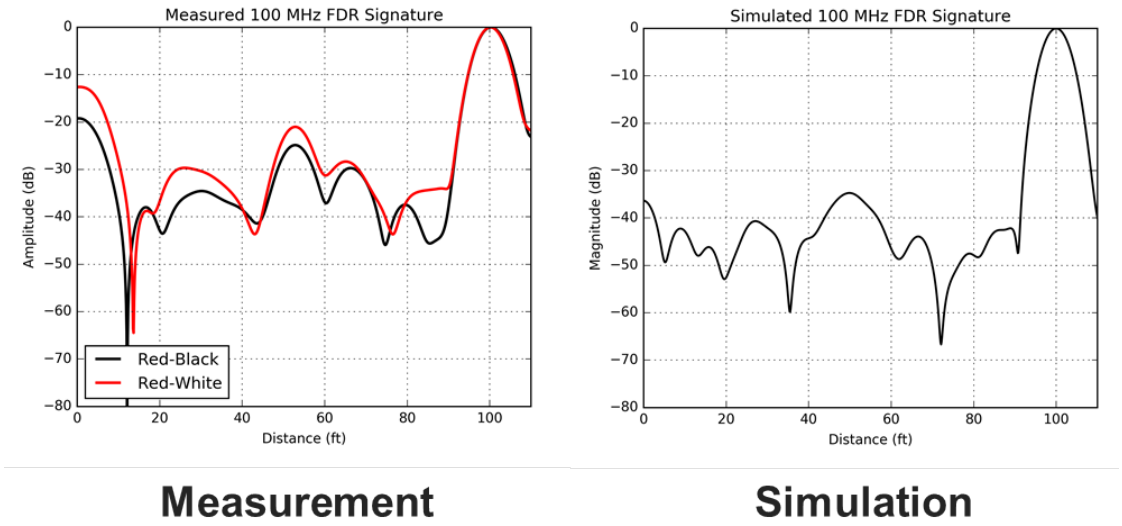


Figure 8.9. (*left*) 100 MHz LIRA measurement of 3.5 in. long damaged section at halfway point of 100 ft. three-conductor shielded EPR cable; (*right*) corresponding 100 MHz LIRA simulation using 5% increase in insulation dielectric constant to match defect peak amplitude.

# 9. TEST AND SIMULATION RESULTS

## 9.1 Degree of Cable Damage

Dielectric spectroscopy has been studied as a nondestructive technique to assess the aged state of cable insulation polymers. Dielectric properties are here compared with EAB, which is a mechanical indicator of polymer degradation.

Three-conductor multipolar cables insulated with EPR and covered by a PVC jacket, shown in Figure 9.1(a), were thermally aged at 140°C for up to 1,270 hr. Thermal aging of the samples, for eight different durations, was conducted at PNNL. The three different colors of EPR insulation should be noted, because the additives that give rise to the color difference also cause differences in the mechanical and electrical material properties measured in the ensuing characterization tests.

EAB measurements of the EPR insulation was performed according to IEC/IEEE 62582-3 (2011). Tubular samples were prepared from the cable by separating the PVC jacketing material from the insulated conductors and removing the conductor from the insulation. Samples were pulled to break using a Lloyd Instruments LF Plus test stand at PNNL and EAB was calculated using grip displacement

Capacitance (C) and dissipation factor (Tan δ) were measured using a Novocontrol Alpha-A dielectric analyzer at Iowa State University over the frequency range from 0.01 Hz to 1 MHz, at ambient temperature and humidity.

Prior to measurement, a custom connector was designed to connect the three-core cable to the analyzer. Simulations were conducted using COMSOL Multiphysics® to identify the best configuration of applied voltage (high potential and low potential) so that capacitance measured on the intact cable would be maximally sensitive to the EPR insulation properties. Out of various configurations considered, the best configuration turned out to be one in which a single conductor is held at high potential, the other two conductors are held at low potential (ground), and a temporary shield applied to the cable exterior is also held at low potential. A custom connector, Figure 9.1(b), and sheath arrangement, Figure 9.1(c), were developed to effect this voltage configuration and ensure a high level of measurement repeatability.

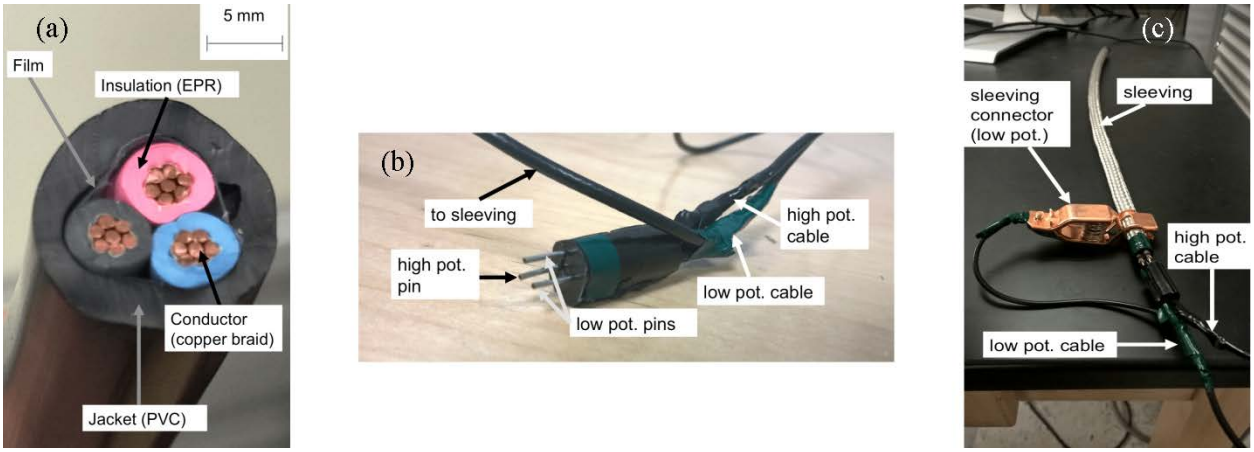


Figure 9.1. (a) Cross-section view of Okonite-FMR Okoseal cable; (b) in-house connector head that connects to the sample conductors; (c) connector attached to the sample, with temporary, grounded shield applied to the sample exterior.

C and Tan δ were measured over the frequency range from 0.01 Hz to 1 MHz using the custom connector and voltage configuration described above. They were generally observed to increase with sample aging time, with some departures from this general trend at certain frequencies. Example results are presented in Figure 9.2 and Figure 9.3. The full dataset is available in Imperatore (2017).

At 0.1 Hz (Figure 9.2) C exhibits a large, step-like, increase at shorter aging times (~700 hr.) than the observed change in EAB (~1,100 hr.). At the same frequency, Tan δ also exhibits a large increase at around 700 hr., but then declines as aging time continues to increase, making Tan δ less suitable than C as an indicator of aging at this frequency. At 1 kHz, both C and Tan δ begin to increase at shorter aging times (~600 hr.) than the observed change in EAB (~1,100 hr.), as shown in Figure 9.3 (apart from C for pink EPR, which initially declines).

In conclusion, C and Tan δ measured on intact cables are promising, nondestructive, diagnostic indicators of EPR insulation aging. The measurement approach is versatile and adaptable to other cable configurations.

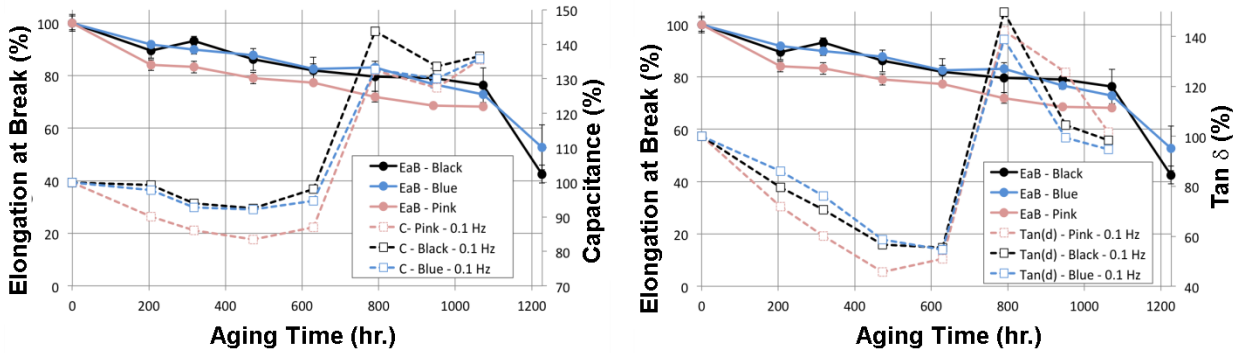


Figure 9.2. Comparison between EAB and specific capacitance C (*left*), and between EAB and Tan δ (*right*), at 0.1 Hz. The color indicates the color of the wire held at positive potential during the measurement.

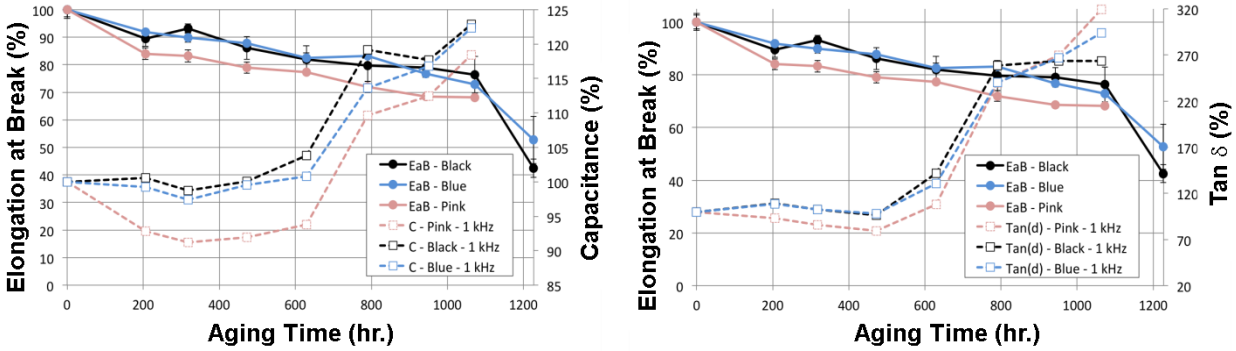


Figure 9.3. Same as for Figure 9.2 but at 1 kHz.

To assess the influence of a uniform change in cable insulation dielectric constant (which is related to the distributed capacitance), simulations were performed using both the ANSYS and LIRA simulation tools for the coaxial cable and the shielded triad cable. In each case, the insulation dielectric constant of a 1 ft. section centered along the 100 ft. cable was increased from the nominal value by 1% to 5% in 1% increments. For the three-conductor shielded cable, these changes along a 3 ft. section of cable were also simulated. The influence of dielectric constant changes on the calculated characteristic impedance of the three-conductor cable impedance segment is summarized in Table 9.1. These changes are significantly below the >30% change in capacitance associated with a 50% EAB shown in Figure 9.2 and Figure 9.3.

Table 9.1. Influence of cable insulation dielectric constant changes on characteristic impedance of shielded three-conductor cable segment.

| Case | $Z_0$ @ 100 MHz (Ω) | % Difference in $Z_0$ |
|---|---|---|
| Baseline: EPR Dielectric Constant (Dk) = 3.0 | 62.67 | 0 |
| 1% increase in Dk | 62.44 | −0.37 |
| 2% increase in Dk | 62.22 | −0.72 |
| 3% increase in Dk | 62.00 | −1.07 |
| 4% increase in Dk | 61.79 | −1.41 |
| 5% increase in Dk | 61.58 | −1.74 |

The ANSYS simulation results for 100 MHz and 200 MHz bandwidths are shown in Figure 9.4 for the 100 ft. coaxial cable models. A stochastic noise setting of 0.25% was used in the simulations to produce a noise level similar to the measurements. Note that a 1% change produces an 8–10 decibels (dB) response in the FDR peak when compared to the baseline reference, and increasing from 1% to 5% produces an additional 10–15 dB change in the defect peak amplitude.

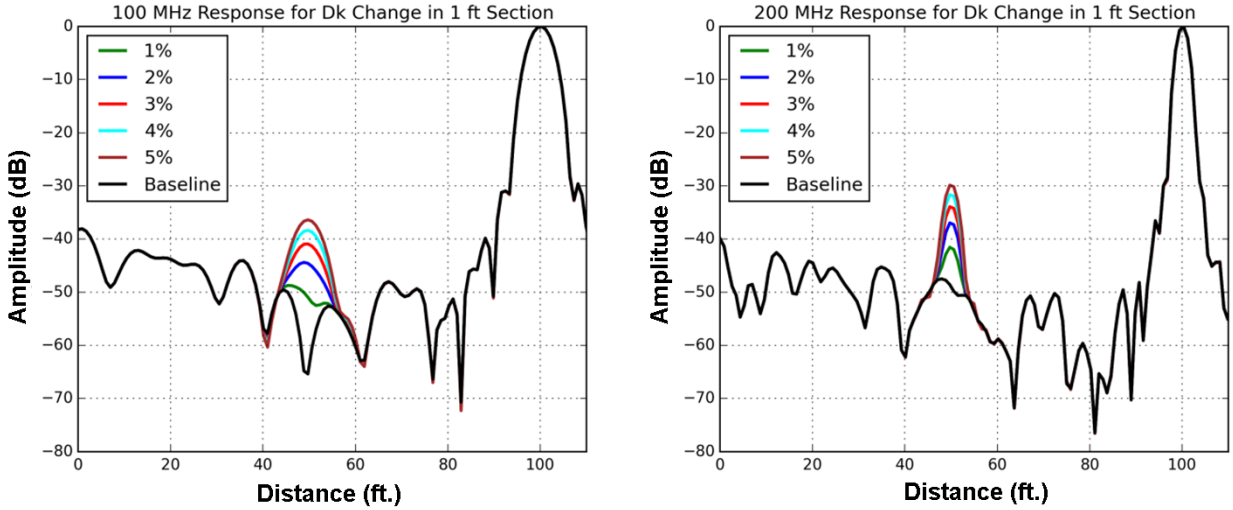


Figure 9.4. (*left*) 100 MHz and (*right*) 200 MHz ANSYS simulations for insulation dielectric constant changes in a 1 ft. segment at the halfway point of 100 ft. coaxial cable.

The ANSYS simulation results for 100 MHz and 200 MHz bandwidths are shown in Figure 9.5 for the 100 ft. shielded triad cable models. No stochastic noise was added in these simulations so that the smallest reflections would be visible. These noiseless simulated responses are not associated with a specific dynamic range or cable fabrication tolerance, which will limit detection in an actual measurement. The defect peak amplitudes are higher for an FDR bandwidth of 200 MHz, but may still fall below the noise level for confident detection if the noise level is comparable to these peaks. For example, Figure 8.7 shows the measured noise level for this specific cable was as high as −30 dB relative to the end termination peak.

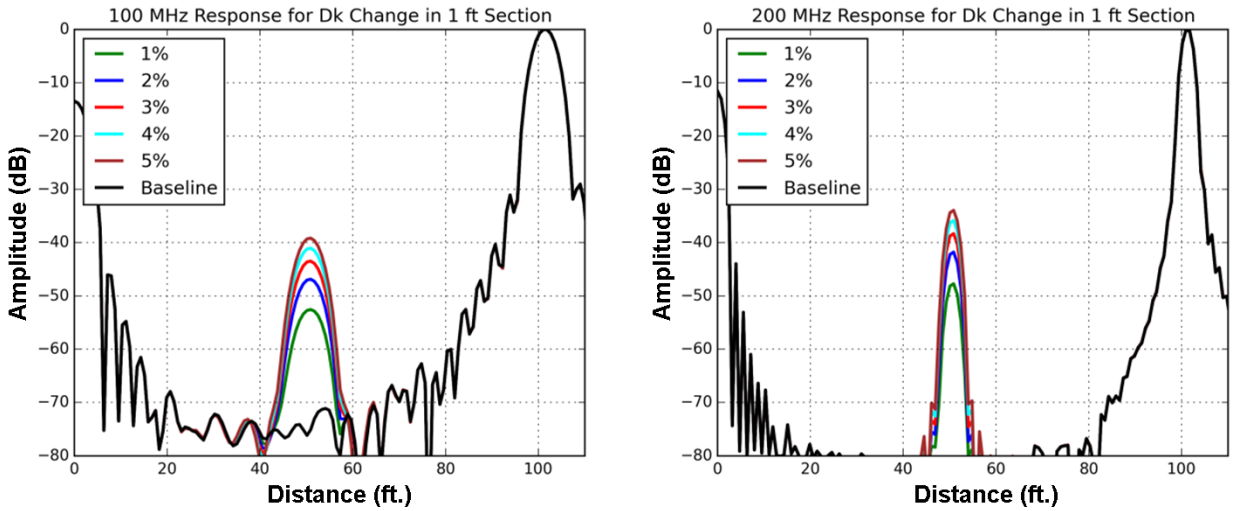


Figure 9.5. (*left*) 100 MHz and (*right*) 200 MHz ANSYS simulations for insulation dielectric constant changes in a 1 ft. segment at the halfway point of 100 ft. shielded triad cable.

The 100 MHz LIRA simulation results are shown in Figure 9.6 for the 100 ft. coaxial cable and shielded triad cable. Stochastic noise settings of 0.3% and 2.5% were used in the simulations to represent noise floor levels similar to measurements of the coaxial and shielded triad cables, respectively. Using the available input parameters in the simulation, the segment insulation dielectric constant was increased in the coaxial cable model while the segment capacitance was increased in the twisted-pair model representing the shielded triad cable. The results for both cables are qualitatively similar to the ANSYS simulations, with the lower noise level in the coaxial cable allowing for improved detection. The noise level in the shielded triad cable simulated response could make detection of changes below 4% difficult unless a baseline dataset was available for comparison.

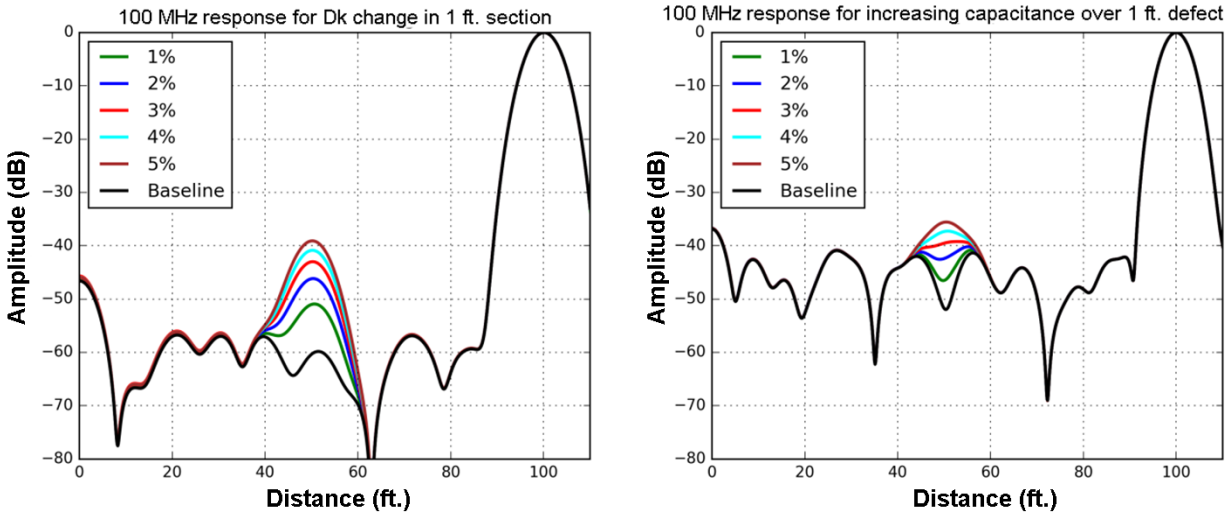


Figure 9.6. 100 MHz LIRA simulations for (*left*) insulation dielectric constant changes in a 1 ft. segment at the halfway point of 100 ft. coaxial cable and (*right*) capacitance changes in a 1 ft. segment at the halfway point of 100 ft. shielded triad cable.

## 9.2 Defect Length

To evaluate the influence of defect length on the FDR response, ANSYS models were created for a range of defect lengths centered along a 100 ft. shielded triad cable. Each defect section was represented by a uniform 5% change in insulation dielectric constant. The FDR responses were divided into relatively short damage lengths of less than 1 wavelength and relatively long damage lengths of greater than or equal to 1 wavelength at the highest frequency. The electrical wavelength for the triad cable at 100 MHz and 200 MHz is approximately 6 ft. and 3 ft. respectively

The simulation results for the two groups are shown in Figure 9.7 through Figure 9.10. Figure 9.7 and Figure 9.8 show the results for a 200 MHz bandwidth, and Figure 9.9 and Figure 9.10 show results for a 100 MHz bandwidth. No stochastic noise representing the effects of fabrication tolerances was added in the circuit simulation because the goal was to study the effect of the defect segment length, and stochastic noise could conceal the responses of short defects.

For the relatively short defects, the reflection peak increased in amplitude as the defect length approached approximately 0.5 wavelengths long. This length is equivalent to the spatial resolution of the FDR spectrum. In the 200 MHz simulations, the difference in the peak amplitudes for 0.25 ft. and 1 ft. defect lengths was approximately 10 dB.

For the longer defects, two distinct peaks were present in the FDR response at the beginning and end of the defect segment. This is due to the defect length being greater than the spatial resolution of approximately 1.5 ft. for 200 MHz bandwidth and approximately 3 ft. for 100 MHz bandwidth. The amplitudes of these peaks were approximately 3 dB lower than the maximum single peak since the energy was divided into two reflections.

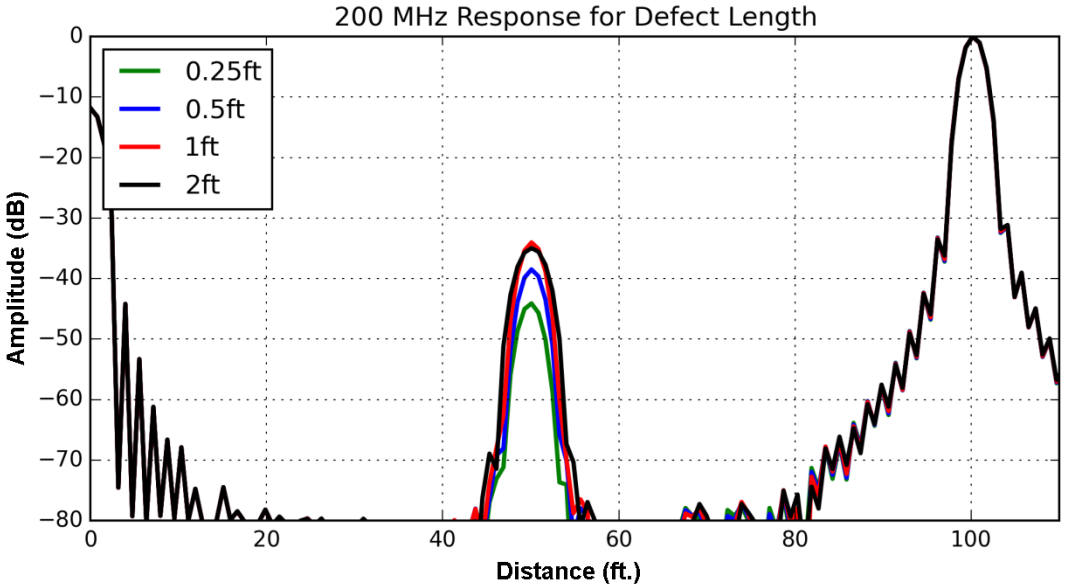


Figure 9.7. 200 MHz ANSYS simulation of 5% increase in insulation dielectric constant for relatively short defect lengths (<1 wavelength at maximum frequency) in three-conductor shielded cable.

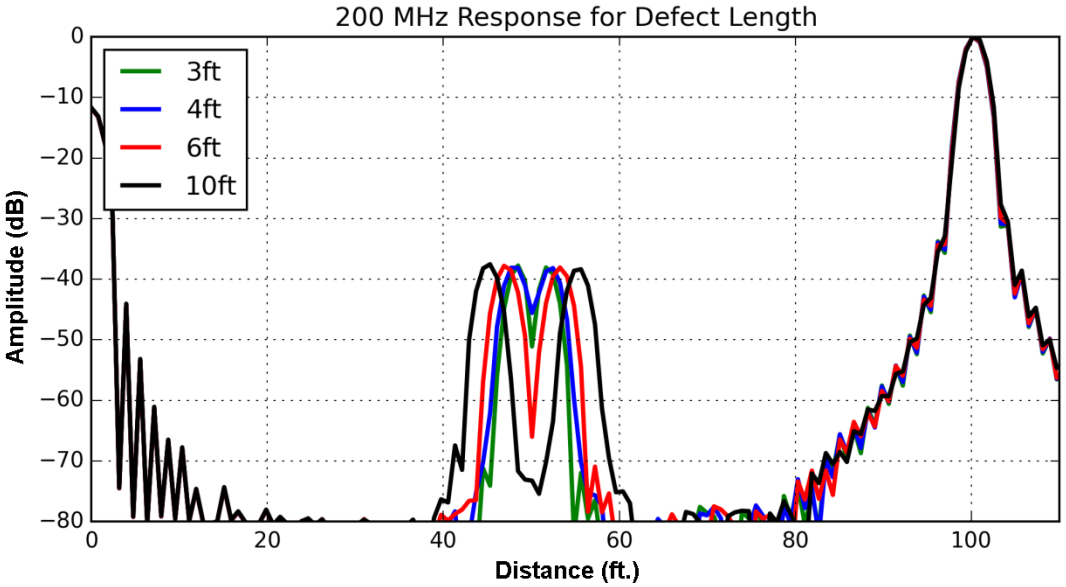


Figure 9.8. 200 MHz ANSYS simulation of 5% increase in insulation dielectric constant for relatively long defect lengths (≥1 wavelength at maximum frequency) in three-conductor shielded cable.

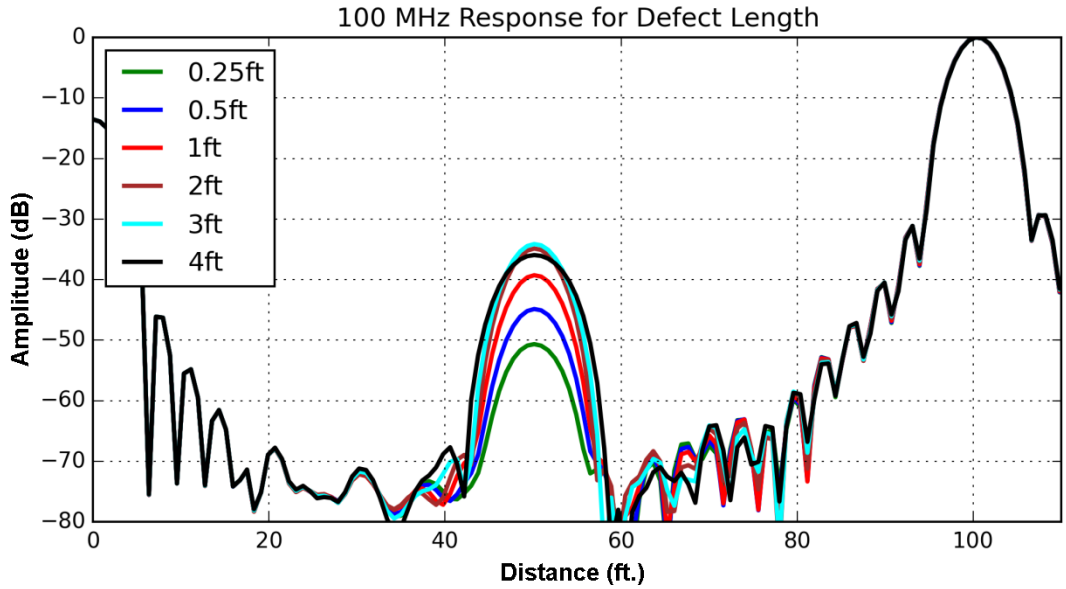


Figure 9.9. 100 MHz ANSYS simulation of 5% increase in insulation dielectric constant for relatively short defect lengths (<1 wavelength at maximum frequency) in three-conductor shielded cable.

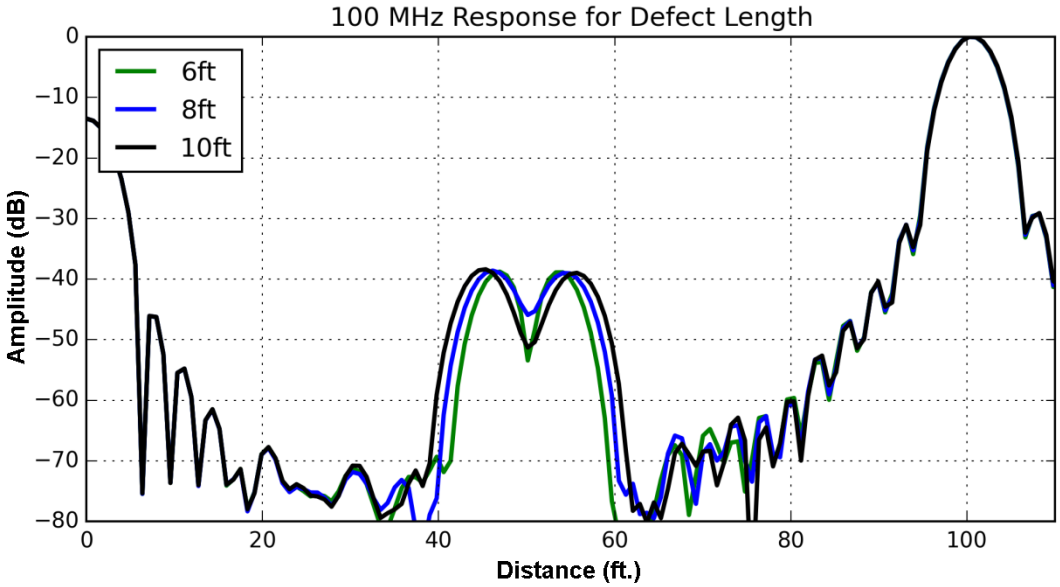


Figure 9.10. 100 MHz ANSYS simulation ofF 5% increase in insulation dielectric constant for relatively long defect lengths (≥1 wavelength at maximum frequency) in three-conductor shielded cable

To illustrate how cable fabrication tolerances can produce noise levels that affect detection as a function of defect length, the LIRA simulator was used to model coaxial and twisted-pair cables. For the coaxial cable, the defect segment was modeled as a 3% increase in the insulation dielectric constant and the stochastic noise setting was specified as 0.3%. For the twisted-pair model, the defect segment was modeled as a 3% increase in the local capacitance and the stochastic noise setting was specified as 2.5%. These values yielded noise levels representative of laboratory measurements. The results are shown in Figure 9.11.

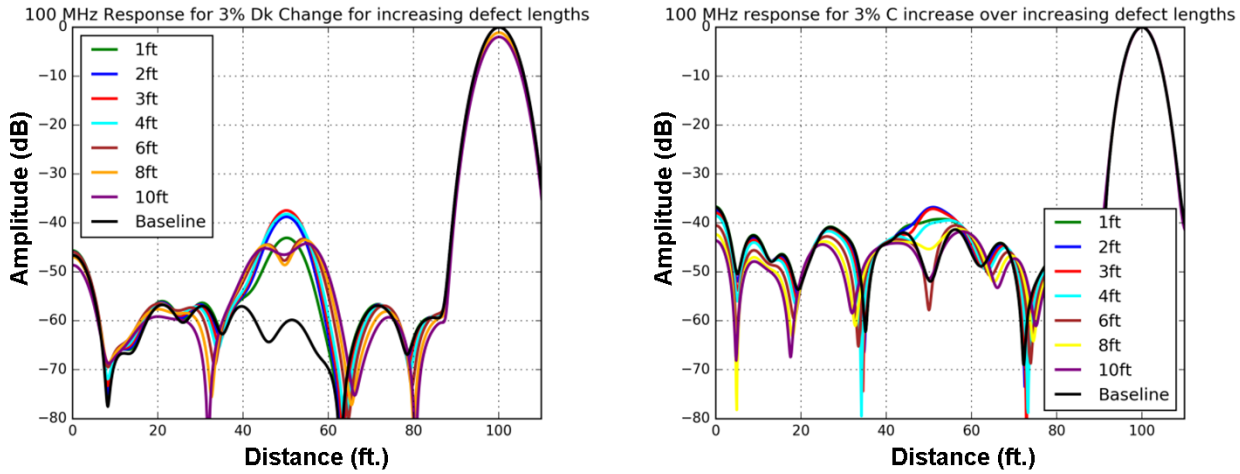


Figure 9.11. 100 MHz LIRA simulation of (*left*) 3% increase in insulation dielectric constant for defect lengths centered along 100 ft. coaxial cable with 0.3% stochastic noise and (*right*) 3% increase in local capacitance for defect lengths centered along 100 ft. twisted-pair cable with 2.5% stochastic noise.

The LIRA simulations that include stochastic noise show the same trend with increasing defect length. The peak amplitude increases for lengths up to 3 ft. and then decrease as the peak separates into peaks at the beginning and end of the defect segment. All defect responses are significantly above the noise level for the coaxial cable, but only a few are noticeable for the twisted-pair cable.

To validate these simulations, three shielded triad cable sections of different lengths were aged in an oven at 140°C. The cable insulation material was EPR and the jacket material was CPE. The total length of each cable was approximately 100 ft. with 1.5 ft., 7.25 ft., and 10.5 ft. aged segments placed inside the oven. The aged sections were located at the halfway point of each cable. The accelerated aging oven setup is shown in Figure 9.12. Note that the 7.25 ft. and 10.5 ft. aged sections were vertically coiled to fit inside the oven.

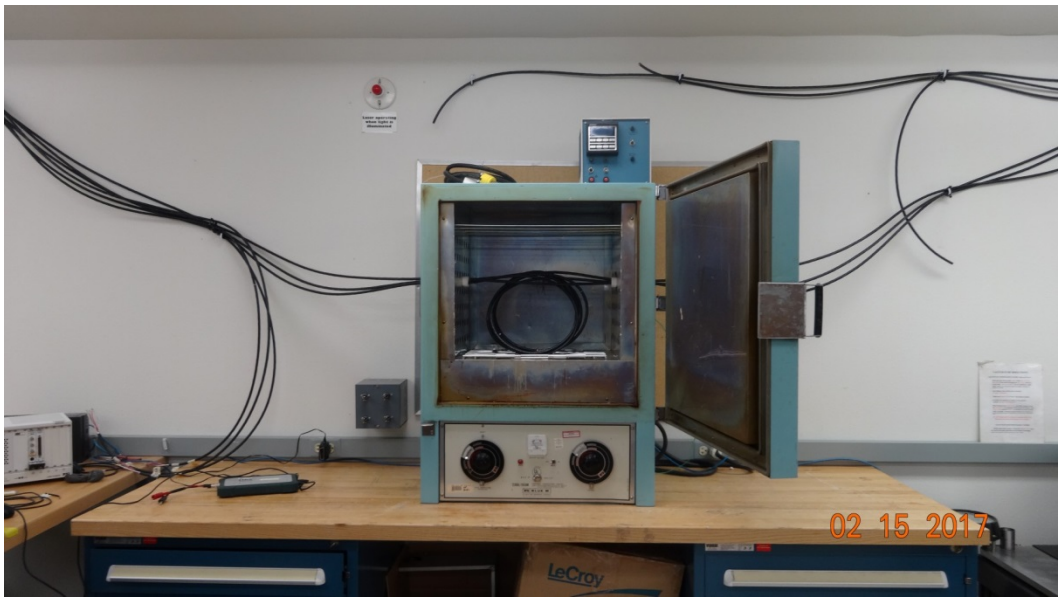


Figure 9.12. Accelerated aging experimental setup for heating 1.5 ft., 7.25 ft., and 10.5 ft. sections of three 100 ft. shielded three-conductor cables.

FDR measurements were made with the LIRA Acquire and VNA instruments after 1,638 hours of accelerated aging time to compare to the simulated responses of uniformly degraded sections having different lengths. The simulation models represent ideal scenarios in which the degraded section is in fact uniformly degraded, while the actual thermal degradation profile may be affected by the coiled state of the cables and any significant localized damage that occurs along the aged segments.

The LIRA measurements were performed in-situ with the cables undisturbed between the baseline and aged datasets. The cables were cooled to room temperature for each FDR measurement. Due to instrument availability, the aged cable VNA measurements were performed in a separate facility after the cables were carefully removed from the oven and placed in a nominally straight configuration.
Figure 9.13 shows the aged sections of the test cable configuration for the in-situ LIRA and ex-situ VNA measurements. Due to the degraded condition of the cable jackets, it was not possible to uncoil the 7.25 ft. and 10.5 ft. sections for the aged measurements.

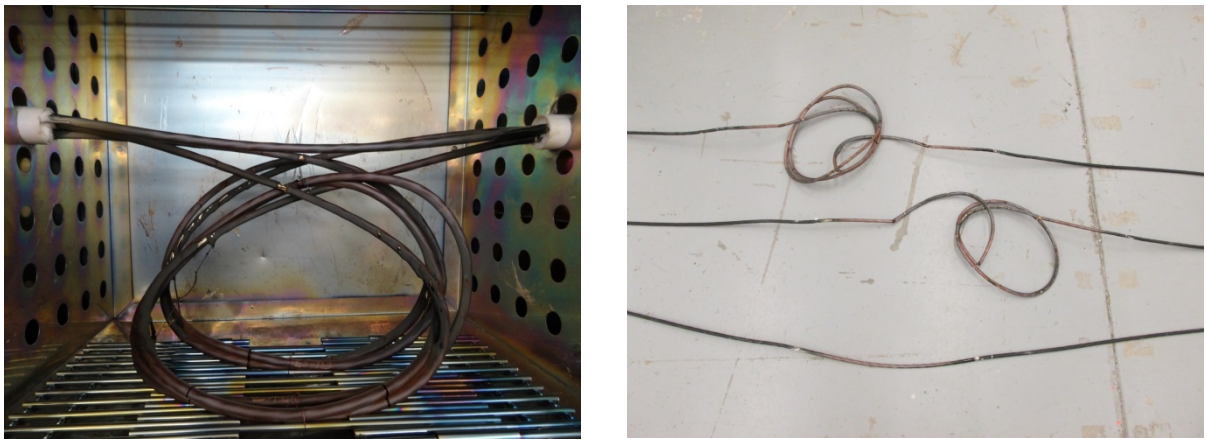

Figure 9.13. Aged cable configurations for (*left*) in-situ LIRA measurements and (*right*) ex-situ VNA measurements.

Figure 9.14 shows LIRA measurements for an example conductor pair of the cables with 1.5 ft. and 7.25 ft. aged sections. The 1.5 ft. aged segment appears as a single peak at 50 ft. approximately 15 dB above the baseline measurement response at this location. The 7.25 ft. aged segment appears as two separate peaks at the beginning and end of the defect section centered at 50 ft. These measured responses are consistent with the characteristics of the simulated responses for defect lengths smaller and larger than the spatial resolution. The LIRA data from the 10.5 ft. aged section is not shown since it did not exhibit a noticeable increase at the defect location compared to the baseline measurement.

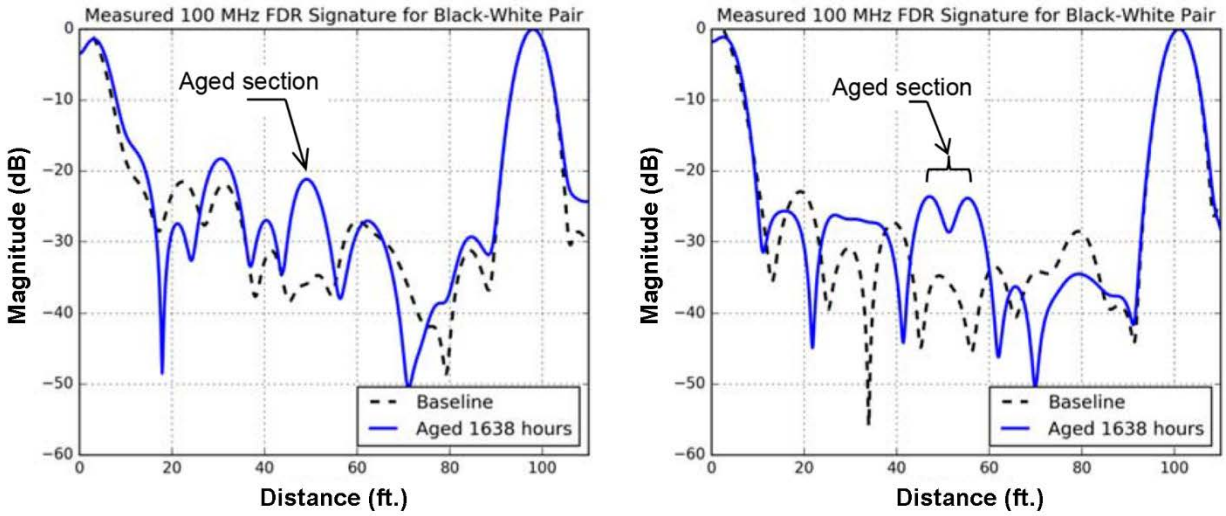


Figure 9.14. 100 MHz LIRA measurements for a uniformly aged (*left*) 1.5 ft. and (*right*) 7.25 ft. segment at the halfway point of 100 ft. shielded triad cable.

Figure 9.15 shows VNA measurements for an example conductor pair of the 7.25 ft. aged section using a highest frequency of 100 MHz and 200 MHz. For both cases, the defect response appears as separate peaks at the beginning and end of the segment centered around 50 ft. The amplitudes of the defect responses are 7–15 dB above the baseline measurement response at this location. The measured responses are consistent with the simulated responses for degraded sections, which are longer than the FDR spatial resolution. Asymmetry in the peak responses may be due to uncertainty in the final aged condition, which could have deviations from a uniform degradation profile.

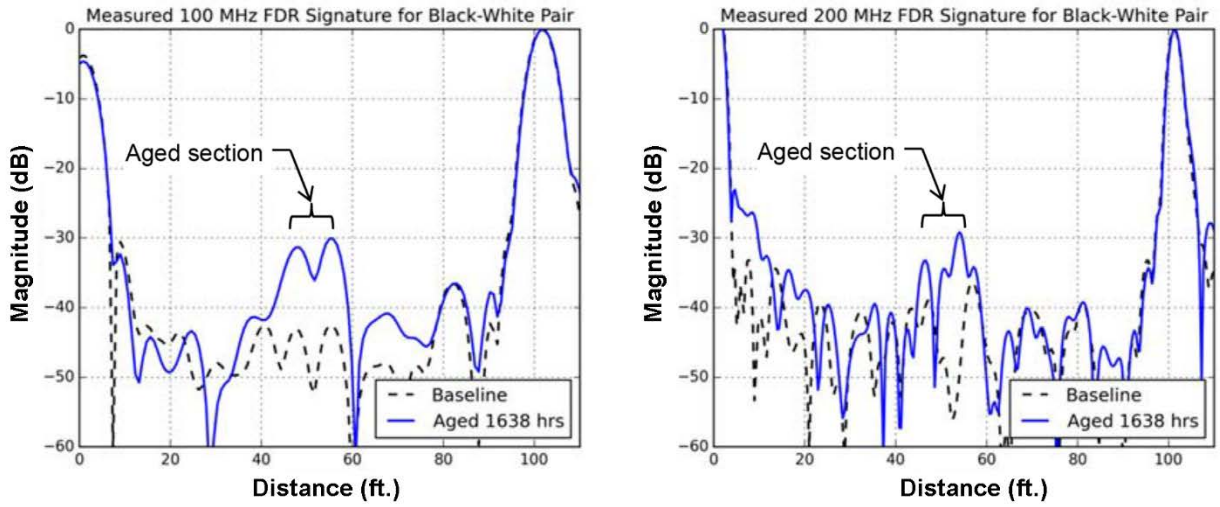


Figure 9.15. (*left*) 100 MHz and (*right*) 200 MHz VNA measurements for a uniformly aged 7.25 ft. segment at the halfway point of 100 ft. shielded triad cable.

Figure 9.16 shows VNA measurements for an example conductor pair of the 1.5 ft. aged section using a highest frequency of 100 MHz and 200 MHz. For both cases, the aged segment appears as a single peak at 50 ft., approximately 10 dB above the baseline measurement response at this location. The measured responses are consistent with the simulated responses for degraded sections, which are shorter than the FDR spatial resolution.

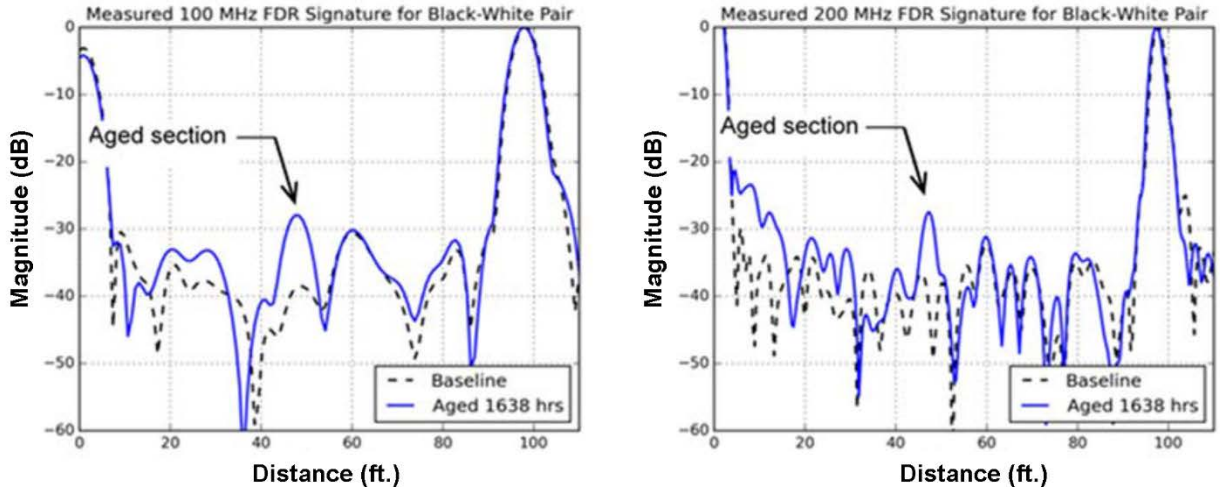


Figure 9.16. (*left*) 100 MHz and (*right*) 200 MHz VNA measurements for a uniformly aged 1.5 ft. segment at the halfway point of 100 ft. shielded triad cable.

Figure 9.17 shows the VNA measurements for an example conductor pair of the 10.5 ft. aged section using a highest frequency of 100 MHz and 200 MHz. For both cases, the aged segment appears as separate peaks at the beginning and end of the segement centered about 50 ft. and are above the baseline measurement response at this location. Again, these responses are consistent with the simulation results for degraded sections, which are longer than the FDR spatial resolution. Asymmetry in the measured defect peaks may be due to uncertainty in the final aged condition, which could have deviations from a uniform degradation profile.

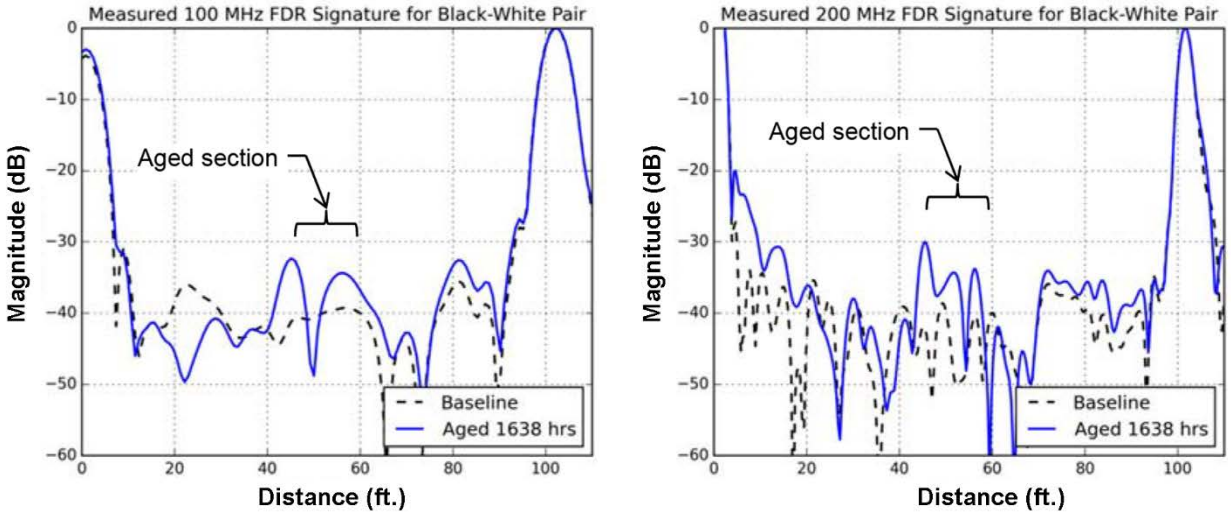


Figure 9.17. (*left*) 100 MHz and (*right*) 200 MHz VNA measurements for a uniformly aged 10.5 ft. segment at the halfway point of 100 ft. shielded triad cable.

The significance of these observations is that the length of an assumed uniform cable degradation should be considered during a peak amplitude calibration of FDR tests for assessing the degree of cable damage. Particularly short defects will produce lower amplitude responses than defects that are on the order of a half-wavelength at the highest frequency of the FDR system. Longer uniformly degraded defects can produce separate peaks, depending upon the frequency bandwidth.

## 9.3 Defect Distribution

The previous section noted the influence of defect length on the FDR response. It was observed that longer defects with abrupt changes in insulation dielectric constant (which is related to capacitance) produced significant responses at the beginning and end of the damaged area. These responses are due to the impedance discontinuities at these junctions. In order to investigate defect scenarios in which the change in cable electrical characteristics is of a more gradual nature, tapered increases in the insulation dielectric constant along a defect were compared to the uniform step changes. All of these cases were performed for a 100 ft. long three-conductor shielded cable in the ANSYS simulations and for a 100 ft. long twisted-pair cable in the LIRA simulations. No stochastic noise representing the effects of cable fabrication tolerances was added in the ANSYS circuit simulation.

An ANSYS model was created with a 10 ft. long defect consisting of a symmetrically tapered change in the insulation dielectric constant as shown in Figure 9.18. Simulation results are given in Figure 9.19 for this distribution. The peak change of 5% occurred in the center of the 10 ft. defect section. The results show that a symmetrically tapered defect distribution significantly lowered the peak response. Specifically, the peak amplitude was reduced by ~7 dB for the 100 MHz simulation and ~15 dB for the 200 MHz simulation.

The reduced peak responses result from the gradual change in impedance along the cable as the electromagnetic wave smoothly transitions between the undamaged and damaged segments. The two distinct peaks visible in the FDR response for the uniform defect are separated by approximately three wavelengths along the cable for the 200 MHz simulation. Additionally, the peaks at the beginning and end of the defect section were not as pronounced as in the uniform distribution.

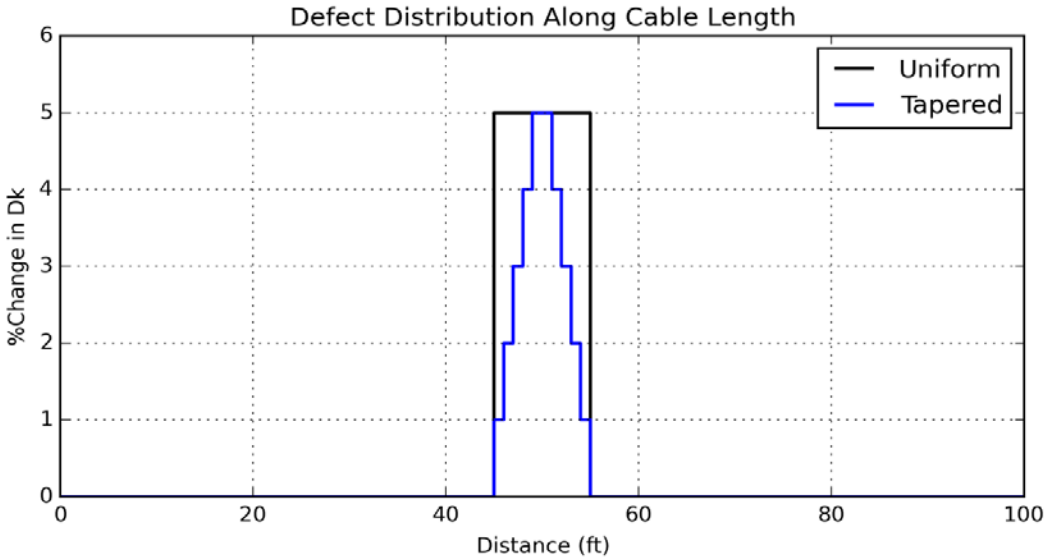


Figure 9.18. Increase in insulation dielectric constant for uniform and symmetrically tapered cable damage for 10 ft. defect section.

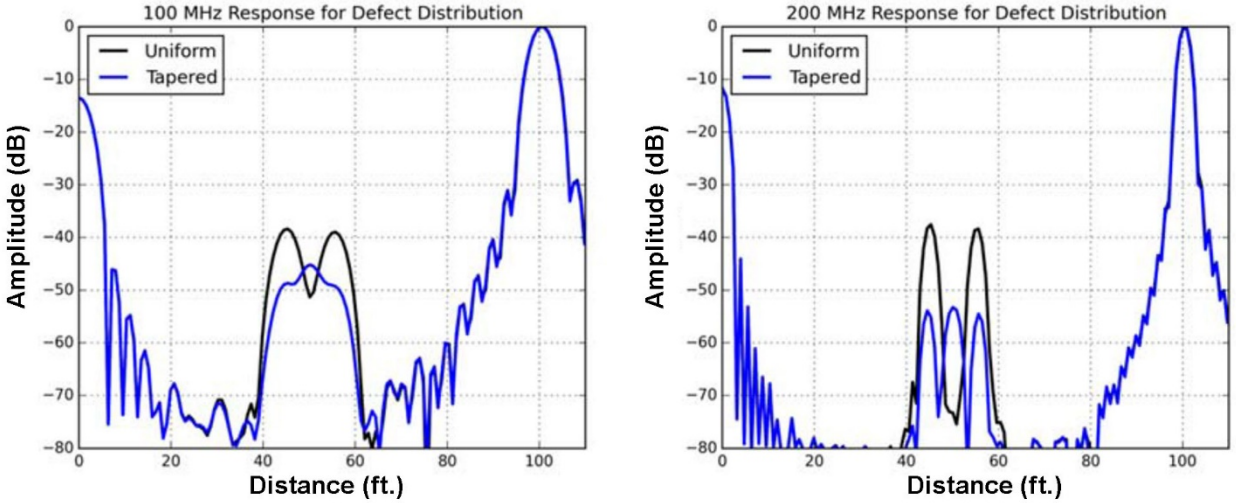


Figure 9.19. (*left*) 100 MHz and (*right*) 200 MHz ANSYS simulations for uniform and symmetrically tapered 10 ft. defect sections of 100 ft. three-conductor shielded cable.

Results from ANSYS simulations for a 10 ft. long defect consisting of a single-sided tapered change in the insulation dielectric constant are shown in Figure 9.20 and Figure 9.21. In this distribution, the peak change of 5% occurred at the far end of the 10 ft. defect section. The results show that the single-sided tapered defect distribution significantly reduces the reflection from the start of the defect section by over 10 dB, but preserves the reflection from the end of the defect section. This is due to the impedance change that occurs at this junction as the wave abruptly transitions back to the undamaged section.

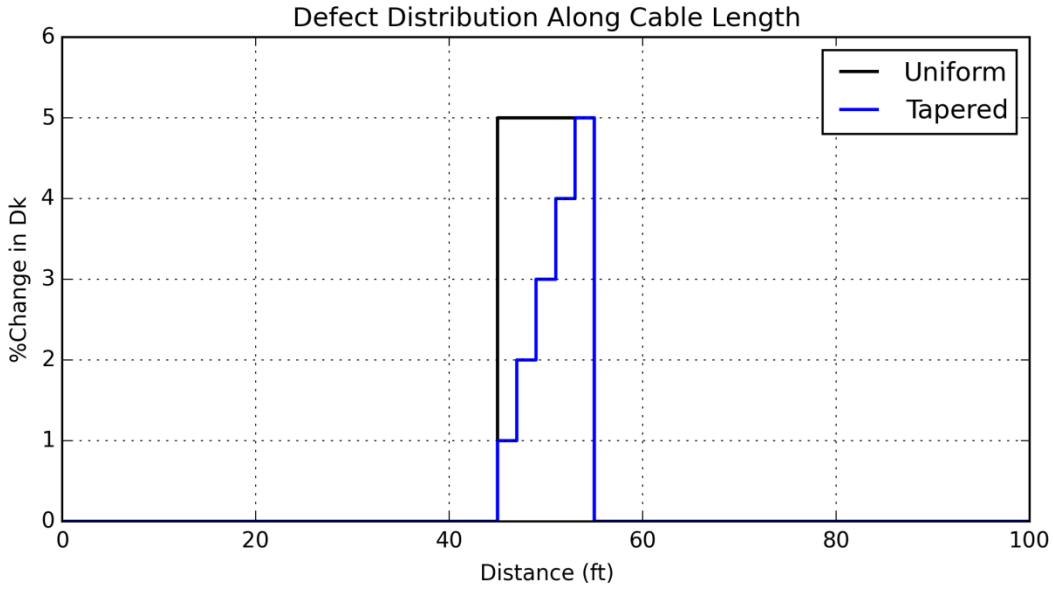


Figure 9.20. Increase in insulation dielectric constant for uniform and single-sided tapered cable damage cases for 10 ft. defect section.

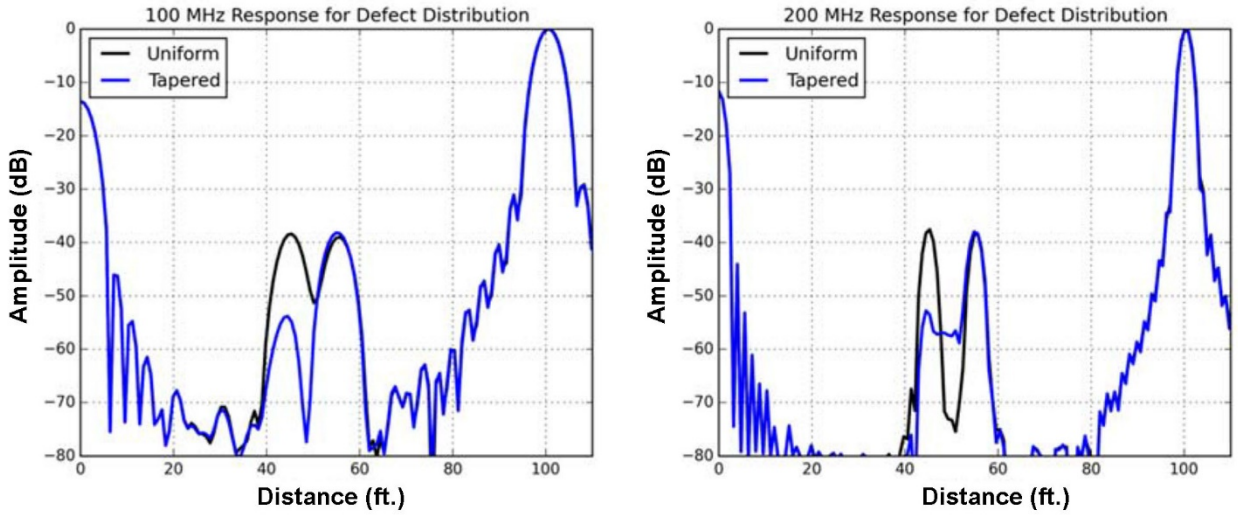


Figure 9.21. (*left*) 100 MHz and (*right*) 200 MHz ANSYS simulations for uniform and single-sided tapered 10 ft. defect sections of 100 ft. three-conductor shielded cable.

Additional tapered distribution models were created to determine the effects on the FDR response when the length is shorter than the resolution. Figure 9.22 shows a 2.5 ft. long defect consisting of a symmetrically tapered change in the insulation dielectric constant, with the peak change of 5% in the center of the defect section. The results in Figure 9.23 show that the symmetrically tapered defect distribution slightly lowered the peak response for the 100 MHz simulation. The response for the single peak was slightly higher than the two separated peaks for the 200 MHz simulation. This is consistent with the results in Section 9.2 in which the effect of the defect length was studied.

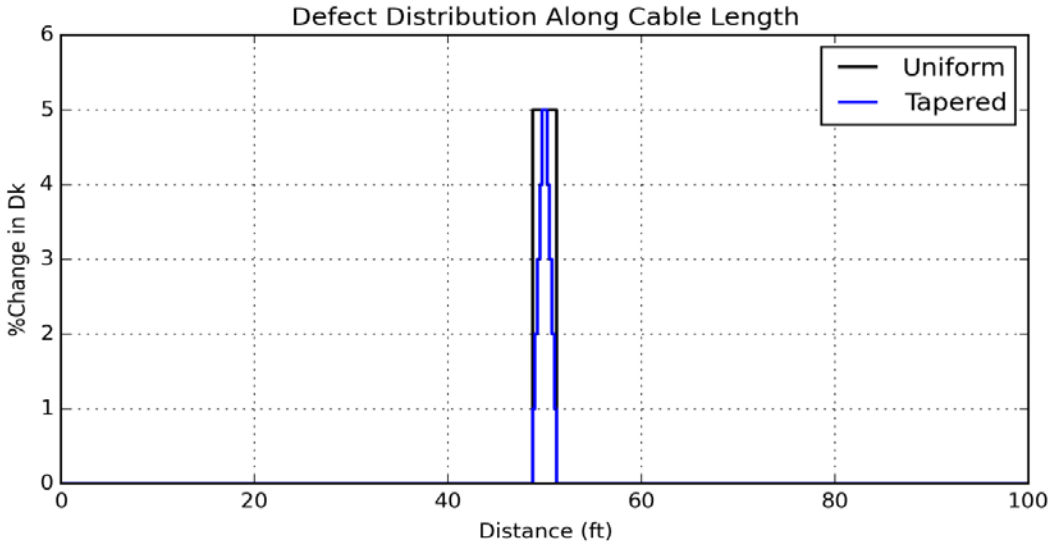


Figure 9.22. Increase in insulation dielectric constant for uniform and symmetrically tapered cable damage cases for 2.5 ft. defect section.

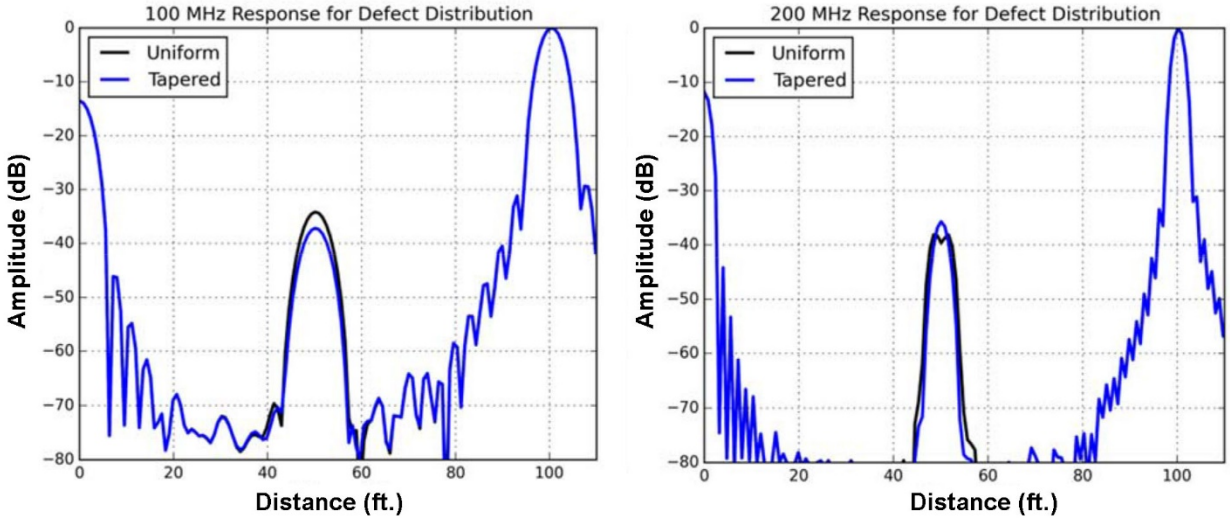


Figure 9.23. (*left*) 100 MHz and (*right*) 200 MHz ANSYS simulations for uniform and symmetrically tapered 2.5 ft. defect sections of 100 ft. three-conductor shielded cable.

Results from ANSYS simulations for a 2.5 ft. long defect consisting of a single-sided tapered change in the insulation dielectric constant are shown in Figure 9.24 and Figure 9.25. The peak change of 5% occurred at the end of the 2.5 ft. defect section. The single-sided tapered defect distribution reduces the reflection for the 100 MHz bandwidth case by ~4 dB and shifts the peak location accordingly. For the 200 MHz bandwidth case, the tapered defect slightly increases the peak amplitude with a more noticeable shift towards the end of the defect section. These cases serve to highlight some of the resolution improvements that are obtained from the use of wider bandwidths.

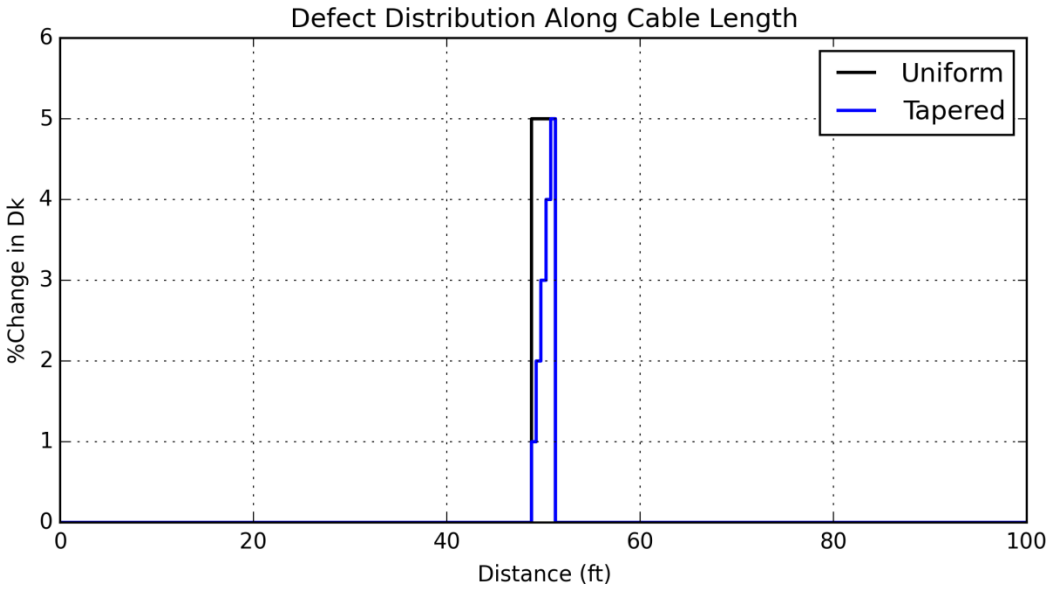


Figure 9.24. Increase in insulation dielectric constant for uniform and single-sided tapered cable damage cases for 2.5 ft. defect section.

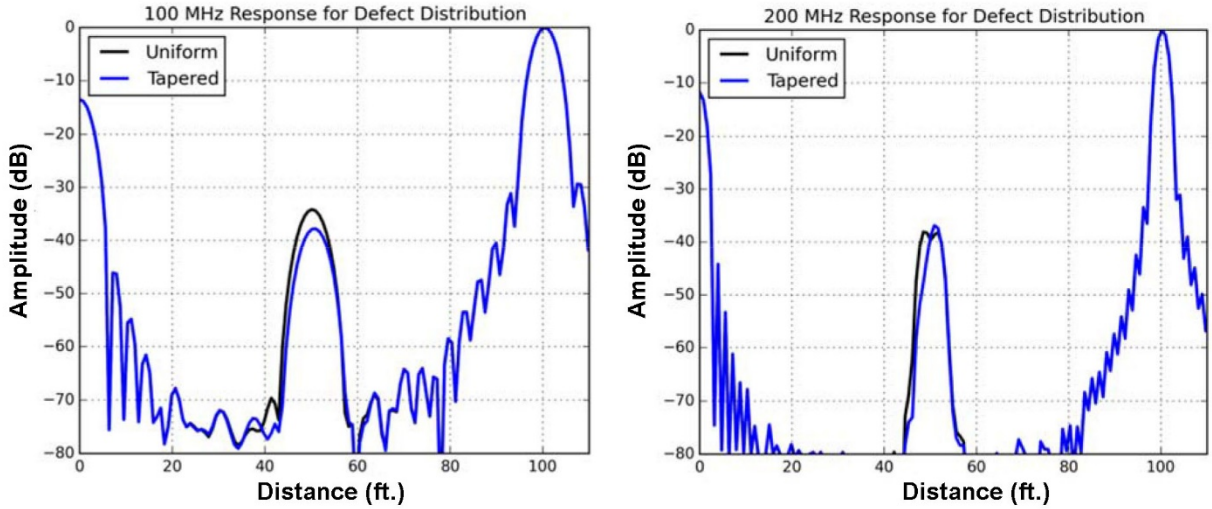


Figure 9.25. (*left*) 100 MHz and (*right*) 200 MHz ANSYS simulations for uniform and single-sided tapered 2.5 ft. defect sections of 100 ft. three-conductor shielded cable.

The LIRA simulator module was also used to model the effects of defect distribution for the 2.5 ft. and 10 ft. defect lengths. A twisted-pair cable was studied with a symmetrically tapered increase in the local capacitance with a 5% maximum increase in the center of the defect. A 0.5% stochastic noise level was used to introduce a low-level noise floor in these simulation models. Results from the 100 MHz LIRA simulations for the two tapered defect lengths are shown in Figure 9.26. In both cases, the results are similar to the results from the ANSYS simulations with the reflection from the tapered damage sections lower than the corresponding uniform damage models.

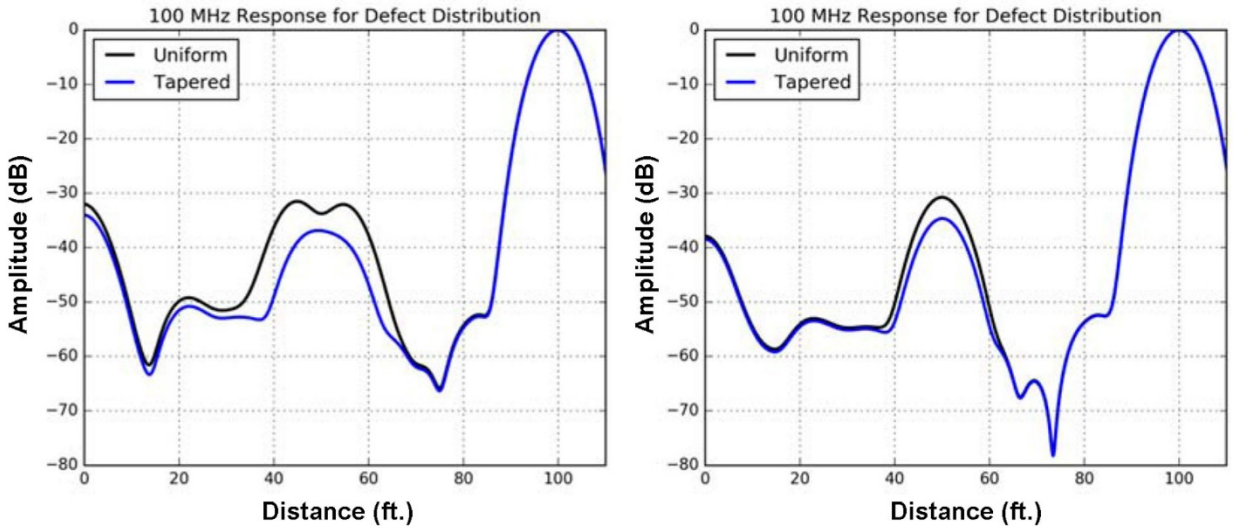


Figure 9.26. 100 MHz LIRA simulations for uniform and symmetrically tapered (*left*) 10 ft. and (*right*) 2.5 ft. defect sections of twisted-pair cable.

Quantifying the effect of reflection peak variations under typical field conditions would be difficult because a damage profile may be impossible to predict. However, it can be understood from the modeled cases that a ramped damage profile will exhibit an FDR response level different than a uniform damage profile. The defect peak amplitude also varies based on the highest frequency used in the sweep.

## 9.4 Cable Length

The defects that have been studied with FDR measurements under this program have been located in cables that are approximately 100 ft. in length (Glass et al. 2016b). The shorter lengths make the test cables more manageable to work with for accelerated aging and defect characterization studies. While these lengths are in the expected range of cable runs in plants, it is straightforward to run longer cables using the simulation models. One factor that affects a practical FDR measurement is the cable attenuation, which limits the bandwidth used to characterize the cable since losses increase with increasing frequency.

The ANSYS and LIRA simulation tools were used to perform a comparative study for low-loss cables having lengths of 100 ft. and 500 ft. containing the same defect at the halfway point of each cable. The ANSYS simulations were performed for a three-conductor shielded cable with a defect consisting of a 1 ft. section with an 18% increase in the wire insulation dielectric constant. The Nexxim circuit simulation consisted of cascaded transmission line segments with the impedance of the defect segment obtained from an HFSS model. The 18% increase in the insulation dielectric constant corresponded to a 5.8% decrease in the characteristic impedance of the two wires used in the simulation. A 1% standard deviation from the baseline impedance was applied to the cascaded segments to provide a dynamic range of 35–40 dB in the FDR response (relative to the end termination peak).

ANSYS results for the 100 ft. and 500 ft. cables are shown in Figure 9.27 and Figure 9.28. The defect peak amplitude is ~12 dB and ~3 dB above the noise level in both cable length models for 200 MHz and 100 MHz, respectively. The quasi-periodic nature of the noise signal appearing in the 500 ft. cables is due to a non-random representation of the stochastic variations in the cascaded circuit model and would not be present in an actual measurement. A comparison of Figure 9.27 and Figure 9.28 also shows how the use of higher frequency bandwidths can improve defect detection for a given cable length.

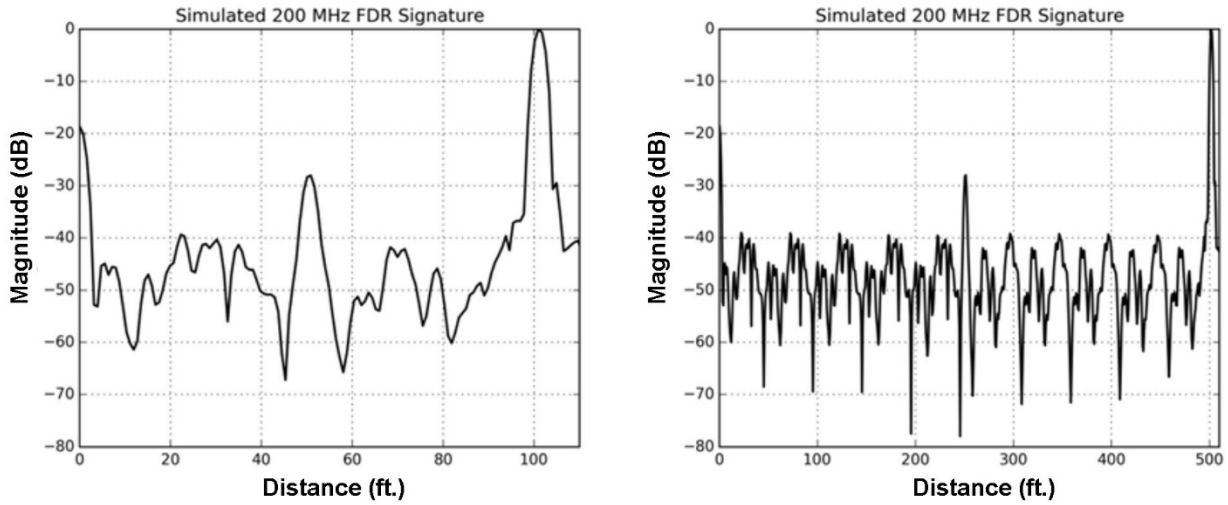


Figure 9.27. 200 MHz ANSYS simulations for 1 ft. defect section at location halfway along (*left*) 100 ft. and (*right*) 500 ft. three-conductor shielded cables.

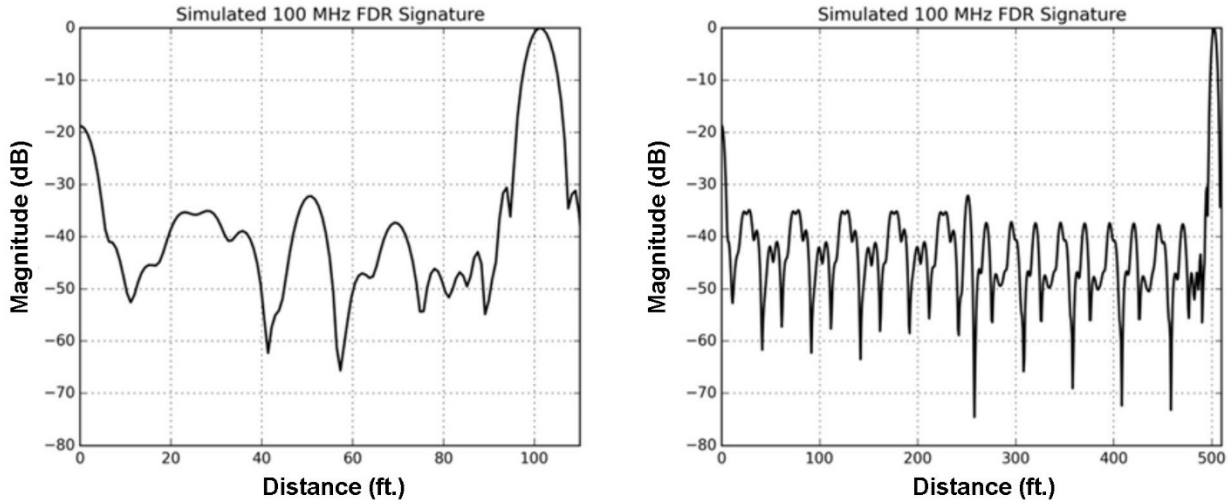


Figure 9.28. 100 MHz ANSYS simulations for 1 ft. defect section at location halfway along (*left*) 100 ft. and (*right*) 500 ft. three-conductor shielded cables.

A corresponding LIRA simulation was performed for a twisted-pair cable with an 18% increase in the local capacitance in a 1 ft. section located in the center of 100 ft. and 500 ft. cables. A 2.5% stochastic noise setting was specified to obtain a dynamic range of 35–40 dB in the FDR signature plot (relative to the end termination peak). The 100 MHz simulation results are shown in Figure 9.29. The defect peak amplitude is ~15 dB above the average noise level in the 100 ft. cable model and ~8 dB above the average noise level in the 500 ft. cable model. This is due primarily to the increased noise level present in the 500 ft. simulation result. In both cases, the stochastic algorithm in the LIRA simulator was set to discretize each damaged or undamaged cable segment into 200 mesh subsegments.

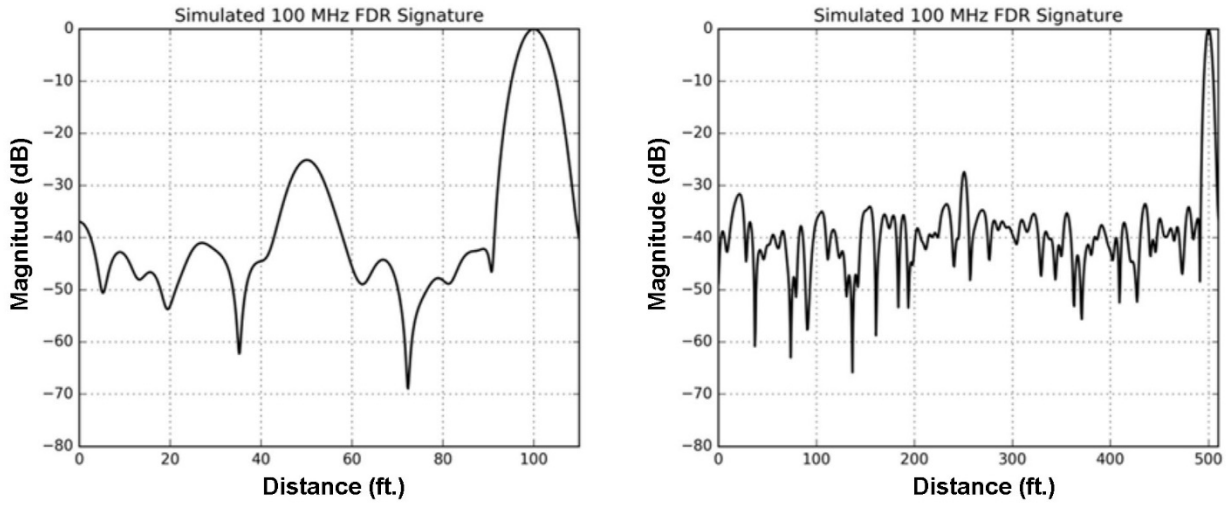


Figure 9.29. 100 MHz LIRA simulations for 1 ft. defect section at location halfway along (*left*) 100 ft. and (*right*) 500 ft. twisted-pair cables.

## 9.5 Defect Location

One of the limitations of the FDR method is the inability to inspect regions near the cable ends due to the large reflections at these locations. The exact performance of an FDR system is a function of the cable velocity factor, swept bandwidth, and signal processing techniques. To investigate the influence of defect location for 100 MHz and 200 MHz cases, ANSYS simulations were performed with a 3 ft. cable segment assigned a uniform 5% increase in insulation dielectric constant at 10, 50, and 90 ft. locations along a 100 ft. three-conductor shielded cable. No stochastic noise was added in the circuit simulation. As in all other ANSYS simulation cases, a Hanning window function and zero-padding were applied as part of the inverse Fourier transform used to create the reflectogram trace.

The ANSYS simulation results are shown in Figure 9.30 through Figure 9.32. For defects near the cable ends, the 100 MHz peaks were not clearly separable from the strong cable end signal. Although the defect was more apparent in the 200 MHz FDR traces, the noise level that will be present for an actual cable measurement may complicate interpretation and decrease detection confidence in such near-termination instances. The peak at 50 ft. was clearly visible in both the 100 MHz and 200 MHz simulations. The peak amplitudes from defects further along the cable were lower since the cable loss was not subtracted from the simulation.

A series of 100 MHz LIRA simulations was also performed with a 3 ft. cable segment assigned a uniform 5% increase in local capacitance at 10, 50, and 90 ft. locations along a 100 ft. twisted-pair cable. Stochastic noise levels of 0.5% and 2.5% were used to illustrate the impact of cable noise on defect detection. These settings yielded FDR dynamic ranges of approximately 50 dB and 35 dB relative to the end termination peak, respectively.

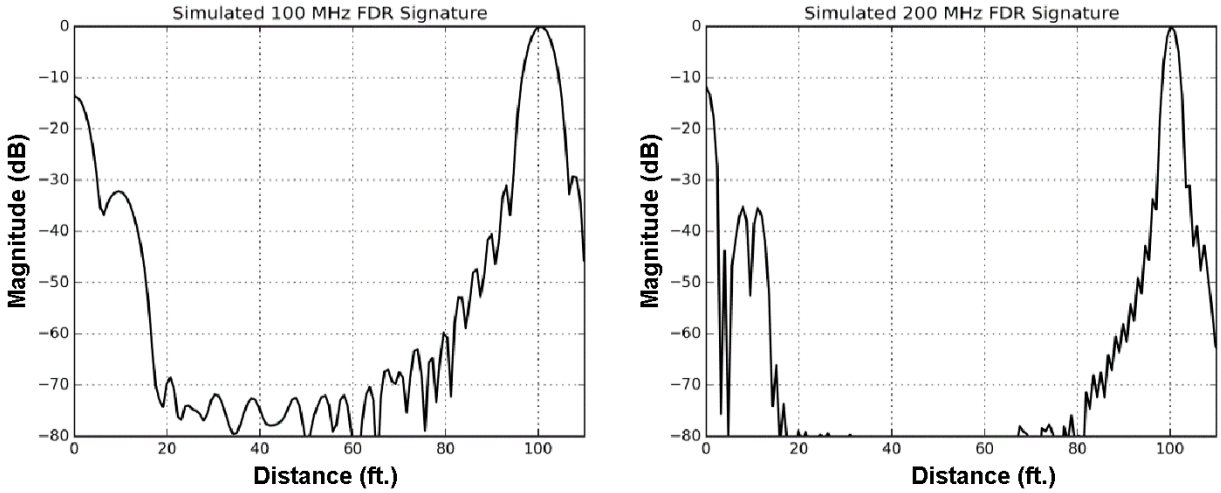


Figure 9.30. (*left*) 100 MHz and (*right*) 200 MHz ANSYS simulations for 3 ft. defect section centered at 10 ft. of 100 ft. three-conductor shielded cable.

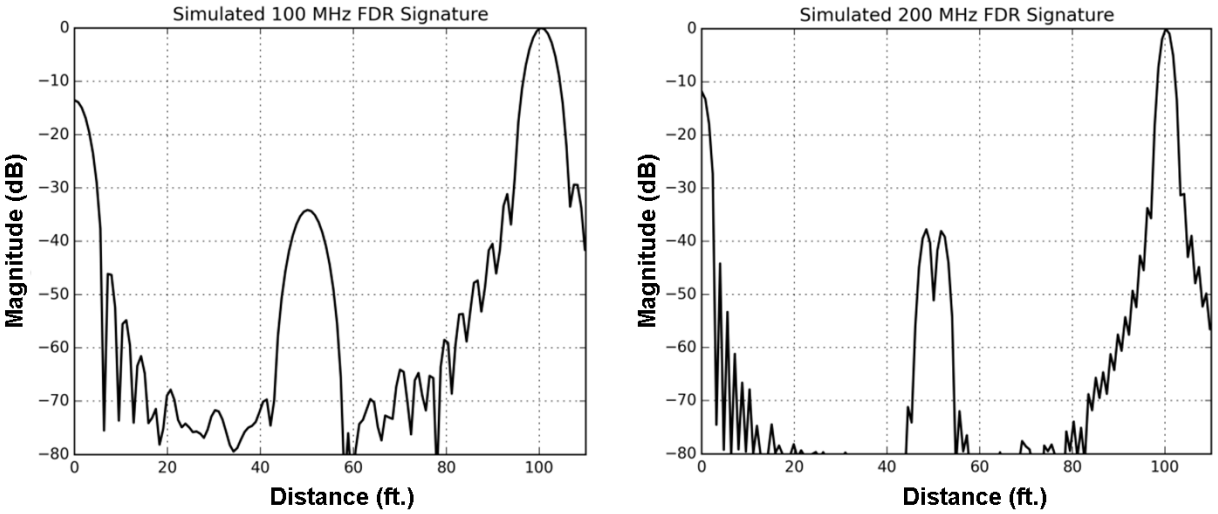


Figure 9.31. (*left*) 100 MHz and (*right*) 200 MHz ANSYS simulations for 3 ft. defect section centered at 50 ft. of 100 ft. three-conductor shielded cable.

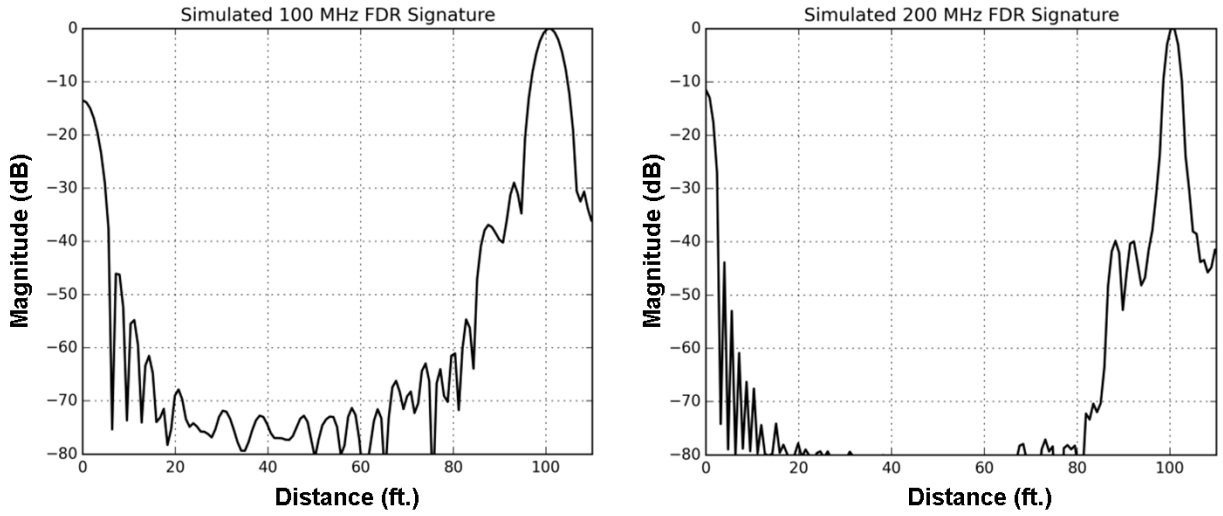


Figure 9.32. (*left*) 100 MHz and (*right*) 200 MHz ANSYS simulations for 3 ft. defect section centered at 90 ft. of 100 ft. three-conductor shielded cable.

The results of the LIRA simulations are shown in Figure 9.33 through Figure 9.35. For defects near the beginning of the cable, the defect peak was visible due to the lack of a prominent peak at the start of the cable. Depending on the LIRA settings used for test lead probe compensation, the beginning peak can have a wide range of amplitudes. The spatial resolution for this cable is approximately 3 ft. for the 100 MHz bandwidth simulation. The peak at 50 ft. was clearly visible in the 0.5% stochastic noise level simulations. The defect at the end of the cable was significantly above the noise level for the 0.5% stochastic noise setting. Confidence in the detection of small defects in these locations would be enhanced by the use of a baseline reference dataset for a given cable.

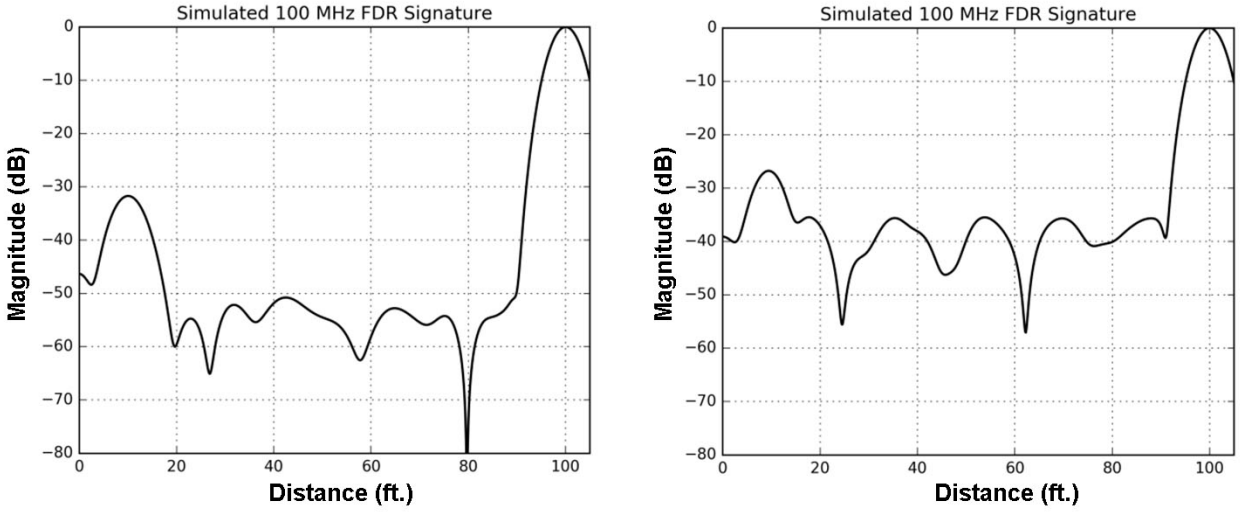


Figure 9.33. 100 MHz LIRA simulations for 3 ft. defect section centered at 10 ft. of 100 ft. twisted-pair cable with (*left*) 0.5% stochastic noise and (*right*) 2.5% stochastic noise settings.

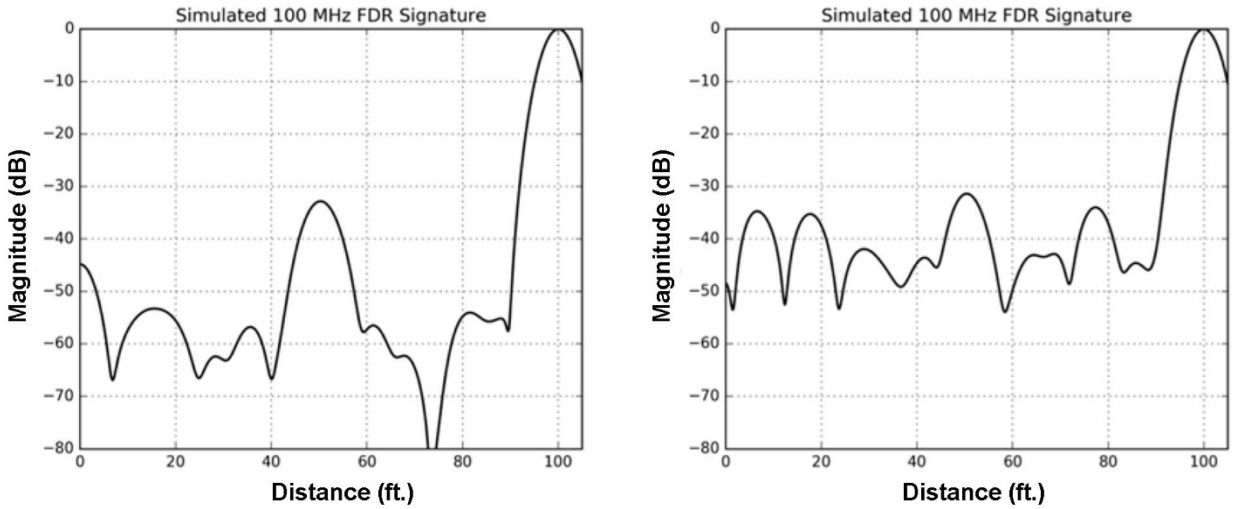


Figure 9.34. 100 MHz LIRA simulations for 3 ft. defect section centered at 50 ft. of 100 ft. twisted-pair cable with (*left*) 0.5% stochastic noise and (*right*) 2.5% stochastic noise settings.

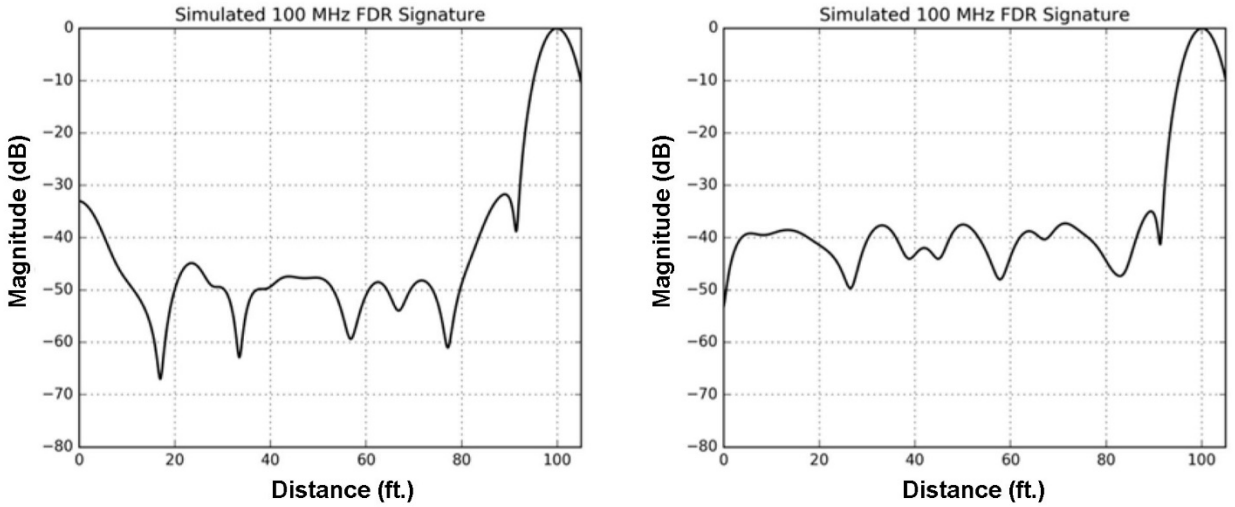


Figure 9.35. 100 MHz LIRA simulations for 3 ft. defect section centered at 90 ft. of 100 ft. twisted-pair cable with (*left*) 0.5% stochastic noise and (*right*) 2.5% stochastic noise settings.

## 9.6 Multiple Defects

One of the potential advantages of the FDR method is the ability of the swept-frequency signals to propagate through multiple defects to diagnose potential performance issues along a cable. A series of simulation cases were performed using bandwidths of 100 MHz and 200 MHz to evaluate the potential impact of multiple defects on a single defect response. In the first scenario, ANSYS simulation models were created to sequentially introduce three identical defects at 25 ft., 50 ft., and 75 ft. locations along a 100 ft. three-conductor shielded cable. The defects were represented by a uniform 5% increase in insulation dielectric constant over a 3 ft. section. No stochastic noise representing the effect of cable fabrication tolerances was added in the Nexxim circuit simulation.

The results of this simulation study are shown in Figure 9.36 through Figure 9.39. The peak responses were essentially independent of the presence or absence of additional defects along the cable length. The peaks at 75 ft. were slightly lower than the peaks at 25 ft. since the insertion loss of the cable was not

subtracted from the simulation data. The individual peaks at the beginning and end of the defect section were visible in the 200 MHz reflectograms since the 3 ft. defect length was greater than the resolution of approximately 1.5 ft.

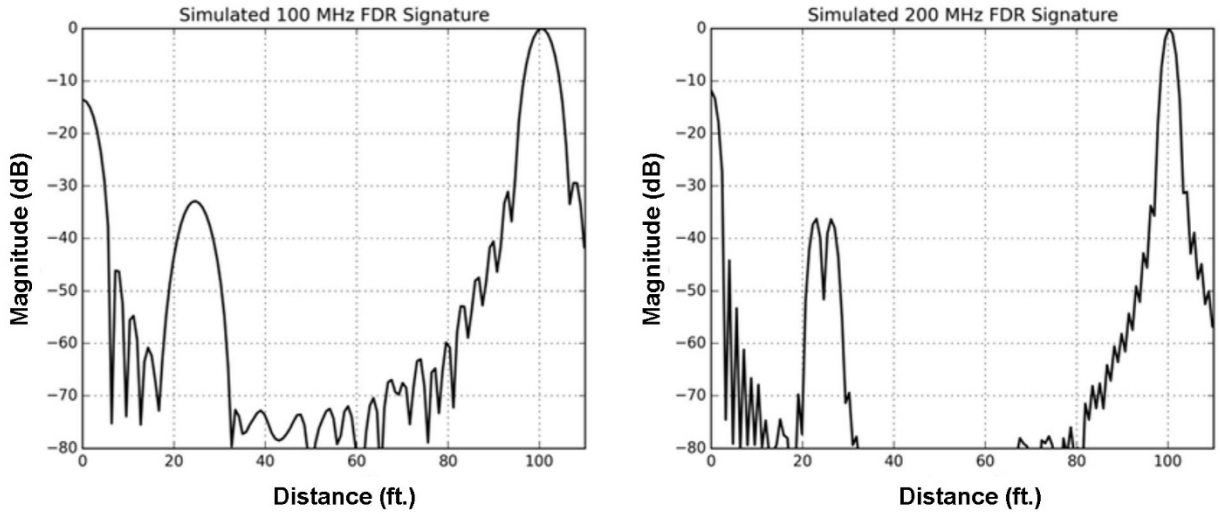


Figure 9.36. (*left*) 100 MHz and (*right*) 200 MHz ANSYS simulations of 3 ft. defect section at 25 ft. along 100 ft. three-conductor shielded cable

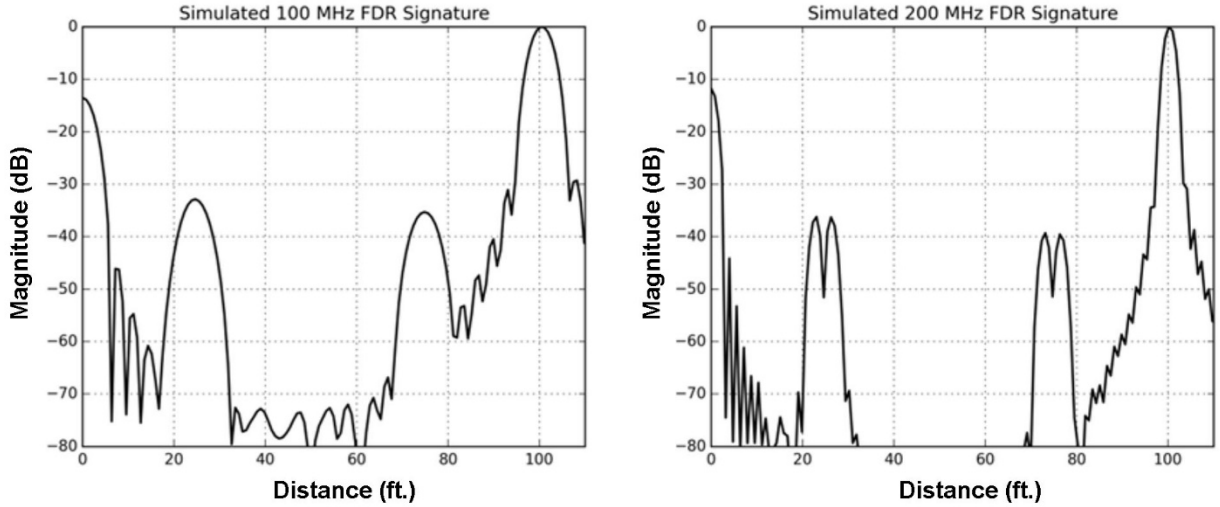


Figure 9.37. (*left*) 100 MHz and (*right*) 200 MHz ANSYS simulations of 3 ft. defect sections at 25 ft. and 75 ft. along 100 ft. three-conductor shielded cable.

The LIRA simulator was used to model multiple identical defects, and the results agreed well with the conclusions from the ANSYS models. The LIRA simulator was then used to model multiple defects of different severity along the cable length. These cases used a 100 ft. twisted-pair cable with a stochastic noise setting of 0.5% to represent cable fabrication tolerances. The defects were represented by 3 ft. sections with capacitance increases of 15% at 25 ft. and 50 ft. and 5% at 75 ft.

The results of these LIRA simulations are shown in Figure 9.39. The peak responses were substantially the same independent of the presence or absence of additional defects along the cable length. The peak amplitude at 75 ft. was not affected by the presence of the two larger peaks (and corresponding loss of signal) that occurred before it.

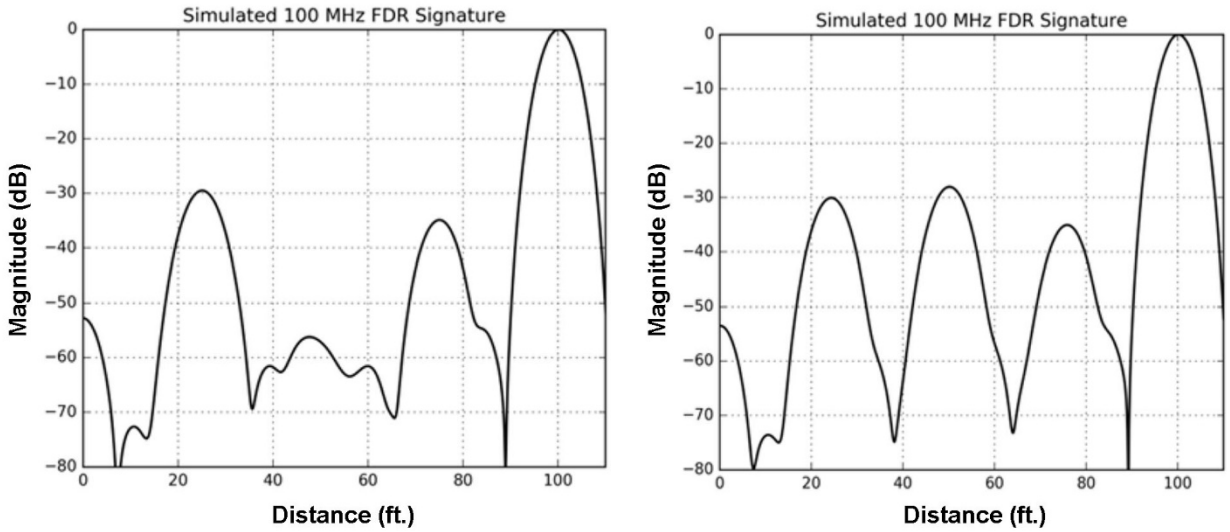


Figure 9.38. 100 MHz LIRA simulations for defect models consisting of (*left*) 15% capacitance increase at 25 ft. and 5% capacitance increase at 75 ft. and (*right*) additional 15% capacitance increase at 50 ft. for 100 ft. twisted-pair cable.

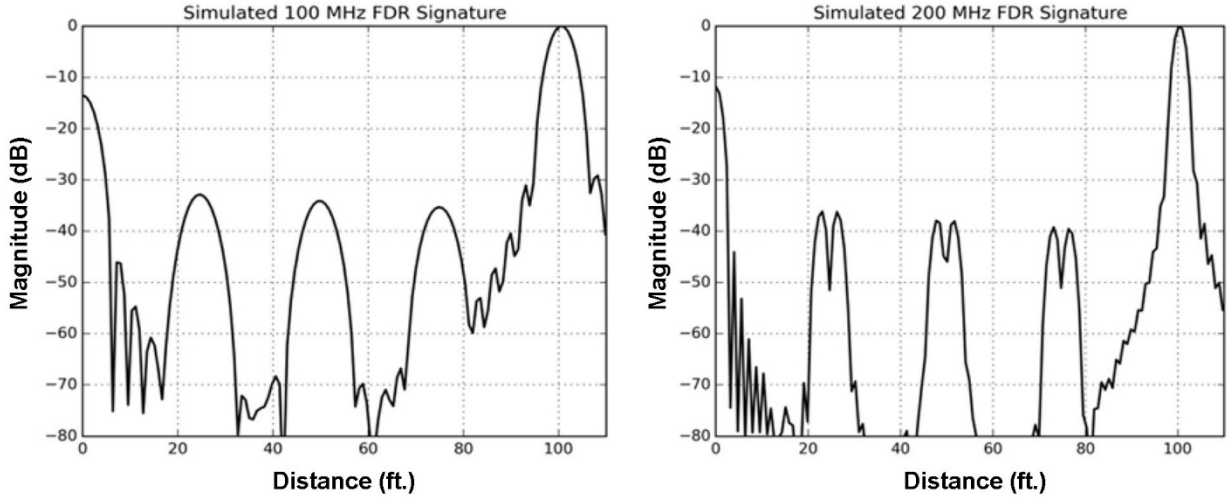


Figure 9.39. (*left*) 100 MHz and (*right*) 200 MHz ANSYS simulations of 3 ft. defect sections at 25 ft., 50 ft., and 75 ft. along 100 ft. three-conductor shielded cable.

In addition to the simulations, a series of measurements was collected for a 95 ft. section of three-conductor shielded cable that contained multiple mechanical defects along the cable length. Each mechanical defect consisted of a 6 in. section with the jacket and shield removed as shown in Figure 9.40. FDR datasets were collected using a VNA and the LIRA Acquire system. The VNA frequency spectrums were processed using the same procedure as the ANSYS simulated frequency spectrums.

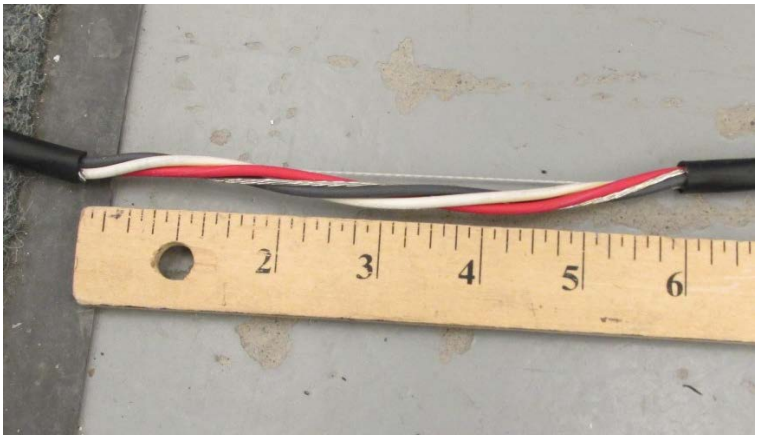


Figure 9.40. Mechanical defect consisting of 6 in. section of removed jacket and shield along the three-conductor shielded cable

Figure 9.41 and Figure 9.42 show the responses for the VNA measurements for the cable with defects located at 25 ft., 50 ft., and 75 ft. For bandwidths of 100 MHz and 200 MHz, the response at 75 ft. is well-resolved and the peak height is not affected by the introduction of the significant mechanical defects at 25 ft. and 50 ft. The peak amplitudes of defects located further along the cable are lower because the data is not adjusted to account for the cable signal attenuation characteristics. The trends in the FDR measurements are in good agreement with the simulations.

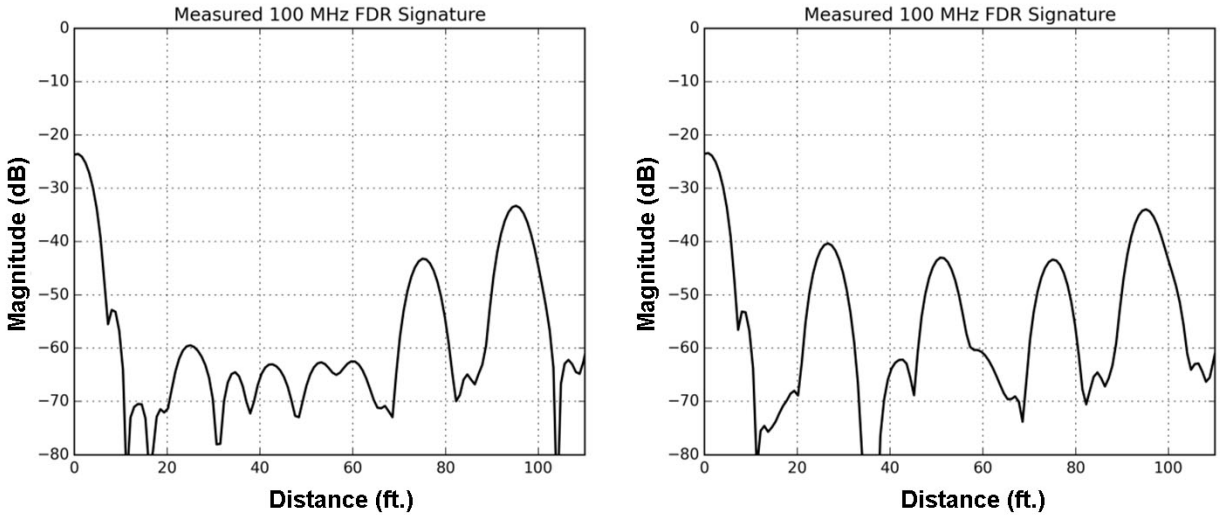


Figure 9.41. 100 MHz VNA measurements for defects consisting of 6 in. section of removed jacket and shield (*left*) at 75 ft. and (*right*) at 25 ft., 50 ft., and 75 ft. for 95 ft. three-conductor shielded cable.

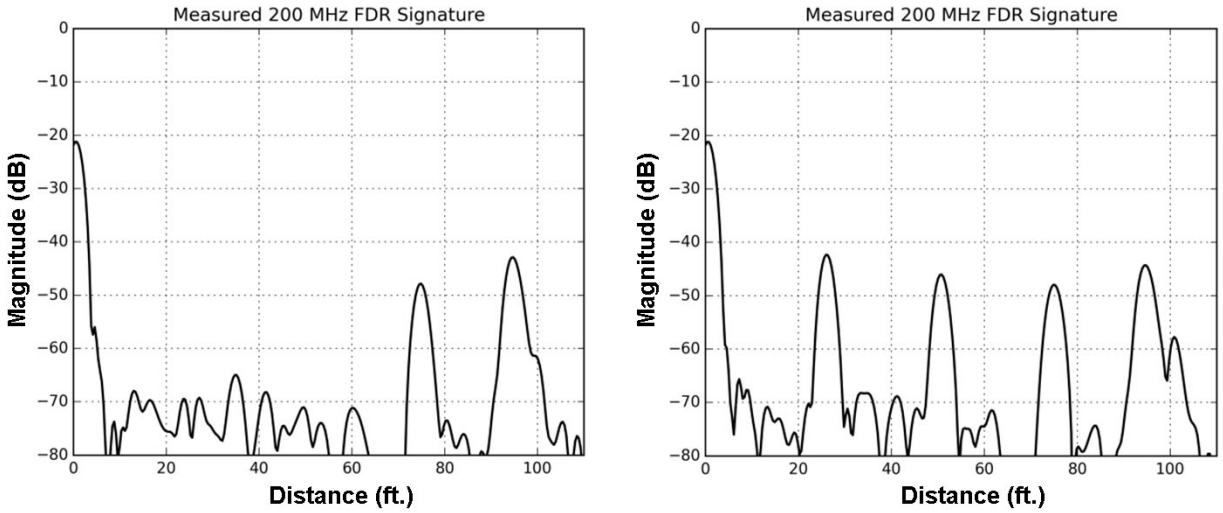


Figure 9.42. 200 MHz VNA measurements for defects consisting of 6 in. section of removed jacket and shield (*left*) at 75 ft. and (*right*) at 25 ft., 50 ft., and 75 ft. for 95 ft. three-conductor shielded cable.

Figure 9.43 shows the responses for the LIRA measurements for the cable with defects located at 25 ft., 50 ft., and 75 ft. For a bandwidth of 100 MHz, the response at 75 ft. is well-resolved and the peak height is not affected by the introduction of the significant mechanical defects at 25 ft. and 50 ft. The peak amplitudes of defects located further along the cable are lower because the data is not adjusted to account for the cable signal attenuation characteristics.

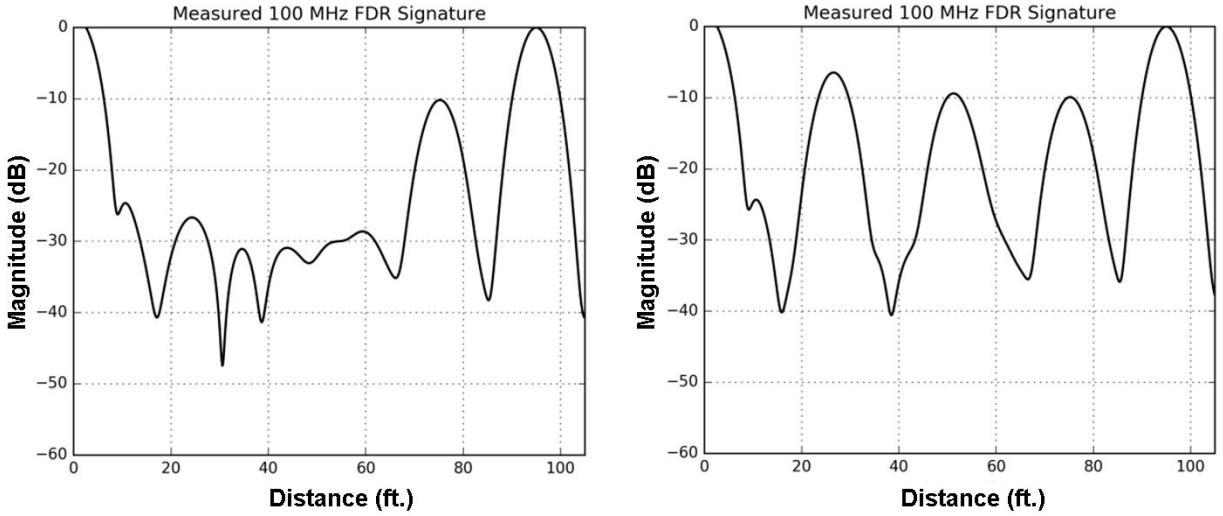


Figure 9.43. 100 MHz LIRA measurements for defects consisting of 6 in. section of removed jacket and shield (*left*) at 75 ft. and (*right*) at 25 ft., 50 ft., and 75 ft. for 95 ft. three-conductor shielded cable.

## 9.7 Use of Cable Extensions

As mentioned in Section 9.5, a complication involved with the use of the FDR method is difficulty detecting defects near the cable ends. A trade must be made between higher bandwidth and increased attenuation to maximize the spatial resolution along the cable while simultaneously ensuring inspection of the entire cable. For a given FDR bandwidth such as 200 MHz, a potential solution to mitigate the overshadowing cable end signal is to add an impedance-matched extension cable to the segment under test to artificially extend the length of the cable. This concept was explored using the ANSYS and LIRA simulation models.

The ANSYS model of the 100 ft. three-conductor shielded cable was simulated with a 3 ft. defect section centered at 5 ft. from the beginning of the cable. The defect was modeled as a uniform 5% increase in the insulation dielectric constant. No stochastic noise was added in the circuit model to represent the effects of cable fabrication tolerances. Figure 9.44 shows the 200 MHz simulated FDR response for this model, with the defect somewhat visible yet partially hidden in the response from the near-end peak.

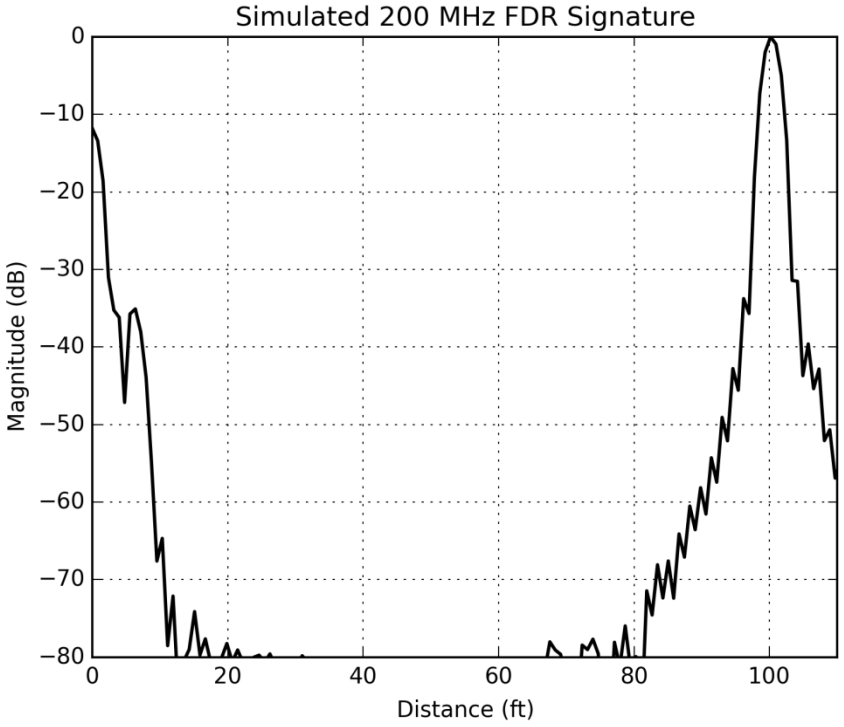


Figure 9.44. 200 MHz ANSYS simulation of 3 ft. defect section at 5 ft. along 100 ft. three-conductor shielded cable.

A series of simulation models was created to artificially extend the length of the cable by 10 ft. A 10 ft. extension cable was added before the 100 ft. cable to determine if it improved detection of the defect. The use of an impedance-matched cable with no impedance discontinuity at the connection point would simply extend the length of the cable being evaluated and move the defect peak to a location 15 ft. from the beginning peak. This case is assumed to be trivial and is not shown here. Cases of practical interest involve the use of dissimilar impedance cables and impedance discontinuities at the junction.

Figure 9.45 shows the results of adding a 10 ft. cable that is impedance-matched to the 62.67-Ohm cable under test, with a 50-Ohm short jumper wire to connect the cables. The 50-Ohm jumper connection was 2 in. long. The impedance-matched extension cable reduces the cable beginning peak by approximately 15 dB, but the defect detection at 5 ft. is only marginally better. The ability to detect the small defect may also be influenced by the stochastic noise produced by a given cable, especially for FDR measurement dynamic ranges of 35–40 dB (below the end termination peak).

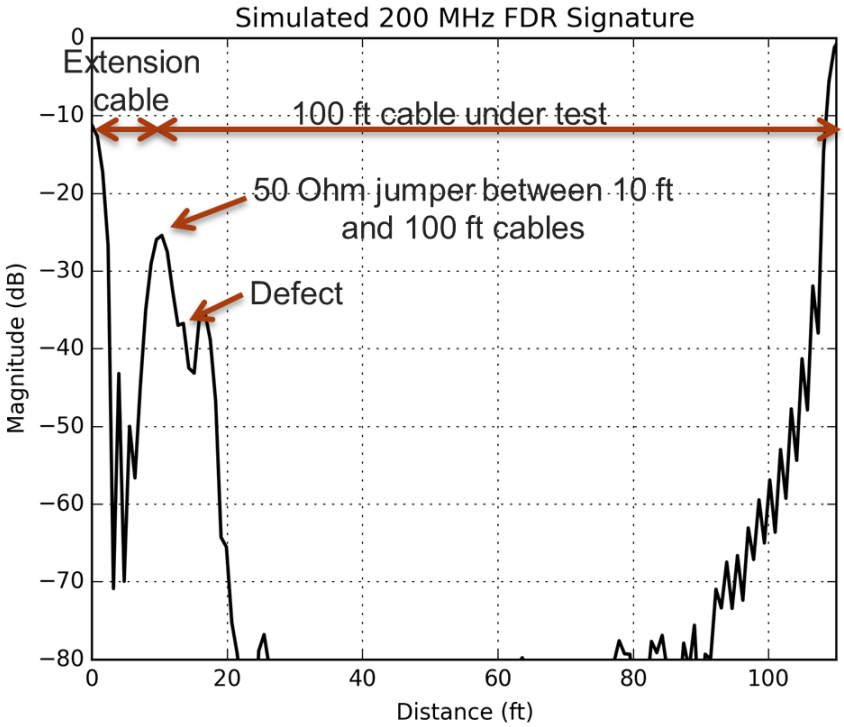


Figure 9.45. 200 MHz ANSYS simulation of 3 ft. defect section at 5 ft. along 100 ft. three-conductor shielded cable with 10 ft. impedance-matched extension cable.

Figure 9.46 shows the simulated results of adding a 10 ft. cable that is not impedance-matched to the 62.67-Ohm cable under test. In this case, the extension cable has an impedance of 50 Ohms. The extension cable does not significantly reduce the beginning peak and the defect response at 5 ft. is similar to the results from the original simulation model.

A corresponding set of cable extension models were analyzed using the LIRA simulator for a bandwidth of 100 MHz. The conclusions were in agreement with the ANSYS models, with even less of a benefit from the extension cable due to the lower bandwidth.

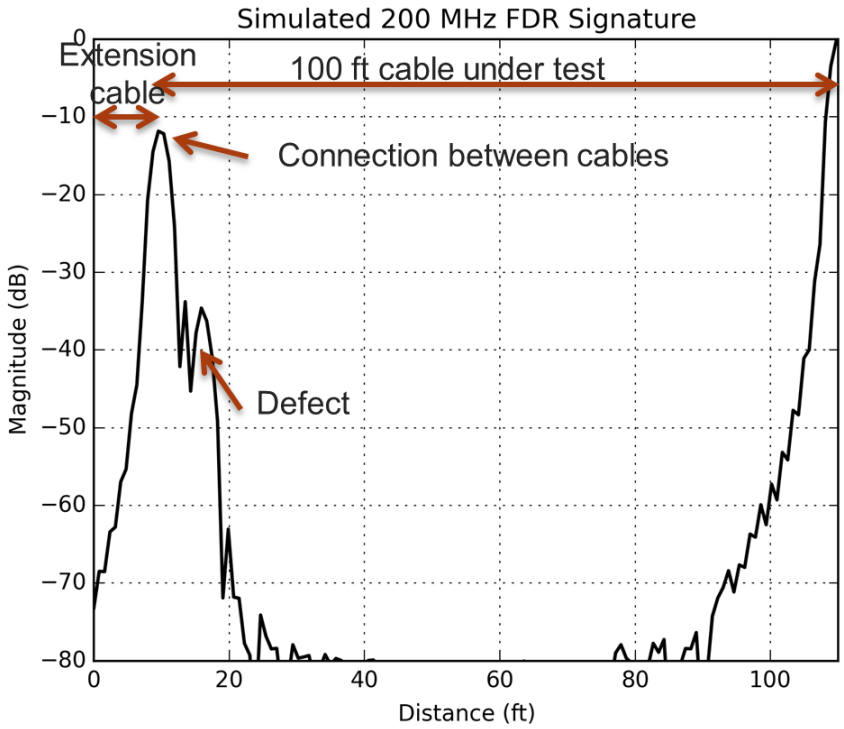


Figure 9.46. 200 MHz ANSYS simulation of 3 ft. defect section at 5 ft. along 100 ft. three-conductor shielded cable with 10 ft. 50-Ohm extension cable.

To support the simulation study on the use of extension cables, a series of measurements were performed using a 100 ft. three-conductor shielded cable to evaluate the addition of an extension cable to improve detection of a mechanical defect near the beginning of the cable. The defect consisted of a 12 in. section with the jacket and shield removed as shown in Figure 9.47. A VNA and the LIRA Acquire system were used to collect the measured FDR responses.

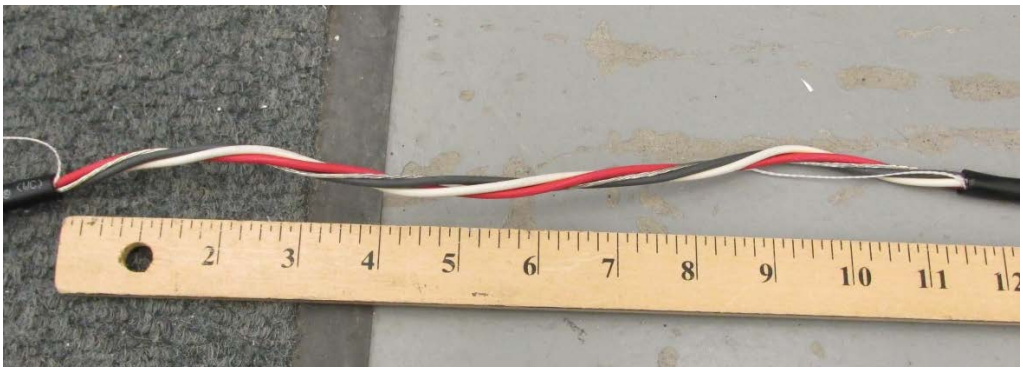

Figure 9.47. Mechanical defect consisting of 12 in. section of removed jacket and shield along the three-conductor shielded cable

Figure 9.48 shows the measured VNA FDR responses for bandwidths of 100 MHz and 200 MHz. A constant attenuation compensation factor was applied to remove the estimated signal loss of the cable. It is difficult to identify a defect at the 5 ft. location in the 100 MHz response. The 200 MHz response exhibits a series of reflections near the beginning of the cable at multiples of 5 ft., which are indicative of signal reverberations along the line due to the defect's significant impedance discontinuity at 5 ft.

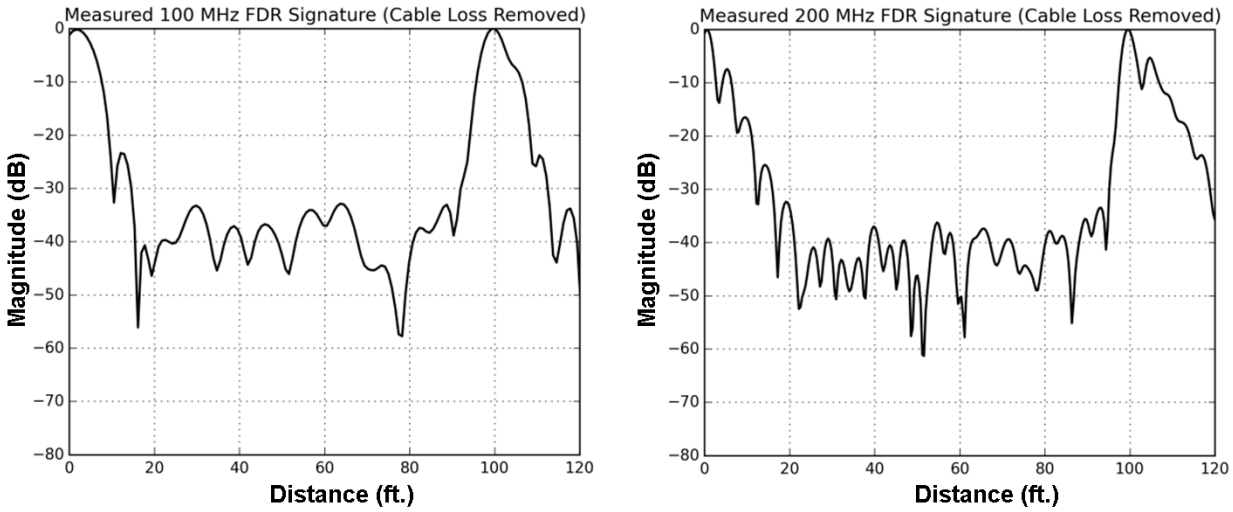


Figure 9.48. (left) 100 MHz and (right) 200 MHz VNA measurements of mechanical defect at 5 ft. along 100 ft. three-conductor shielded cable.

Figure 9.49 shows the measured LIRA FDR response for the cable for a bandwidth of 100 MHz. Again, it is difficult to readily distinguish between the expected peak at the beginning of the cable and the defect located at 5 ft.

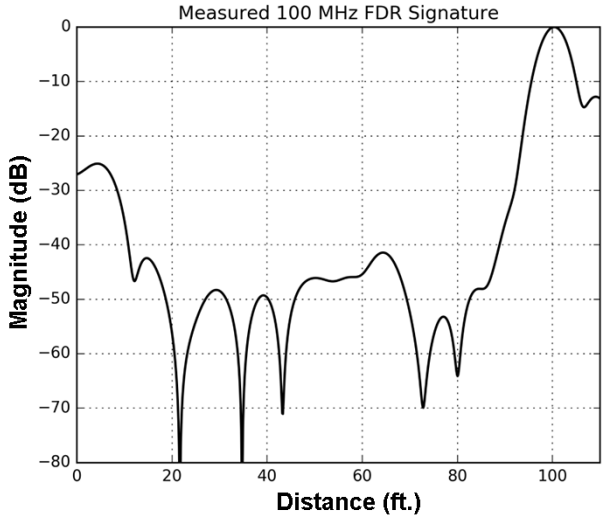


Figure 9.49. 100 MHz LIRA measurement of mechanical defect at 5 ft. along 100 ft. three-conductor shielded cable.

A 10 ft. extension cable was connected between the FDR instruments and the cable containing the defect. The cables were of the same type to represent a best-case scenario in which the two cables have the same characteristic impedance. The connection between the extension cable and cable being inspected was realized by twisting the individual wires together as shown in Figure 9.50. This represents a best-case scenario in which the impedance discontinuity created by the connection is minimized. Alligator clips were also used to connect the two cables and, as expected, this type of discontinuity produced a much larger peak that effectively shadowed the defect response.

Figure 9.50. Twisted wire connections made between 10 ft. extension cable and the 100 ft. three-conductor shielded cable under test.

Figure 9.51 shows the measured VNA FDR response for this test configuration. A constant attenuation compensation factor was applied to remove the estimated signal loss of the cable. A large reflection peak at the effective 15 ft. location from the measurement instrument (including the 10 ft. extension cable) is present in both the 100 MHz and 200 MHz responses. Additionally, the 200 MHz response shows a peak at the connection point located at 10 ft. from the measurement instrument, which is approximately 10 dB lower than the defect peak amplitude. At least one reflection from the defect and connection pair can be seen in both responses at distances further down the cable.

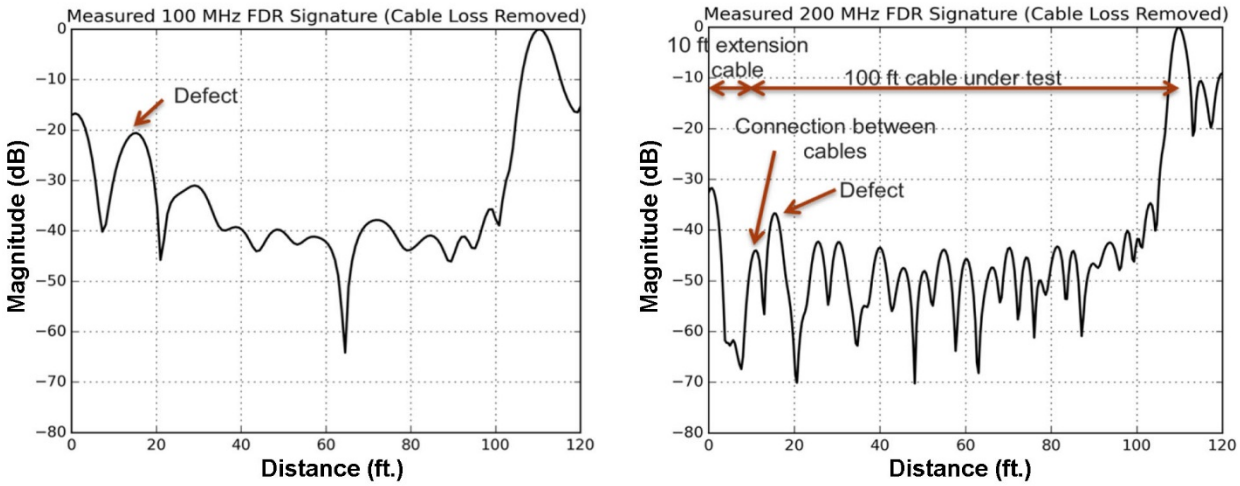


Figure 9.51. (*left*) 100 MHz and (*right*) 200 MHz VNA measurements of mechanical defect at 5 ft. along 100 ft. three-conductor shielded cable with 10 ft. identical extension cable.

Figure 9.52 shows the measured LIRA FDR response for this test configuration using a bandwidth of 100 MHz. A large reflection peak at the effective 15 ft. location from the measurement instrument (including the 10 ft. extension cable) is clearly visible.

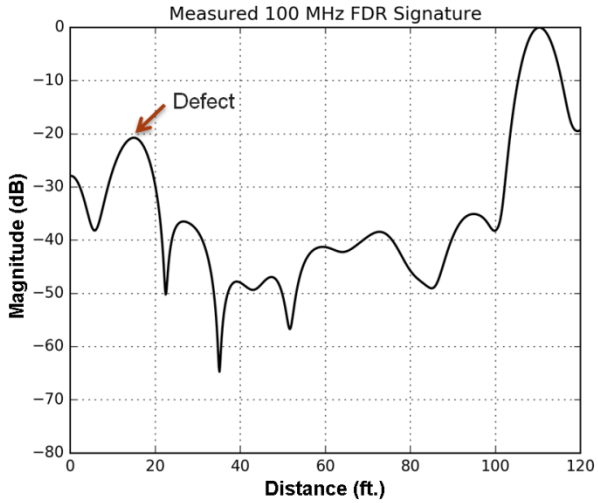


Figure 9.52. 100 MHz LIRA measurement of mechanical defect at 5 ft. along 100 ft. three-conductor shielded cable with 10 ft. identical extension cable.

The measurements indicated that the use of an extension cable can improve the defect detection under ideal laboratory conditions. Specifically, improvements were noted when the extension cable impedance was the same as the cable under inspection, the wires were twisted together to minimize reflections, and the defect was a 12 in. long complete removal of the shield and jacket. The physical length of the extension cable must also be compatible with the resolution of the FDR measurement in order to provide any benefit. Given the likelihood of these conditions not being met in actual field inspections, it appears improbable that this approach would increase the detection probability for defects located near the end of a cable.

## 9.8 Cable Termination

FDR testing is often performed without de-terminating the far end of the cable under test. Simulations were performed to assess the influence of the cable termination condition on the detection of a defect centered along the cable. The ANSYS model simulated a 100 ft. three-conductor shielded cable with a 3 ft. defect section centered at 50 ft. consisting of a uniform 5% increase in insulation dielectric constant. The LIRA model simulated a 100 ft. twisted-pair cable with a 3 ft. defect section centered at 50 ft. consisting of a uniform 5% increase in the local capacitance. For both models, the end termination conditions included a short circuit, open circuit, matched impedance, and 50-Ohm load. The ANSYS model framework used for this series of cases is shown in Figure 9.53.

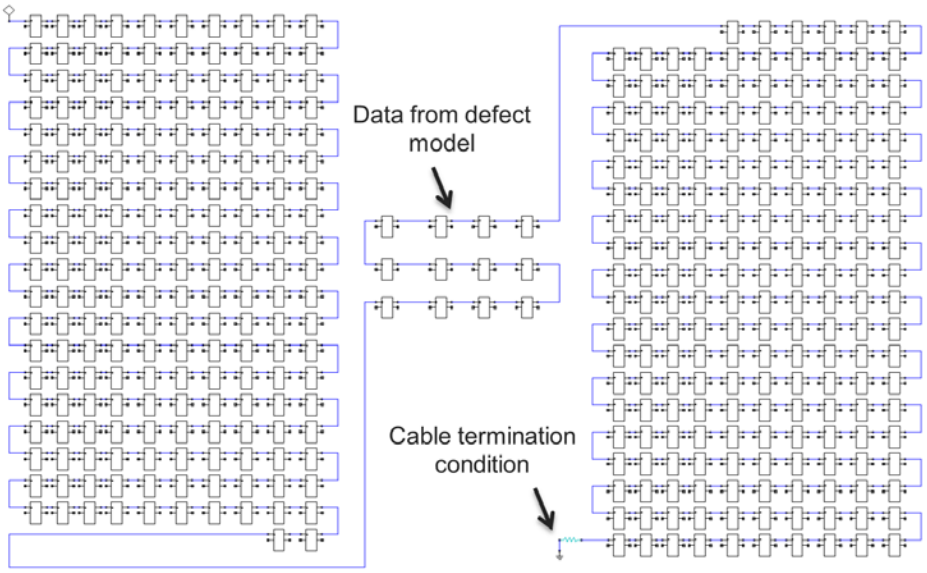


Figure 9.53. ANSYS simulation model consisting of cascaded S-parameter blocks to simulate damaged and undamaged cable segments with different end termination conditions.

Figure 9.54 shows the 100 MHz ANSYS and LIRA simulation results for the cable termination conditions. As predicted from transmission line principles, the short circuit and open circuit produced identical end peaks and the matched impedance produced the smallest end peak. The defect amplitude response was unaffected by the end termination value, except for the LIRA simulation of the impedance-matched termination. Since the LIRA technique is based on line resonances that exist along the cable length, it is compatible with an arbitrary termination condition except for an exact match to the cable impedance. The matched impedance condition makes the cable appear infinitely long due to the lack of reflections from the end of the cable.

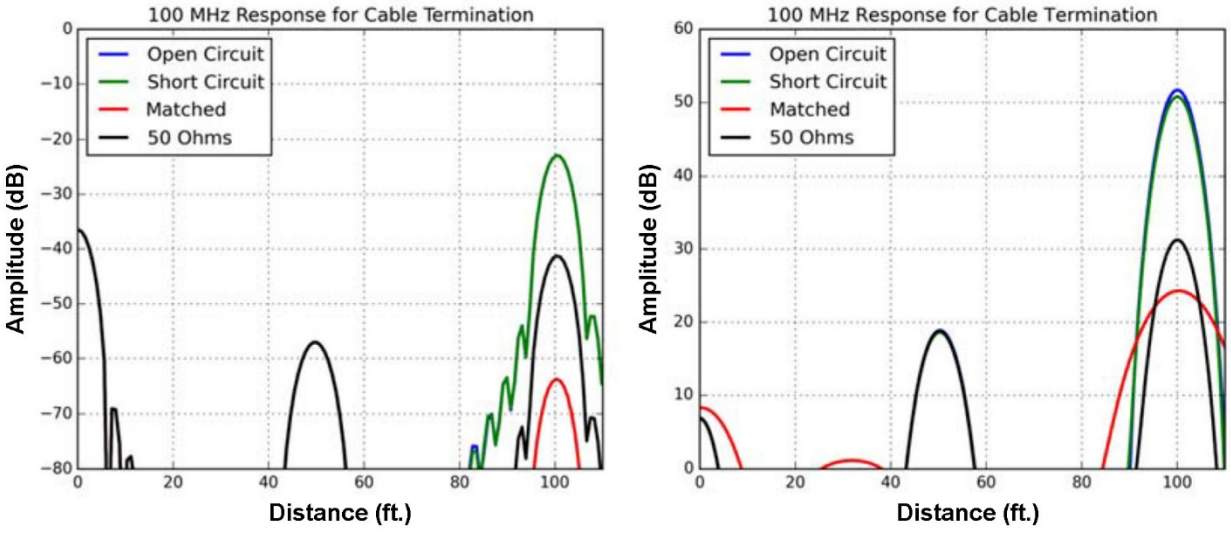


Figure 9.54. 100 MHz (*left*) ANSYS and (*right*) LIRA simulations of cable terminations for a 100 ft. cable with a 3 ft. defect section at 50 ft.

## 9.9 Cable Environment

It has previously been shown that the FDR response of a multi-conductor unshielded cable can be sensitive to the surrounding environment. In one study (Glass et al. 2016b), a 100 ft. unshielded three-conductor cable with a short section at 50 ft., which had mechanical damage (insulation removed), was tested with the 100 MHz LIRA system. When the damaged short section was placed on concrete, wood, and aluminum, a change in the FDR damage indication peak of approximately 10 dB was observed as shown in Figure 9.55. As may be expected, no effect was noted when this test was performed with a shielded cable since the shield isolates the cable signals from the external environment.

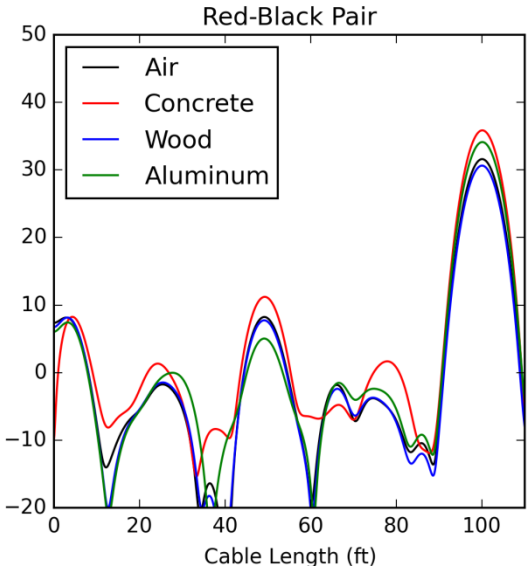


Figure 9.55. 100 MHz LIRA measurements for 100 ft. unshielded three-conductor cable with different types of environmental conditions at the 50 ft. mechanically damaged location.

To follow up on these previous measurements, a series of ANSYS simulations was performed to model the effects of the local environment on an unshielded cable. The cable was an unshielded version of the 100 ft. three-conductor cable given in Table 6.1. The cable was placed in contact with air, aluminum, and carbon steel along a short section at the center of the total length. Figure 9.56 shows plots of the predicted electric field amplitude at 100 MHz for cross sections of the unshielded cable in free space and placed on a 0.25 in. thick aluminum support plate. The external field distribution is significantly affected by the presence of the metal plate, with the plate shadowing the area within the lower half of the model.

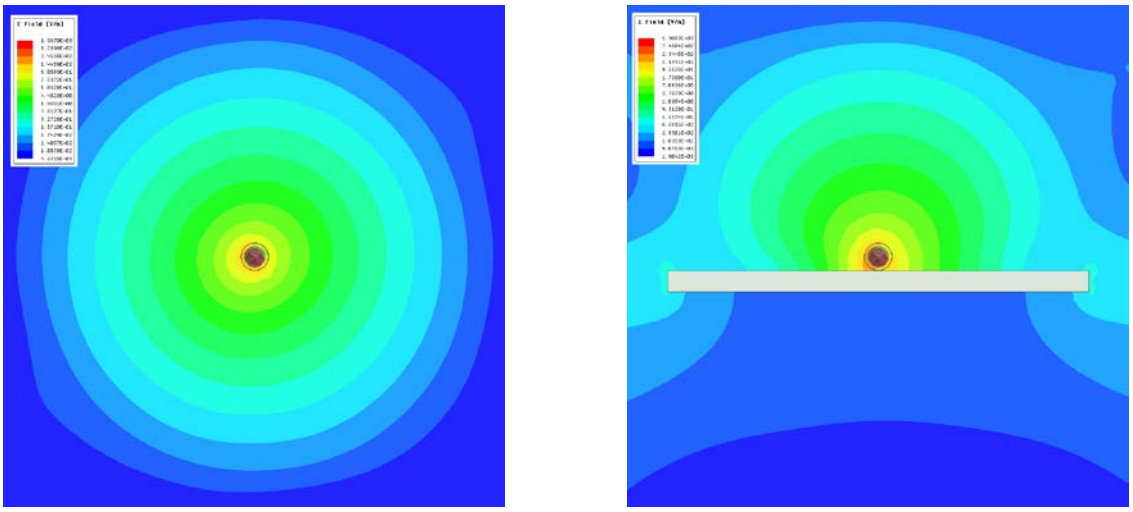

Figure 9.56. ANSYS simulated electric field magnitude at 100 MHz for unshielded cable cross-section (left) in free space and (right) on 0.25in. thick aluminum plate.

Corresponding simulation results are shown in Figure 9.57 for the aluminum plate placed below 6 in. and 12 in. sections of the unshielded cable. The simulations were performed for an FDR bandwidth of 200 MHz. Similar results were obtained for a bandwidth of 100 MHz. The presence of the 6 in. plate produced a reflection with a peak amplitude 35 dB below the end termination peak. The 12 in. plate increased the peak amplitude by 5 dB. Depending upon the stochastic noise present in a given cable measurement, these peaks may be noticeable above the noise level.

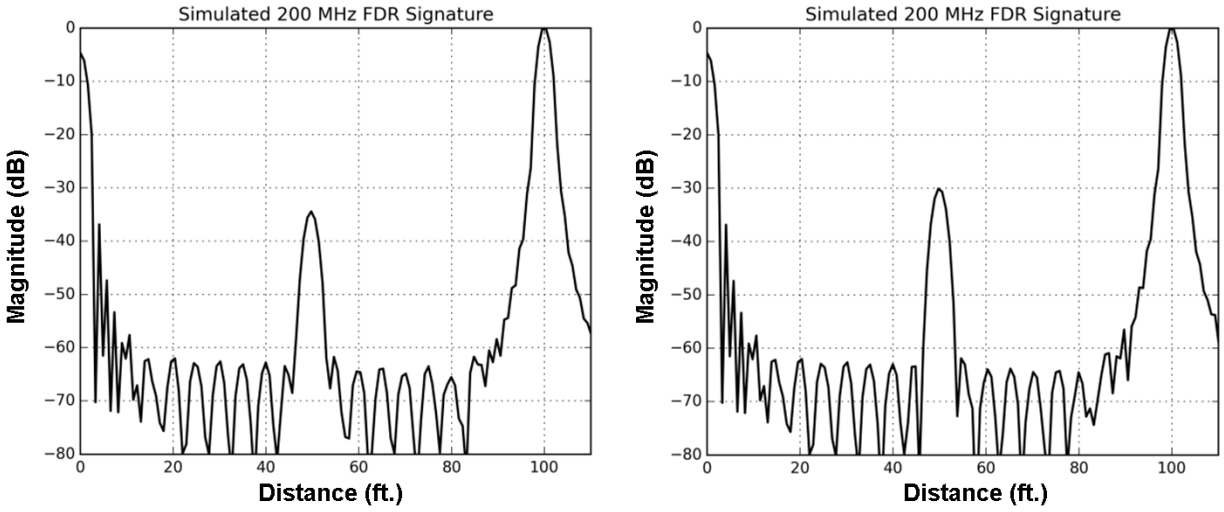


Figure 9.57. 200 MHz ANSYS simulation of 100 ft. unshielded three-conductor cable supported by (*left*) 6 in. long and (*right*) 12 in. long 0.25 in. thick aluminum plate at 50 ft.

Corresponding results are shown in Figure 9.58 for 6 in. and 12 in. long metal plates assigned the electrical properties of AISI 1010 carbon steel. The carbon steel was modeled using a conductivity of 7E6 S/m and magnetic permeability of 3290. The simulations were again performed for an FDR bandwidth of 200 MHz, with similar results obtained for a bandwidth of 100 MHz. The peak amplitudes at the carbon steel plate locations are similar to the results for the aluminum plate models.

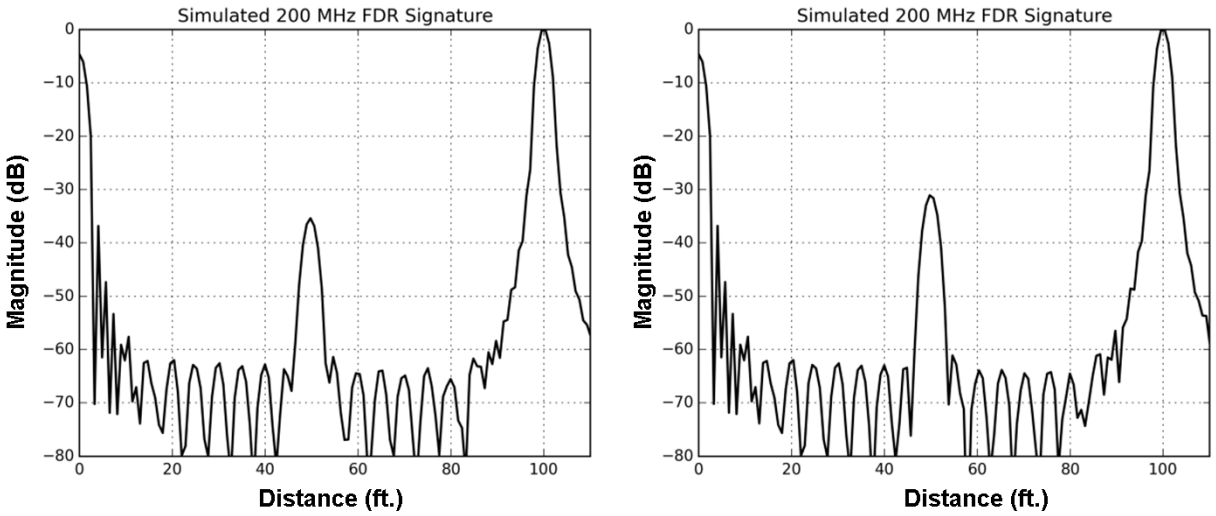


Figure 9.58. 200 MHz ANSYS simulation of 100 ft. unshielded three-conductor cable supported by (*left*) 6 in. long and (*right*) 12 in. long 0.25 in. thick carbon steel plate at 50 ft.

A series of ANSYS simulations was also performed to model the effect of water intrusion into the immediate vicinity of a short section of the cable. The dielectric properties of the unshielded three-conductor cable jacket were modified to simulate a fresh-water environment. The fresh water was modeled using a dielectric constant of 81 and electrical conductivity of 0.01 S/m. No stochastic noise was added in the circuit model to represent the effects of cable fabrication tolerances.

Figure 9.59 shows plots of the predicted electric field amplitude at 100 MHz for cross sections of the unshielded cable in free space and with fresh water as the cable jacket material. The external field distribution is significantly affected by the presence of the much higher dielectric constant, with the higher field levels much more confined.

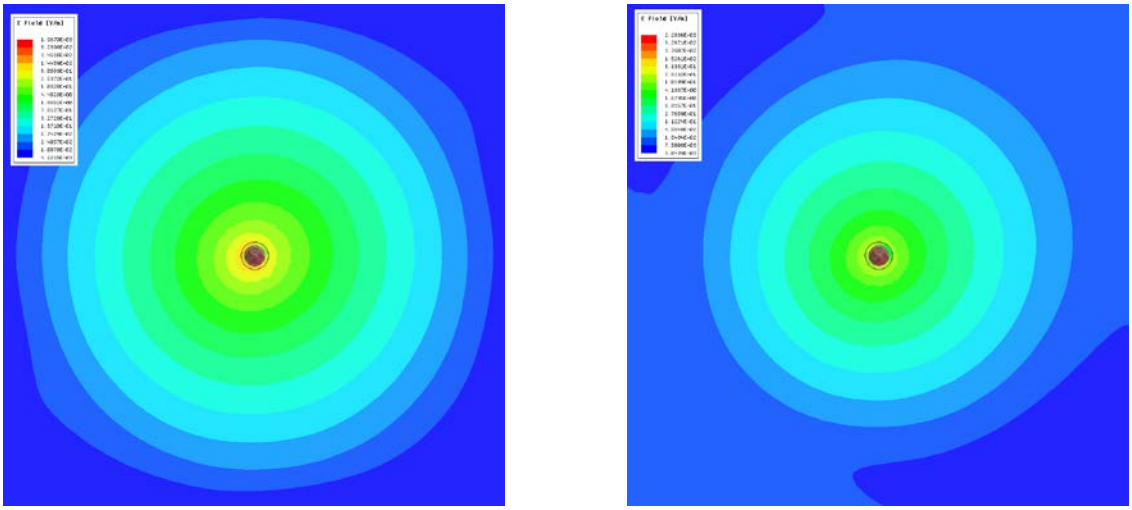

Figure 9.59. ANSYS simulated electric field magnitude at 100 MHz for unshielded cable cross section (*left*) in free space and (*right*) with fresh water as jacket material.

Corresponding simulation results are shown in Figure 9.60 for the fresh water used as the cable jacket for 6 in. and 12 in. sections of the unshielded cable. The simulations were performed for an FDR bandwidth of 200 MHz. Similar results were obtained for a bandwidth of 100 MHz. The presence of the water around the wires for a 6 in. long section produced a reflection with a peak amplitude 18 dB below

the end termination peak. The presence of the water for a 12 in. long section increased the peak amplitude by 3 dB. These higher peaks are much more likely to be detectable in an actual cable measurement, relative to the noise level.

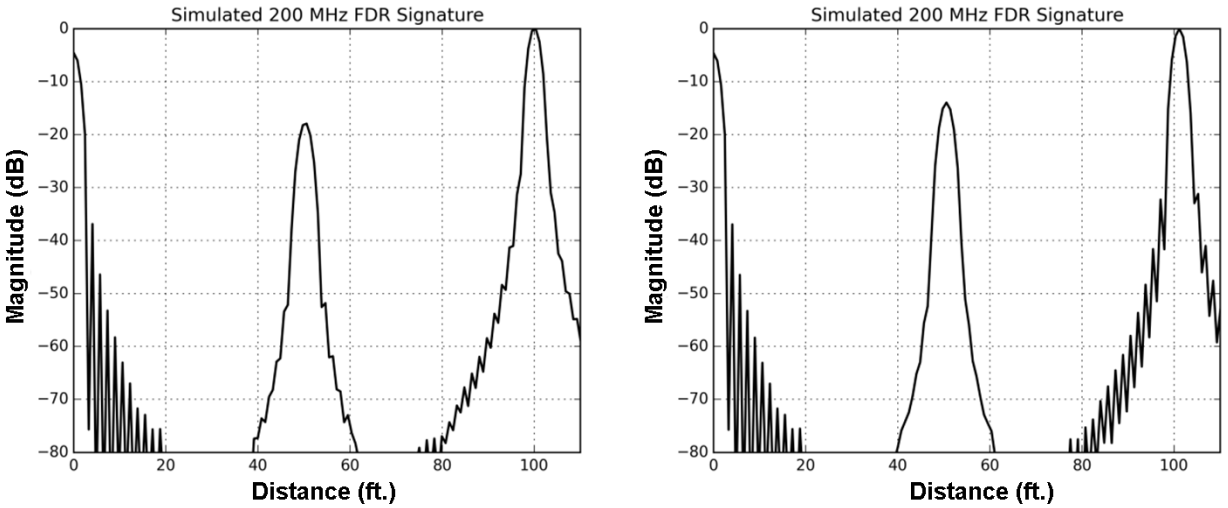


Figure 9.60. 200 MHz ANSYS simulation of 100 ft. unshielded three-conductor cable with jacket modeled as fresh water along (*left*) 6 in. and (*right*) 12 in. sections at 50 ft.

## 9.10 Frequency Bandwidth

The frequency bandwidth employed in the FDR method is an important parameter that significantly impacts the results. A higher bandwidth improves detection sensitivity and resolution, but is subject to increased attenuation as the swept-frequency signal propagates along the cable. Therefore, a tradeoff must be made to determine the bandwidth that is best suited for a cable inspection. In general, the inspection bandwidth must be reduced as the cable length increases.

A series of LIRA simulations was performed to study the use of higher bandwidths to detect defects in 100 ft. and 1000 ft. twisted-pair cables. This study was enabled by the acquisition of a newer version of the LIRA simulator module that could analyze models at frequencies higher than 100 MHz. The available higher bandwidth settings in the newer software release were 200 MHz, 400 MHz, 800 MHz, and 1300 MHz. For all simulations, a stochastic noise setting of 0.5% was used to represent the effects of random fluctuations in the electrical properties due to cable fabrication tolerances.

The LIRA simulated results for a 100 ft. cable with a dielectric loss tangent of 0.01 are shown in Figure 9.61. The defect was modeled as a 3 ft. section with a uniform 5% increase in capacitance centered at 50 ft. Cable signature plots are given for FDR bandwidths of 100 MHz, 200 MHz, 400 MHz, and 1300 MHz. The simulations demonstrate the improved resolution achievable with higher bandwidths, with distinct peaks at the beginning and end of the defect section for bandwidths of 200 MHz and above. The signal attenuation along the 100 ft. cable is low enough to use these bandwidths since the reflection from the end of the cable is visible in all cases.

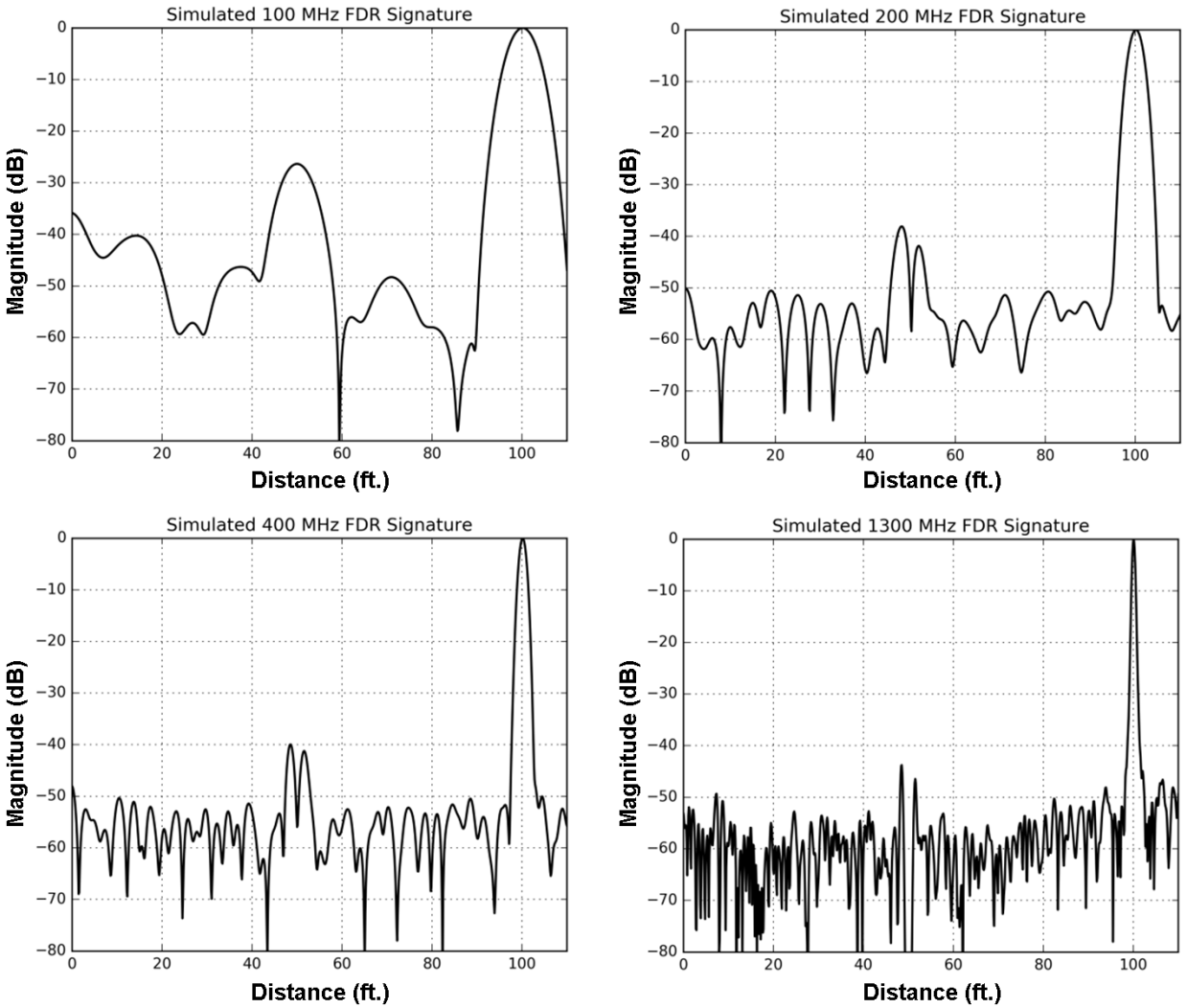


Figure 9.61. LIRA simulations of 100 ft. twisted-pair cable with loss tangent of 0.01 and 3 ft. defect section at 50 ft. for (*upper left*) 100 MHz, (*upper right*) 200 MHz, (*lower left*) 400 MHz, and (*lower right*) 1300 MHz.

The LIRA simulations were repeated for the 100 ft. cable with the dielectric loss tangent decreased to 0.0001. These results representing an extremely low-loss case are shown in Figure 9.62. The stochastic noise parameter was held constant from the previous cable simulation shown in Figure 9.61 to allow direct comparison of the defect response. For all simulated bandwidths, the defect responses and signal-to-noise ratio were unaffected by this range of loss tangents for inspection of this short cable.

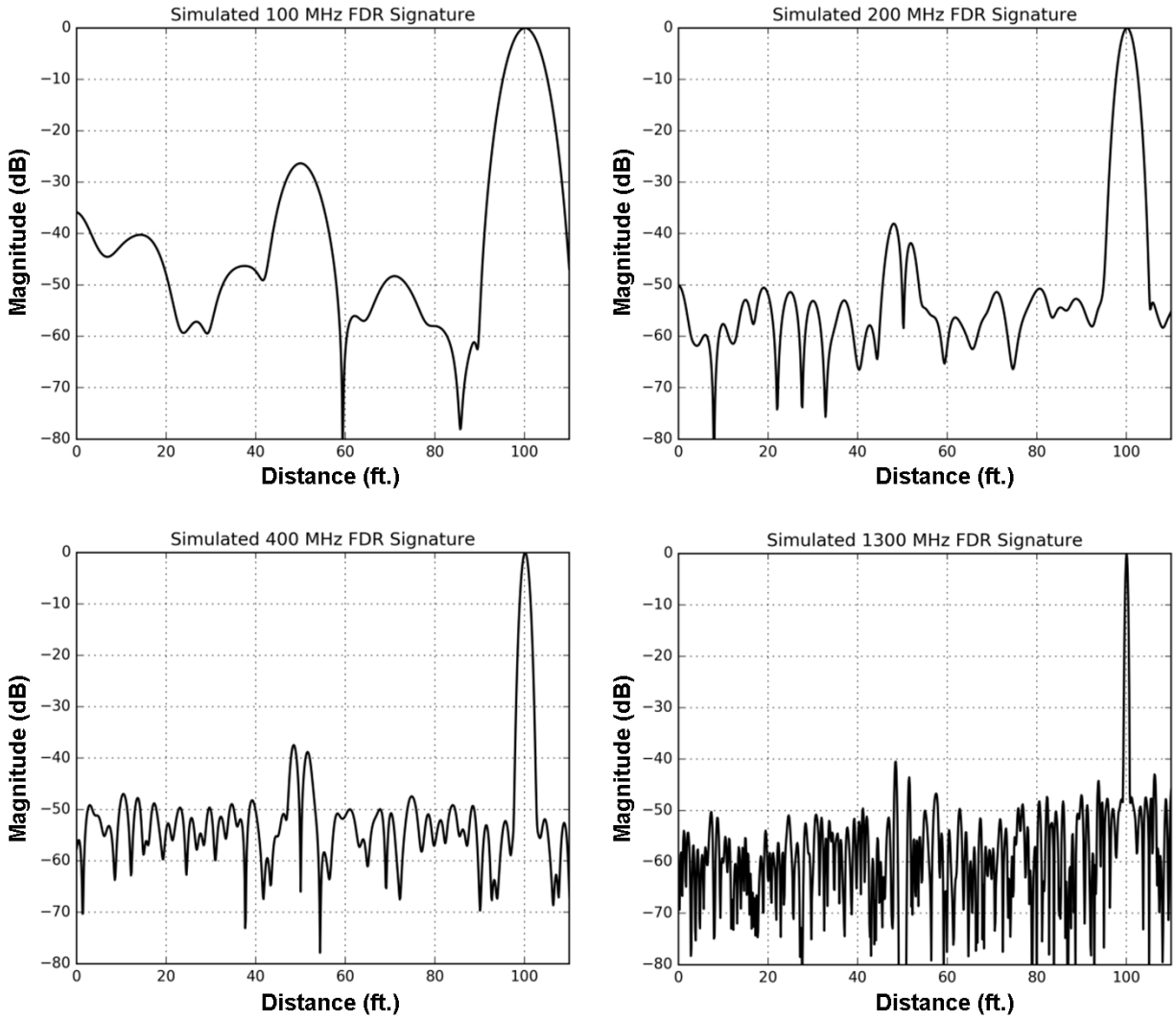


Figure 9.62. LIRA simulations of 100 ft. twisted-pair cable with loss tangent of 0.0001 and 3 ft. defect section at 50 ft. for (*upper left*) 100 MHz, (*upper right*) 200 MHz, (*lower left*) 400 MHz, and (*lower right*) 1300 MHz.

The results of LIRA simulations of a 1000 ft. twisted-pair cable with a dielectric loss tangent of 0.01 are shown in Figure 9.63. The defect was modeled as a 3 ft. section with a uniform 5% increase in capacitance centered at 800 ft. Cable signature plots are provided for FDR bandwidths of 10 MHz, 25 MHz, 50 MHz, and 100 MHz. For this cable model, it was found that signal attenuation limits the inspection bandwidth to several hundred MHz. The defect peak at 800 ft. is above the noise level in all signature plots except for 10 MHz.

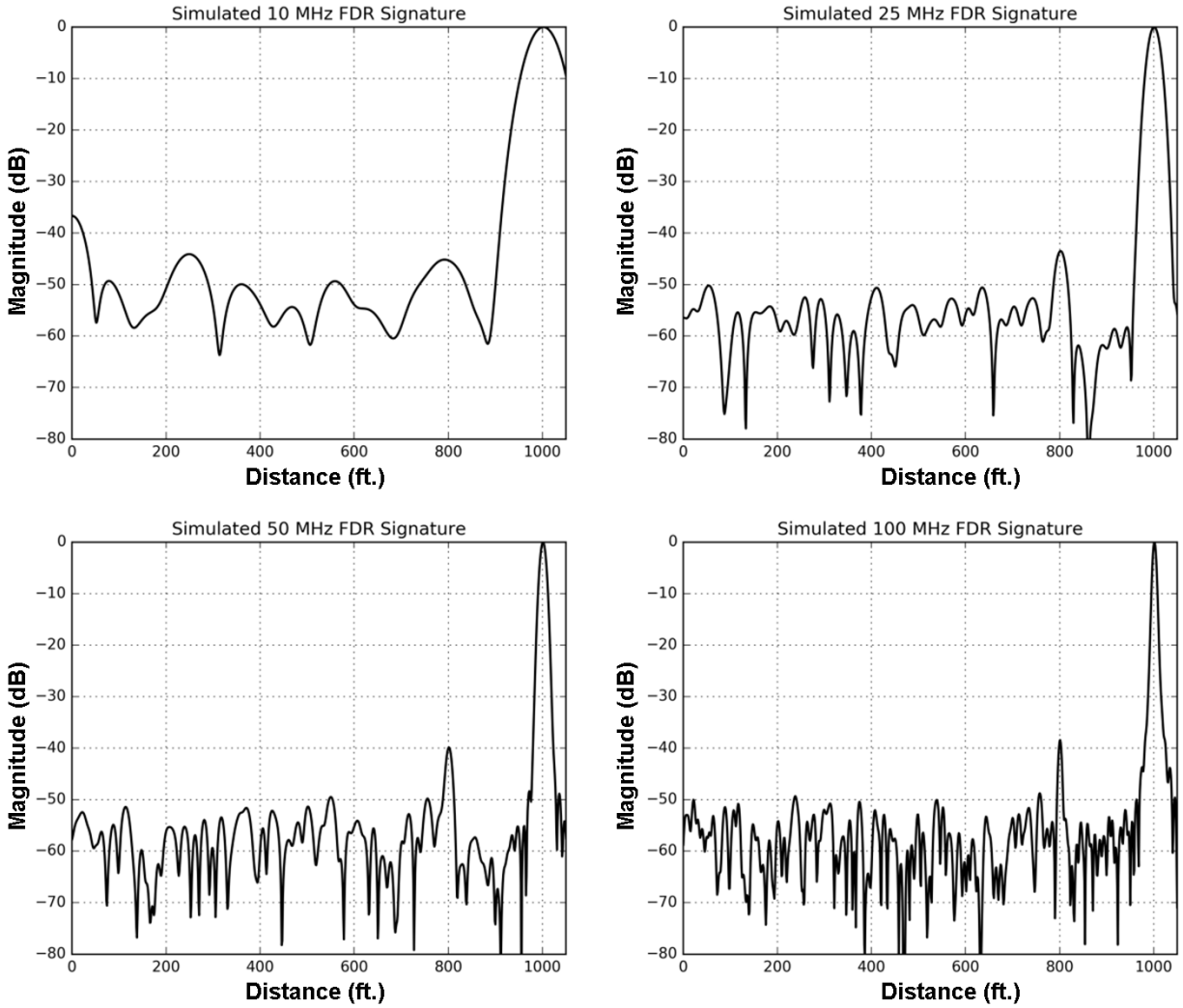


Figure 9.63. LIRA simulations of 1000 ft. twisted-pair cable with loss tangent of 0.01 and 3 ft. defect section at 800 ft. for (*upper left*) 10 MHz, (*upper right*) 25 MHz, (*lower left*) 50 MHz, and (*lower right*) 100 MHz.

The LIRA simulations were repeated for the 1000 ft. cable with the dielectric loss tangent increased to 0.02. These results are shown in Figure 9.64. The stochastic noise parameter was held constant from the previous cable simulation shown in Figure 9.63 to allow direct comparison of the defect response. The defect responses and signal-to-noise ratio are reduced by approximately 3–5 dB at the higher frequencies by the higher loss tangent value.

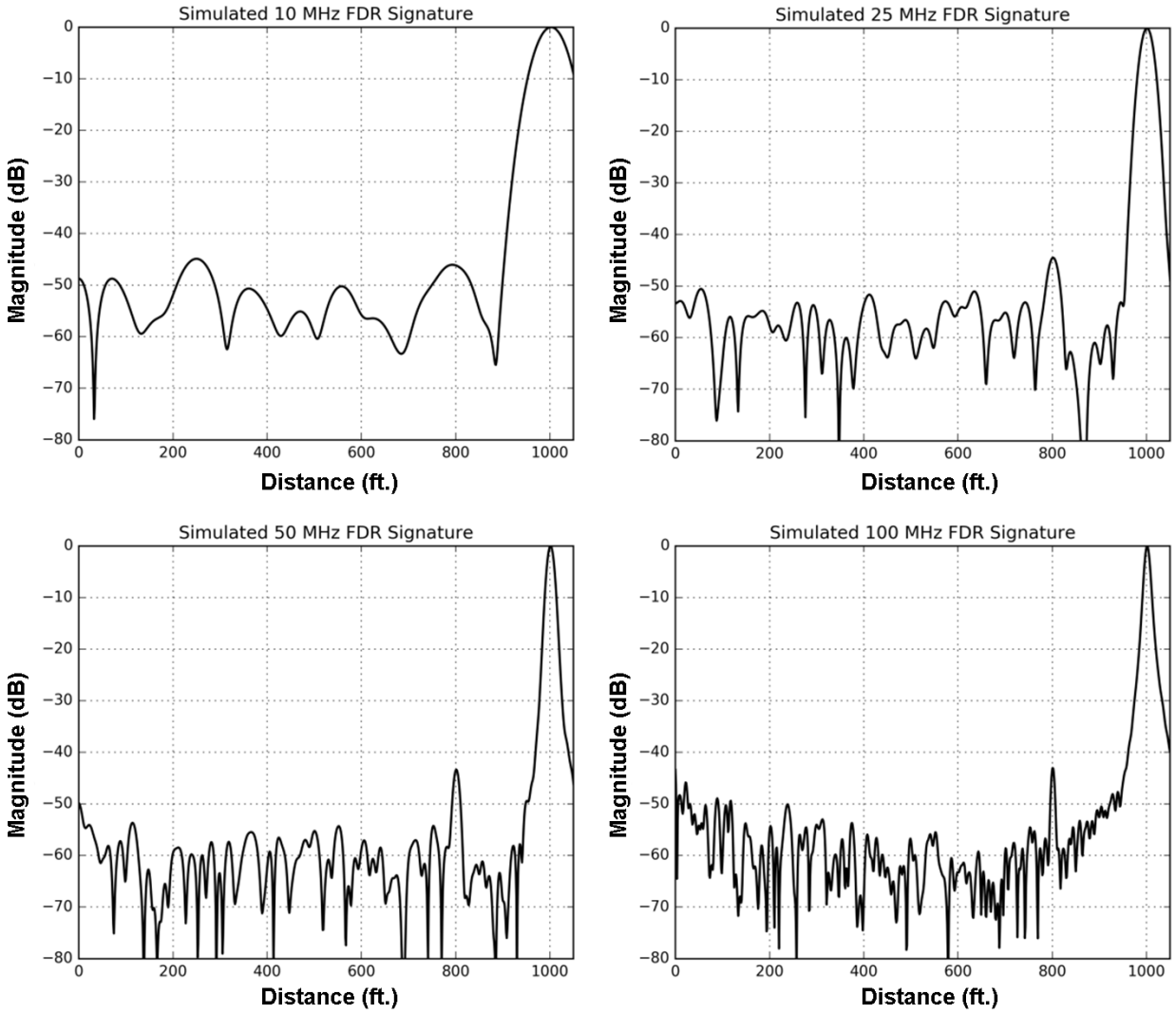


Figure 9.64. LIRA simulations of 1000 ft. twisted-pair cable with loss tangent of 0.02 and 3 ft. defect section at 800 ft. for (*upper left*) 10 MHz, (*upper right*) 25 MHz, (*lower left*) 50 MHz, and (*lower right*) 100 MHz.

To illustrate the effect of cable loss on a higher frequency sweep, the LIRA simulator was used to compare responses for a 1000 ft. cable having different loss tangents for a bandwidth of 200 MHz. The defect was held constant at 800 ft. and the cable loss tangent value was specified as 0.0001, 0.01, and 0.02. These results are shown in Figure 9.65. The higher signal loss degrades the FDR response and illustrates the need to optimize the bandwidth for a given cable inspection.

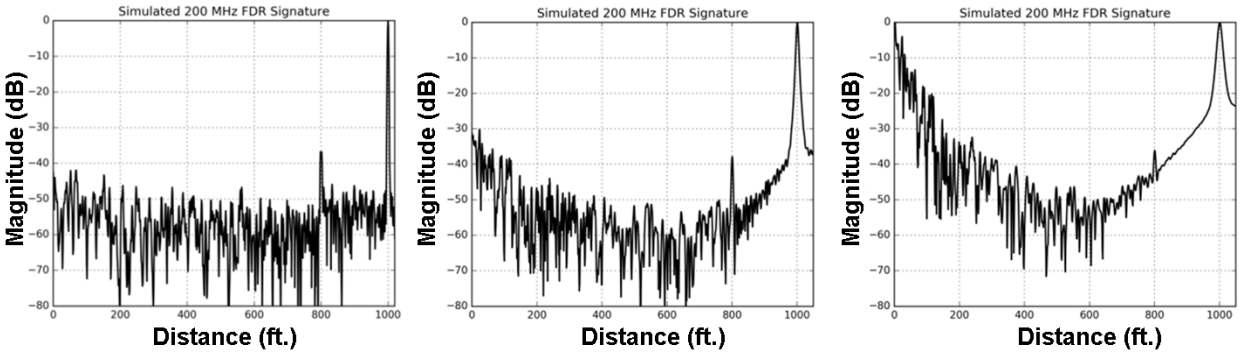


Figure 9.65. LIRA simulations of 1000 ft. twisted-pair cable with 3 ft. defect section at 800 ft. and dielectric loss tangent of (*left*) 0.0001, (*center*) 0.01, and (*right*) 0.02.

To support the simulation study of frequency bandwidth, a series of measurements was performed using 500 ft. and 1000 ft. lengths of a three-conductor shielded cable. Figure 9.66 shows the test layout of the 1000 ft. cable in which the cable was routed along the floor in approximately 90 ft. long straight sections between 180-degree turns. Two 500 ft. cables were created by cutting the 1000 ft. cable into equal sections. The FDR measurements were performed using a VNA and the LIRA Acquire system.

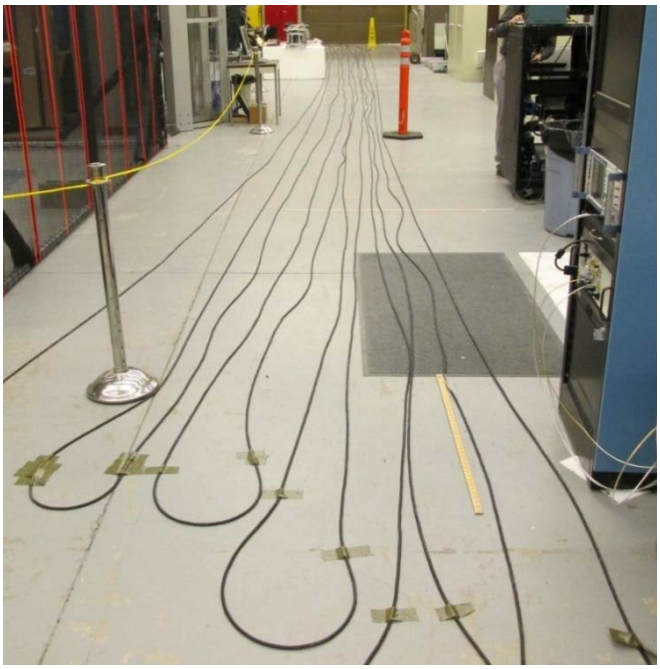

Figure 9.66. Test layout of 1000 ft. three-conductor shielded cable used in bandwidth study.

Figure 9.67 shows the measured LIRA response for the 1000 ft. cable for bandwidths of 10 MHz, 25 MHz, 50 MHz, and 100 MHz. The cable contained no intentionally introduced defects, and any significant peaks are attributed to the 180-degree bends in the cable layout. The results show that bandwidths up to approximately 50 MHz are suitable for inspection of this 1000 ft. cable.

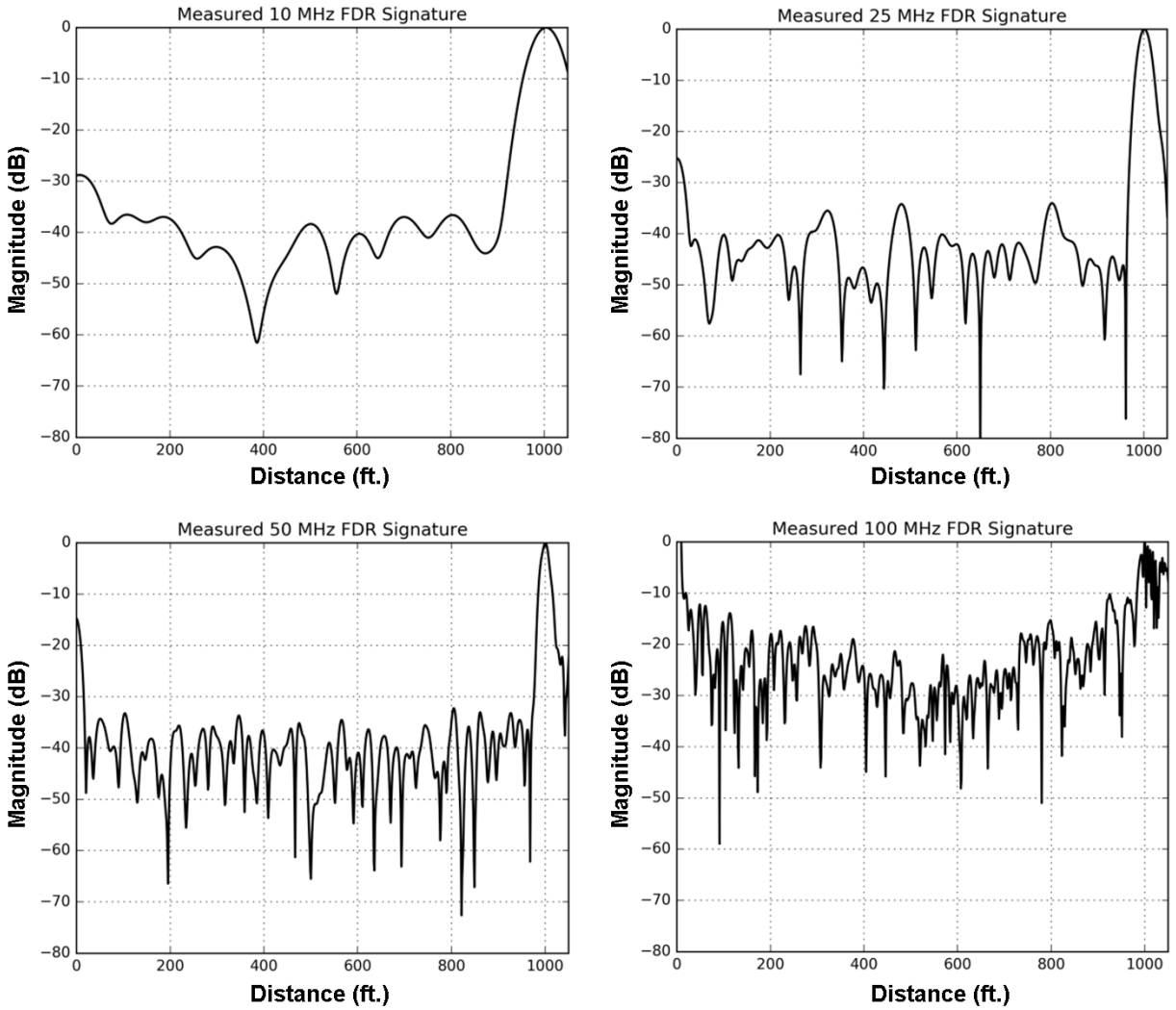


Figure 9.67. LIRA measurements of 1000 ft. three-conductor shielded cable using bandwidth of (*upper left*) 10 MHz, (*upper right*) 25 MHz, (*lower left*) 50 MHz, and *(lower right*) 100 MHz.

Figure 9.68 shows the measured LIRA response using these bandwidths for the 1000 ft. three-conductor shielded cable with a mechanical defect located at 905 ft. The defect consisted of a 1 ft. section having the cable shield and jacket removed as shown in Figure 9.68. The defect peak is concealed within the end termination peak for the 10 MHz response. The defect peak is clearly visible in the 25 MHz and 50 MHz responses. The cable attenuation prevents the defect from appearing in the 100 MHz response.

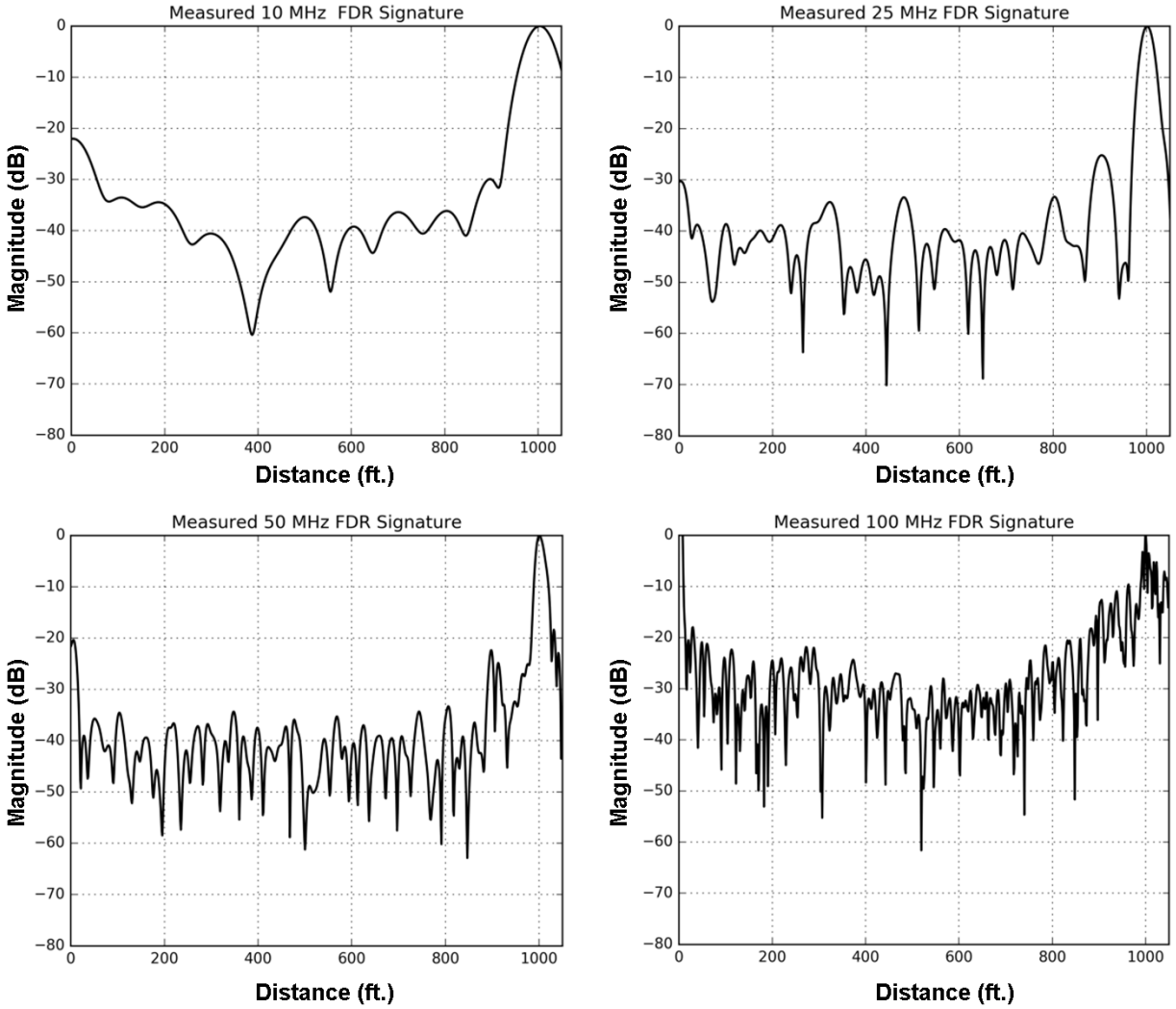


Figure 9.68. LIRA measurements of 1000 ft. three-conductor shielded cable with 1 ft. mechanical defect at 905 ft. using bandwidth of (*upper left*) 10 MHz, (*upper right*) 25 MHz, (*lower left*) 50 MHz, and (*lower right*) 100 MHz.

Figure 9.69 shows the measured LIRA responses at 25 MHz and 50 MHz for the 1000 ft. three-conductor shielded cable as a function of defect length. Each defect was centered at 905 ft. and consisted of a section having the cable shield and jacket removed. For the 25 MHz measurements, the 3.5 in. defect does not produce a noticeable peak and the 6 in. defect has a peak amplitude comparable with some of the cable bends. For the 50 MHz measurements, the peak amplitude for each defect is noticeably above the noise level.

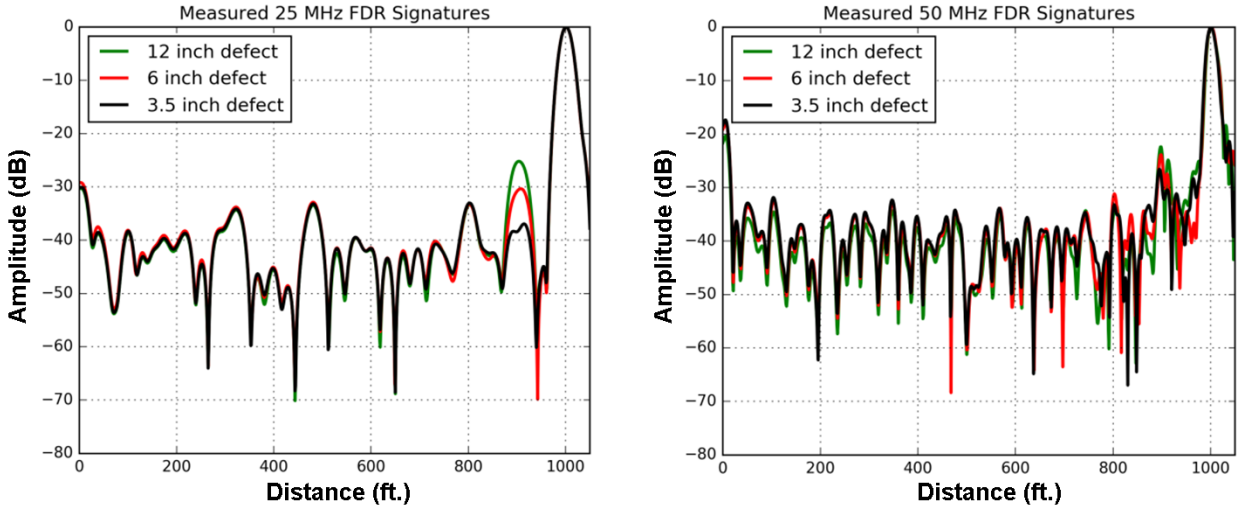


Figure 9.69. LIRA measurements of 1000 ft. three-conductor shielded cable with mechanical defects at 905 ft. using bandwidth of (*left*) 25 MHz and (*right*) 50 MHz.

Figure 9.70 shows the measured VNA responses for the 500 ft. cable using bandwidths of 50 MHz, 100 MHz, 150 MHz, and 200 MHz. The cable contained no intentionally introduced defects, and any peaks are attributed to 180-degree bends in the cable layout. A constant attenuation compensation factor was applied to each dataset to remove the estimated signal loss of the cable. The results show that frequencies up to 150–200 MHz are suitable for inspection of this 500 ft. cable.

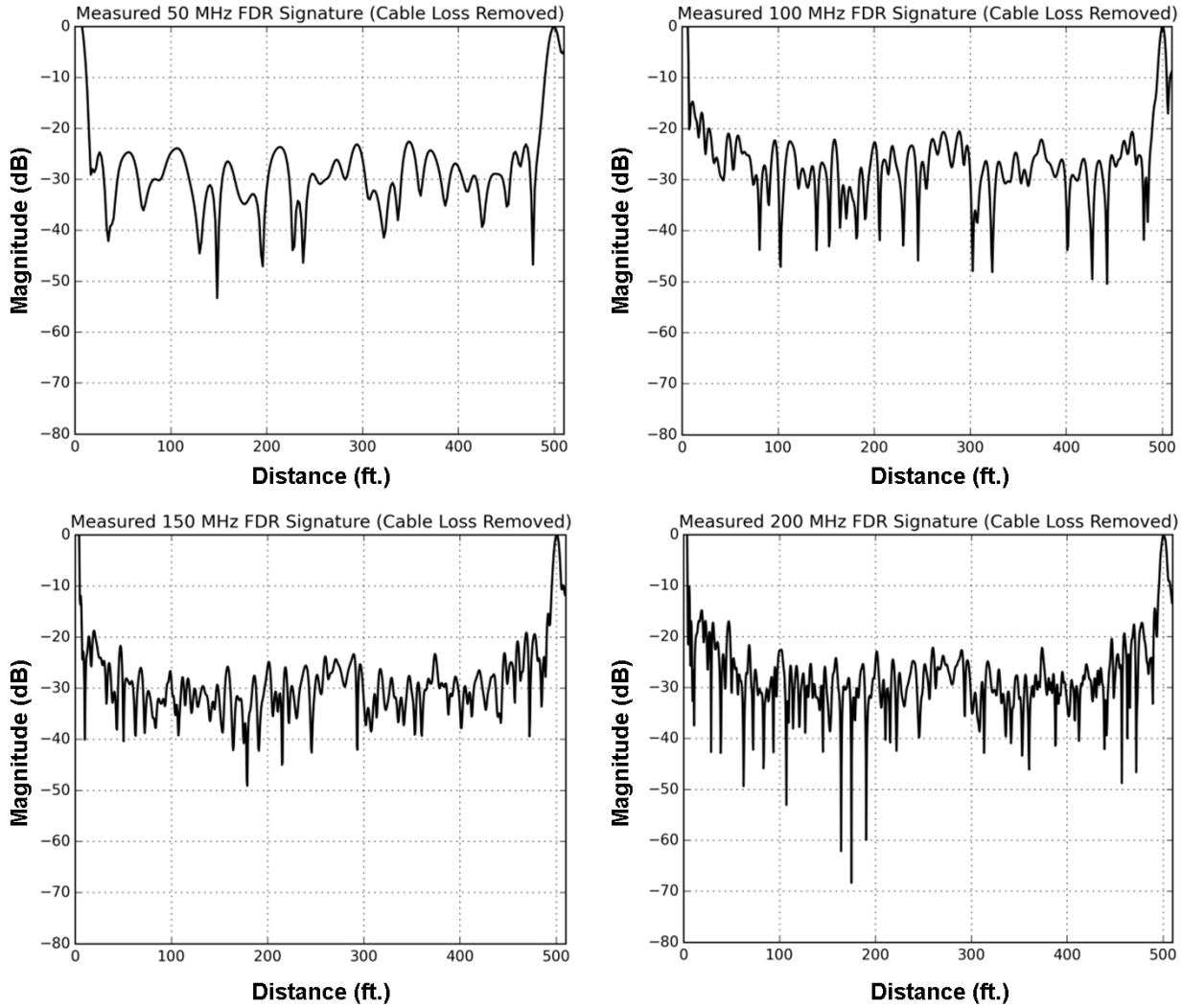


Figure 9.70. VNA measurements of 500 ft. three-conductor shielded cable using bandwidth of (*upper left*) 50 MHz, (*upper right*) 100 MHz, (*lower left*) 150 MHz, and (*lower right*) 200 MHz.

Figure 9.71 shows the measured VNA responses using these bandwidths for a 500 ft. three-conductor shielded cable with a mechanical defect located at 405 ft. The defect consisted of a 1 ft. section having the cable shield and jacket removed as shown in Figure 9.40. A constant attenuation compensation factor was applied to each dataset to remove the estimated signal loss of the cable.

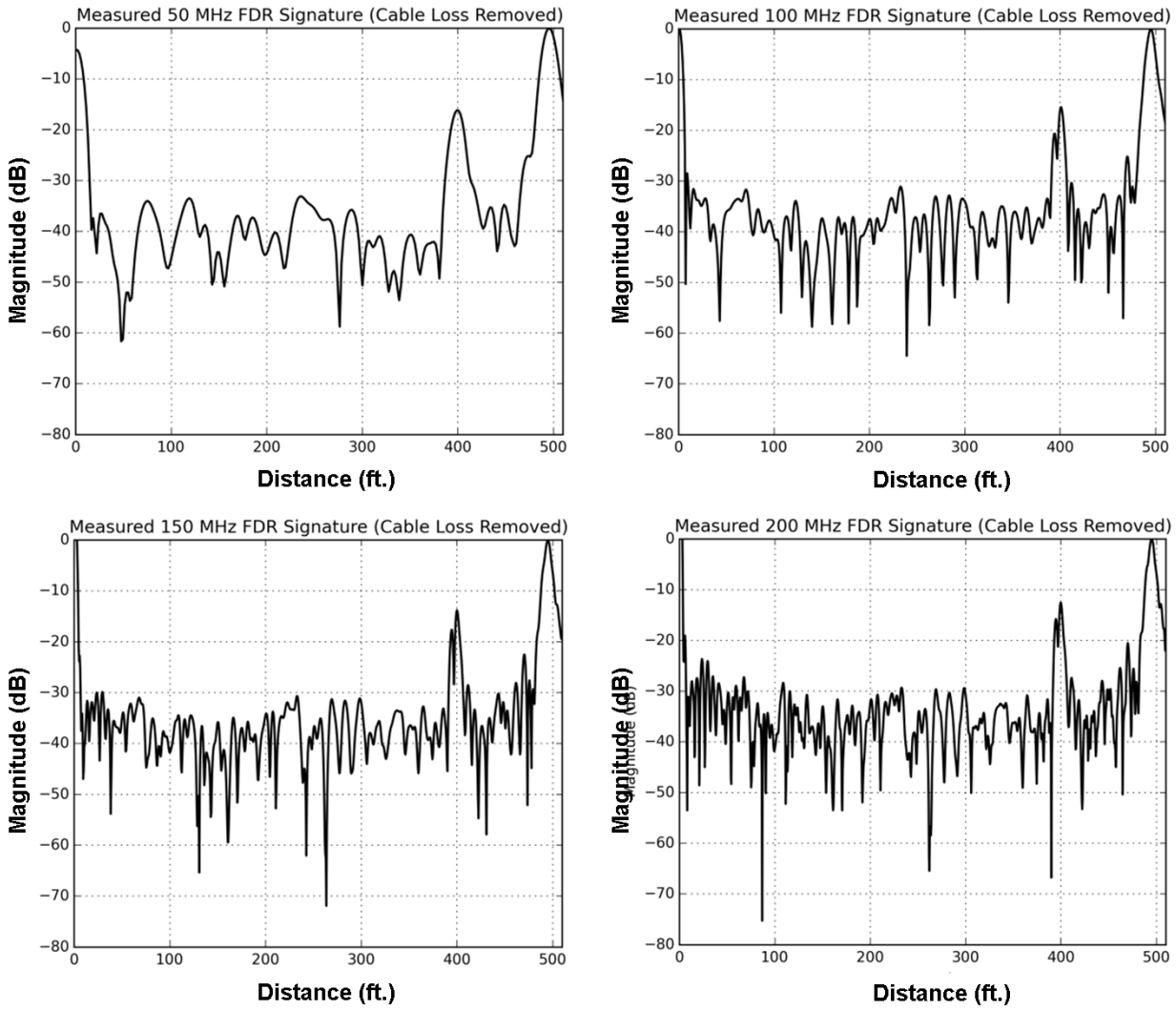


Figure 9.71. VNA measurements of 500 ft. three-conductor shielded cable with 1 ft. mechanical defect at 405 ft. using bandwidth of (*upper left*) 50 MHz, (*upper right*) 100 MHz, (*lower left*) 150 MHz, and (*lower right*) 200 MHz.

# 10. CONCLUSIONS

FDR cable tests are useful for evaluating cable condition and locating regions along the cable with the worst damage. However, interpreting the data is complex as there are a large number of factors that may influence the results. Physics-based cable system models have been developed based on electromagnetic finite element models combined with cascaded circuit network elements. A commercial FDR simulator has also been used to supplement the modeling study.

The simulation results have been validated using test data from a laboratory vector network analyzer and from a commercial cable test system. Using these models, a large number of cable conditions can be simulated to better understand expected FDR cable test behavior with a much more limited set of calibration and demonstration cables. The following conclusions have been drawn from the cases simulated in this report:

- Defect length had an important influence on the FDR amplitude response. The maximum amplitude occurred for defect lengths that are on the order of 0.5 wavelength at the highest frequency used in the FDR inspection. This length corresponds to the spatial resolution available from the frequency sweep. This is an explanation for the relatively small responses for mechanical cable damage, since most mechanically damaged segments are only damaged over a short length.
- For longer damaged segments consisting of a uniform change in the insulation dielectric constant (and thus local capacitance), the FDR response appeared as two distinct peaks centered on the ends of the damaged segments. This began to occur when the defect section was longer than the system resolution. The amplitudes of the two symmetric peaks were smaller than the amplitude of a similarly damaged segment, which was approximately 0.5 to 1 wavelength long at the maximum frequency of the FDR sweep.
- When the damage profile was gradually tapered rather than occurring as a step condition change, the amplitude of the FDR peak was reduced. This effect was due to the tapered impedance transition that reduces the reflection from the tapered portion of the defect segment. If the length of the defect segment was smaller than the spatial resolution, the effect of a tapered damage profile was to simply reduce the FDR peak amplitude relative to the uniform single-step damage profile.
- The FDR peaks were not significantly affected by:
  - Termination impedance value (short circuit, open circuit, finite resistance). The single exception was the LIRA response with a matched termination.
  - Number of defects
  - Location of defects
  - Length of low-loss cable
- The FDR peak amplitudes were affected by:
  - Defect length
  - Defect profile
  - Environment around defect (air, water, metals)
  - Cable loss
  - Frequency bandwidth
- Cable design affects the FDR response. Coaxial cables generally exhibit lower noise because of better fabrication tolerances and can be more sensitive to subtle changes in insulation characteristics than multi-conductor cable. For multi-conductor cables with a helical twist, inevitable variations in the twist rate (lay length) produce random fluctuations in the distributed inductance and capacitance, which can elevate the threshold for detection for defects.

- Shielded and unshielded cable configurations respond differently to the local environment. This difference is expected since the surrounding conductor in shielded cables serves to isolate the propagating signal from the external environment.
- For thermally damaged EPR cable, capacitance changes of 40% to 60% corresponded to an end-of-life EAB of 50%. This was well above the reliably detectable 1% to 5% capacitance change. The threshold for reliable detection is dependent on the intrinsic cable noise.
- The large reflections at the near end and far end of the cable can prevent inspection of degradations in these regions. Increasing the FDR bandwidth shortens the influence of the cable end reflection by improving the range resolution and can improve sensitivity, but higher bandwidths may not completely inspect longer cables due to signal attenuation. Adding separate cable extensions to artificially lengthen the inspection length can improve the ability to discern defect indications if the extension is impedance-matched to the cable being tested, the connection point does not introduce a significant reflection, and the defect amplitude response is large enough. The practicality of this approach may be limited in field conditions due to the difficulty of exactly matching the cable impedance and achieving very low-impedance mis-match connections.
- The swept-frequency bandwidth is a key parameter for obtaining useful data from FDR cable inspections. Simulated and measured cases for 100 ft. to 1000 ft. cables using bandwidths from 10 MHz to 1300 MHz showed the tradeoff between spatial resolution and signal attenuation. In example measurements, bandwidths of 200 MHz and 50 MHz were successfully used to inspect a shielded triad cable with lengths of 500 ft. and 1000 ft., respectively.

# 11. FUTURE WORK

This modeling effort provided significant insight for a small set of cables. The work will continue into future reporting periods to investigate other cable configurations including multi-conductor cables with varying paired conductors and other more complex cable designs. The work may also be extended to assessing other frequency domain tests such as dielectric spectroscopy and joint time frequency domain reflectometry.

# 12. REFERENCES


Agilent. 2012. *Time Domain Analysis Using a Network Analyzer*. Application Note 1287-12, Agilent Technologies, Santa Clara, California. Available at http://cp.literature.agilent.com/litweb/pdf/5989-5723EN.pdf.

Alsharif M, P Wallace, D Hepburn and C Zhou. 2012. "FEM Modeling of Electric Field and Potential Distributions of MV XLPE Cables Containing Void Defect." In *Proceedings of the 2012 COMSOL Conference*. October 10-12, 2012, Milan. COMSOL, Inc., Burlington, Massachusetts. Available at https://www.comsol.com/paper/fem-modeling-of-electric-field-and-potential-distributions-of-mv-xlpe-cables-con-13431.

ANSYS. 2014. *Application Brief: Power Cable Analysis*. ANSYS, Inc. Canonsburg, Pennsylvania. Accessed March 29, 2017. Available at http://resource.ansys.com/staticassets/ANSYS/staticassets/resourcelibrary/techbrief/ab-power-cable-analysis.pdf.

Brown J, R Bernstein, G Von White II, S Glover, J Neely, G Pena, K Williamson, F Zutavem and F Gelbard. 2015. *Submerged Medium Voltage Cable Systems at Nuclear Power Plants: A Review of Research Efforts Relevant to Aging Mechanisms and Condition Monitoring*. SAND2015--1794, Sandia National Laboratories, Albuquerque, New Mexico. DOI: 10.2172/1177756.

Chen Q, K Burkes, E Makram, R Hadidi and X Xu. 2014. "Capacitance of Water Tree Modeling in Underground Cables." *Journal of Power Engineering* 2(11):9-18. DOI: 10.4236/jpee.2014.211002

EEWeb. 2015. *Twisted Pair Calculator*. EEWeb Electrical Engineering Community. Accessed May 12, 2017. Available at https://www.eeweb.com/toolbox/twisted-pair.

EPRI. 1994. *Low-Voltage Environmentally-Qualified Cable License Renewal Industry Report; Revision 1*. TR-103841, Electric Power Research Institute (EPRI), Palo Alto, California.

EPRI. 2005. *Initial Acceptance Criteria Concepts and Data for Assessing Longevity of Low-Voltage Cable Insulations and Jackets*. TR-1008211, Electric Power Research Institute (EPRI), Palo Alto, California.

EPRI. 2015. *Plant Engineering: Evaluation and Insights from Nuclear Power Plant Tan Delta Testing and Data Analysis - Update*. TR-3002005321, Electric Power Research Institute, Palo Alto, California.

Eriksson R, R Papazyan and G Mugala. 2006. "Localization of Insulation Degradation in Medium Voltage Distribution Cables." In *First International Conference on Industrial and Information Systems*, pp. 167-172. August 8-11, 2006, Sri Lanka. DOI 10.1109/ICIIS.2006.365658. IEEE.

Fantoni PF and A Nordlund. 2006. *Wire System Aging Assessment and Condition Monitoring (WASCO)*. NKS-130, Nordic Nuclear Safety Research, Roskilde, Denmark.

Fifield LS, MP Westman, A Zwoster and B Schwenzer. 2015. *Assessment of Cable Aging Equipment, Status of Acquired Materials, and Experimental Matrix at the Pacific Northwest National Laboratory*. PNNL-24198, Pacific Northwest National Laboratory, Richland, Washington.

Furse C, YC Chung, R Dangol, M Nielsen, G Mabey and R Woodward. 2003. "Frequency-domain Reflectometry for On-board Testing of Aging Aircraft Wiring." *IEEE Transactions on Electromagnetic Compatibility* 45(2):306-315. DOI: 10.1109/TEMC.2003.811305.

General Cable. 2016. *Industrial Cable, SPEC 4325*. General Cable Technologies Corporation. Highland Heights, Kentucky. Accessed May 15, 2017. Available at http://viewer.epaperflip.com/Viewer.aspx?docid=a1a03078-bddf-49e5-a4de-a74e013cb246#?page=38.

Glass SW, LS Fifield, G Dib, JR Tedeschi, AM Jones and TS Hartman. 2015. *State of the Art Assessment of NDE Techniques for Aging Cable Management in Nuclear Power Plants FY2015*. M2LW-15OR0404024, PNNL-24649, Pacific Northwest National Laboratory, Richland, Washington.

Glass SW, LS Fifield and TS Hartman. 2016a. *Evaluation of Localized Cable Test Methods for Nuclear Power Plant Cable Aging Management Programs*. M3LW-16OR0404022, PNNL-25432, Pacific Northwest National Laboratory, Richland, Washington.

Glass SW, AM Jones, LS Fifield and TS Hartman. 2016b. *Bulk Electrical Cable Non Destructive Examination Methods for Nuclear Power Plant Cable Aging Management Programs*. PNNL-25634, Pacific Northwest National Laboratory, Richland, Washington.

IEC. 2002. *Broadband Services, Applications, and Networks: Enabling Technologies and Business Models*. International Electrotechnical Commission (IEC).

IEC/IEEE 62582-3. 2011. Nuclear Power Plants – Instrumentation and Control Important to Safety – Electrical Equipment Condition Monitoring Methods – Part 3: Elongation at Break." IEC/IEEE, Geneva.

Imperatore MV. 2017. *Dielectric Spectroscopy as a Condition Monitoring Diagnostic Technique for Thermally Aged PVC/EPR Nuclear Power Plant Cables*. Masters Thesis, University of Bologna.

Johnson MK. 1984. *Calculation of Transmission Line Impedances Using the ANSYS Finite Element Program*. TM-1270, Fermilab, Batavia, Illinois. Available at http://lss.fnal.gov/archive/tm/TM-1270.pdf.

Kuan TM, AM Ariffin, S Sulaiman and YHM Thayoob. 2011. "Wave Propagation Characteristics of Polymeric Underground Cables." In *5th International Power Engineering and Optimization Conference*, pp. 410-415. June 6-7, 2011, Shah Alam, Selangor, Malaysia. DOI 10.1109/PEOCO.2011.5970396. IEEE.

Lofaro M and R Villaran. 2002. *Evaluation of Aging and Qualification Practices for Cable Splices Used in Nuclear Power Plants*. NUREG/CR-6788, Brookhaven National Laboratory, Brookhaven, New York.

Mantey A. 2015. "Evaluation and Insights from Nuclear Power Plant Tan Delta Testing and Data Analysis-Update." Presented at *Power and Energy Society Insulated Conductors Committee, Subcommittee D*, November 3, 2015, Tucson, Arizona.

Minet J, S Lambot, G Delaide, JA Huisman, H Vereecken and M Vanclooster. 2010. "A Generalized Frequency Domain Reflectometry Modeling Technique for Soil Electrical Properties Determination." *Vadose Zone Journal* 9(4):1063-1072. DOI: 10.2136/vzj2010.0004.

Mohr and Associates. 2010. *Application Note: TDR vs. FDR: Distance-to-Fault*. Mohr and Associates, Richland, Washington. Available at http://www.mohr-engineering.com/TDR_vs_FDR_Distance_to_Fault-A.php.

Murty KL, Ed. 2013. *Materials Ageing and Degradation in Light Water Reactors: Mechanisms and Management*. Woodhead Publishing, Cambridge, United Kingdom.

NRC. 2010. *Condition Monitoring Program for Electric Cables Used in Nuclear Power Plants*. Draft Regulatory Guide DG-1240, U.S. Nuclear Regulatory Commission, Washington, D.C. Available at http://pbadupws.nrc.gov/docs/ML1007/ML100760364.pdf.

NRC. 2012. *Condition-Monitoring Techniques for Electric Cables Used in Nuclear Power Plants*. Regulatory Guide 1.218, U.S. Nuclear Regulatory Commission, Washington, D.C. Available at http://pbadupws.nrc.gov/docs/ML1035/ML103510447.pdf. ADAMS Accession No. ML103510447.

Ramuhalli P, LS Fifield, MS Prowant, G Dib, JR Tedeschi, JD Suter, AM Jones, MS Good, SW Glass and AF Pardini. 2015. *Assessment of Additional Key Indicators of Aging Cables in Nuclear Power Plants -- Interim Status for FY2015*. PNNL-24309, Pacific Northwest National Laboratory, Richland, Washington.

Simmons KL, LS Fifield, MP Westman, JR Tedeschi, AM Jones, MS Prowant, AF Pardini and P Ramuhalli. 2014. *Determining Remaining Useful Life of Aging Cables in Nuclear Power Plants -- Interim Status for FY2014*. PNNL-23624; INL-EXT-14-32505 Rev. 0, Pacific Northwest National Laboratory, Richland, Washington.

Simmons KL, P Ramuhalli, DL Brenchley and JB Coble. 2012. *Light Water Reactor Sustainability (LWRS) Program – Non-Destructive Evaluation (NDE) R&D Roadmap for Determining Remaining Useful Life of Aging Cables in Nuclear Power Plants*. PNNL-21731, Pacific Northwest National Laboratory, Richland, Washington.

Strikwerda A. 2016. *Model Cables and Transmission Lines in COMSOL Multiphysics*. COMSOL, Inc. Burlington, Massachusetts. Accessed March 29, 2017. Available at https://www.comsol.com/blogs/model-cables-and-transmission-lines-in-comsol-multiphysics/.